Summer 2007

Modeling and performance estimation for airborne minefield detection system

Saurabh Agarwal

Department:

MODELING AND PERFORMANCE ESTIMATION FOR AIRBORNE MINEFIELD DETECTION SYSTEM

by

SAURABH AGARWAL

A THESIS

Presented to the Faculty of the Graduate School of the

UNIVERSITY OF MISSOURI-ROLLA

In Partial Fulfillment of the Requirements for the Degree

MASTER OF SCIENCE IN ELECTRICAL ENGINEERING

2007

Approved by

_____	_____
Sanjeev Agarwal, Advisor	R. Joe Stanley

_____

Steve Grant

ABSTRACT

Many programs aimed at airborne mine and minefield detection are being pursued and different algorithms are being developed and evaluated to achieve performance specifications. Thus far, no single algorithm or detection architecture has been able to fulfill the performance specifications for different mine and minefield detection scenarios. The reasons for this are numerous. The environment and the operating conditions under which an airborne sensor is expected to perform are highly varied. Also, the performance of airborne sensors and algorithms is highly dependent on the type of targets and environments. Research has been aimed to make the algorithms more robust under these varying conditions, but the studies have been only partially successful. A large amount of data needs to be collected and analyzed to gain insight into detection algorithms and their performance under different operating conditions. Data collection on this scale is time consuming, and costly. Due to this reason, a need exist for a simulation-based approach. One such simulation system is developed and evaluated in this thesis. The factors affecting the performance of an airborne detection system include physical parameters (type of background, time of day), data collection parameters (swath width, number of steps, in-step and in-flight overlap), and minefield scenarios. Data collection parameters are included in the simulation tool. False alarms and mine statistics are modeled based on the available data collected as a part of the developmental programs. Various mine and minefield detection algorithms are modeled and evaluated. Simulations are run, and Receiver Operating Characteristic (ROC) curves are used to evaluate the performance at both the mine and minefield levels. Analytical models for minefield detection performance are formulated and used to validate the simulated performance.

ACKNOWLEDGMENTS

This thesis would not have been a reality without the support of many people. First and foremost I am extremely grateful to my advisor, Dr. Sanjeev Agarwal, for his constant support and help throughout the master's program. His encouragement and confidence helped me to make this thesis a reality. I would also like to thank Dr. Stanley and Dr. Grant for being on my committee.

I would also like to thank all my friends in my research group, especially Sumesh Nair Kesavan for his constant support and help throughout my research. I would also like to thank the Countermine Division of Night Vision and Electronic Sensors Directorate (NVESD) for providing the financial support, data and the opportunity to work on this project.

In addition, I would like to express my eternal gratitude towards my parents for always being there for me and helping me in all my difficult situations.

TABLE OF CONTENTS

LIST OF ILLUSTRATIONS

Page

LIST OF TABLES

Page

1. INTRODUCTION

Solutions to landmine and minefield detections have been sought for more than 75 years. A number of different sensors, algorithms and technologies have been proposed and are now being pursued for landmine detection. All mine detection technologies can be classified into two major categories: ground-based mine detection and airborne minefield detection. Ground-based technologies consist of handheld and vehicular mine detection in which either a human or a vehicle carrying a mine detection device scans the neighborhood for mines. However, these techniques suffer with a number of obvious drawbacks. First of all, due to the presence of humans; the risk of fatal errors always exists. It is estimated that for every 2000 mines cleared, a fatal human error occurs [Ghaffari et al., 2004]. Second, ground-based methods are slow because one person clearing mines by hand can clear up to 20 to 50 square meters per day, and a vehicle can cover about 15,000 square meters per day, which is often considered to be very slow [Dincerler, 1995]. Third, mines are available in different materials as well as, different sizes and shapes. This imposes limitations in the equipment and technologies used for the landmine detection.

Because of the fatal errors, slow clearing of mines of ground based minefield detection system, and for tactical reasons in counter mine operations, airborne mine/minefield detection using unmanned airborne vehicles (UAV) have gained popularity in recent years. Some of the recent airborne minefield detection programs in this research area include the Airborne Far IR Minefield Imaging System (AFIRMIS) [Simrad and Mathieu, 1998], Remote Minefield Detection System (REMIDS) [1999], Cobra Reconnaissance and Analysis System (COBRA) [Witherspoon et al., 1995], and Lightweight Airborne Multi-spectral Minefield Detection System [LAMD] [Haskett and Reago, 2001]. Visual, near-infrared, and mid-wave infrared images of a minefield taken from an airborne platform are processed at a ground station to determine the likely presence of minefields and other obstacles. The data are collected using a sensor mounted on a gimbal in either a push broom or step stair manner. The detection process typically follows a sequential paradigm based on the detection of mine-like anomalies followed by the detection of minefield-like patterns.

A huge amount of data is being collected and analyzed to gain insight into the actual mine and minefield detection algorithms and their performance. Various anomaly detections algorithms such as RX [Reed and Yu, 1990], radial anomaly detector [Menon and Agarwal, 2003], cluster based anomaly detection [Carlotto, 2005], signal subspace processing [Ranney, 2006], support vector data description [Banerjee et al., 2006], and false alarm reduction methods such as, gray-scale moments [Sriram et al., 2002], circularity [Menon et al., 2004], and reflection symmetry [Menon et al., 2004; Kiryati and Gofman, 1996] have been used to identify mine like targets. Various minefield detection algorithms have been similarly proposed such as the empty boxes test algorithm [Lake et al., 1997], linear pattern detection [Malloy, 2003; Muise and Smith, 1995], Hough line transforms [Carlson et al., 1994], Scatter Number [Earp, 2000b] and Scatter Log weighted [Earp et al., 1995].

Apart from the algorithm choices, the performance of the system depends on various other factors, including minefield scenarios (such as scattered or patterned), and data collection parameters such as swath width, side step overlap, and the size of the field of regard (FoR). Mine and minefield detection algorithms need to be evaluated for different backgrounds like arid and temperate. To evaluate the performance of the sensors and detection algorithms for different scenarios and algorithm choices, an enormous amount of data collection is required. This collection and subsequent analysis of data is one of the most expensive aspects in the process of system development and evaluation. Moreover, it is impossible to collect the data for all possible variations in mine and minefield detection scenarios and other data collection parameters. However, it is quite possible to generate reasonably accurate simulation data under different sensors, minefield layout scenarios, and mission-specific constraints. The simulated data can subsequently be used to evaluate the performance of different choices of algorithms and data collection models under different scenarios. This thesis describes the design of a simulation tool to evaluate mine and minefield level performances based on simulated data under different sensors and mission profile parameters. Mine and minefield level performances obtained using simulated data are verified using analytical results and available data.

This thesis is organized as follows. Section 2 starts with the basic airborne minefield detection system and explains its various blocks with the help of actual data. Section 3 explains the simulation system, which is developed to simulate the minefield detection system and also describe the flexibility incorporated in the simulated systems. This system evaluates the performance for a particular choice of data collection parameters, minefield scenarios, and mine and minefield detection and thresholding algorithm.

Section 4 presents a detailed explanation of the RX anomaly detector. The RX detection values are then modeled using standard probabilistic models. The modeling results for different times of day and, different background types are provided. The performance of these models for different datasets is tested using the chi square test.

Section 5 deals with spatial distributions that are used to model the spatial locations of the false alarms. Complete spatial random processes, their tests and generation methods are discussed in some detail. Preliminary results for spatial distribution of mines and false alarms are also presented.

Section 6 deals with analytical models for different minefields detection methods. It also explains the choice of minefield detection algorithms used for detecting the presence of a minefield. Minefield scoring techniques are also explained in this section. Section 7 shows simulation results for a particular set of parameters. Simulation results are generated showing the effect of various parameters including swath width, signal to clutter ratio, constant false alarm rate, and segment overlap. This thesis concludes with Section 8, which discusses the general conclusions and future work in this area.

Some of the supporting concepts and derivations are included in four Appendices. Appendix A lists various spectral vegetation indices. It also shows the capability of these indices to differentiate between vegetation and non-vegetation (rock, soil, etc.). Appendix B discusses the EM algorithm and its mathematical formulation. It also derives the formulation of the update equation and finally parameter estimation for RX statistics. Convergence properties of the EM algorithm are also discussed. Appendix C explores the method of moments to estimate the initial parameters for RX distribution to be used for the EM estimation. Appendix D discusses different tests to evaluate the goodness of fit for the probability model obtained.

2. PROBLEM DESCRIPTION

This section describes the basic airborne minefield detection system and the role different parameters play in determining detection performance. A typical airborne minefield detection system can be described in the form of the block diagram in Figure 2.1. It consists of three different stages, each represented by a single block. The first stage involves data collection, which deals with various factors such as platform data, sensor data, minefield layout, and background data. Once the data are collected, they are processed in the mine level detection block to provide a list of anomalies, which are different for different backgrounds and depend on the anomaly detection algorithm used for the processing. The anomaly values are then thresholded and passed to minefield level detection block where the thresholded anomaly values are processed along with their spatial locations to provide a confidence metric pertaining to the presence of a minefield. Minefield level scoring is used to evaluate the performance of the airborne minefield system in terms of Receiver Operating Characteristic (ROC) curves.

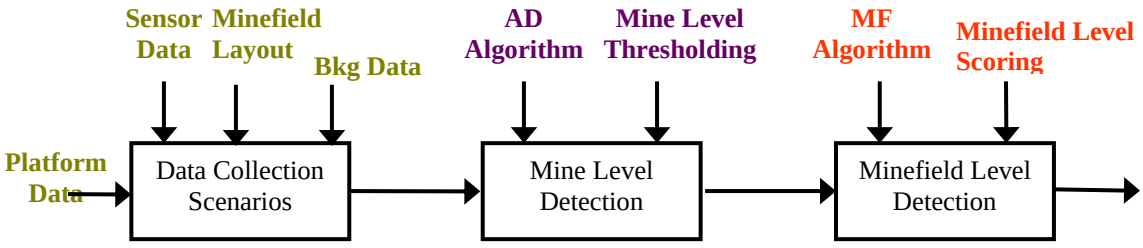

Figure 2.1. Block Diagram for a Typical Airborne Minefield Detection System

Different data collection scenarios, as well as mine detection and minefield detection algorithms, are the main drivers of the performance of this airborne minefield detection system. Each of these blocks is discussed briefly in the following section and elaborated further in later sections.

2.1. DATA COLLECTION SCENARIOS

The airborne data are collected in the form of a sequence of image frames captured as the sensor is flown over the minefield. In a typical system, the airborne sensor is flown over the minefield area at a predefined altitude and speed, with a gimbal to collect frames of images in a specified pattern. The image data collected from one flight are called a *run*. A specified number of frames create a segment/field of regard (FoR), and a set of segments constitutes a run. The geo-locations of each frame along with other information constitute Meta data (data of data) collected using onboard GPS and IMU. These Meta data and any available image overlap are used to reconstruct the ground image for the FoR. Minefield decision is based on the detection statistics calculated over this FoR. Various factors of data collections that may affect the minefield detection performance are discussed below.

2.1.1. Background Data. Background data play an important role in performance evaluation. Background refers to the ground terrain in which mines are being laid. The background may be vegetation, soil, road, or a combination of two or more of these areas. Vegetation can be either thick forest or tall grass, and soil can be either rough clay or smooth desert terrain among others. Apart from natural background there may be cultured sources of clutter in the background like soft drink cans among others. In order to capture the impact of these on the detection performance, both natural and cultured sources of clutter should be modeled appropriately.

2.1.2. Minefield Layout. Mines are distributed in a predefined pattern that includes both patterned and scattered distribution. Each minefield will exhibit different performance due to different types of mines (metal, plastic, etc.), different sizes of mines, and different types of spatial distributions of mines. These layouts of the minefields are dictated primarily by the mechanism by which mines are laid in the minefield and tactical scenarios. The mines can be laid manually, by ground vehicle, or by helicopter. The mines can be surface laid or buried and can be of different sizes varying from small to large. Mines can also be classified based on the composition, i.e., they can be made up of either metal or plastic. Figure 2.2 shows the distribution of mines. Figure 2.2(a) shows typical distribution of mines for the case of scattered and Figure 2.2(b) shows typical distribution of mines for patterned minefields. Detection of mines depends greatly on the

type of mine (plastic or metal), size (large, medium or small), and color of mines (tan, green). Apart from these factors, number of other factors such as background terrain, time of day also influences the performance.

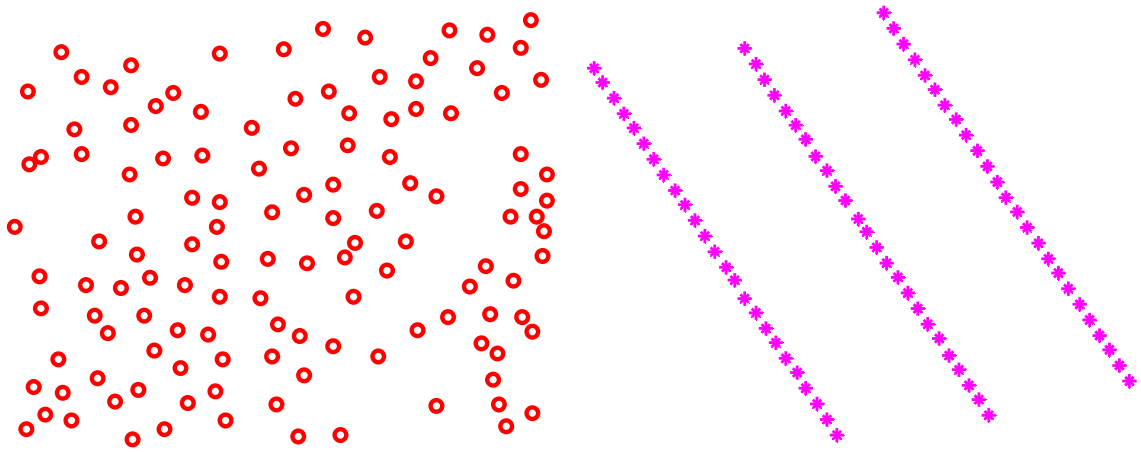

(a) Scattered Minefield (b) Patterned Minefield

Figure 2.2. Typical Distribution of Mines in Scattered and Patterned Minefield

2.1.3. Platform Data. Platform data comprises a number of parameters such as the altitude at which the UAV is flying, flight speed, flight angle, and start position of the UAV. The flight altitude decides the ground sample distance (GSD) along with other parameters for the images, whereas the flight speed determines the frame rate for the image data to be collected and the in-flight overlap between the frames. In the real environment, these platform parameters are not constant and change across the frames and segments due to various reasons. Various distributions can be used to model these parameters. The variability of the start position and the start angle relate to how the run encounters the minefield front.

The flight speed and a number of other factors including the wind angle, roll, yaw, and pitch of the vehicle are also not constant throughout the whole run. Even the altitude of the flight changes over the run due to changes in the terrain relief, which eventually change the image resolution for a particular frame. Sensor parameters such as side-step overlap also vary due to wobbling in the platform and gimbal pointing error.

Figure 2.3 shows variations in the flight altitude, flight speed, and heading angle for four consecutive segments (84 frames) corresponding to the same run of the airborne data. Table 2.1 shows various parameters and corresponding statistics for a particular run.

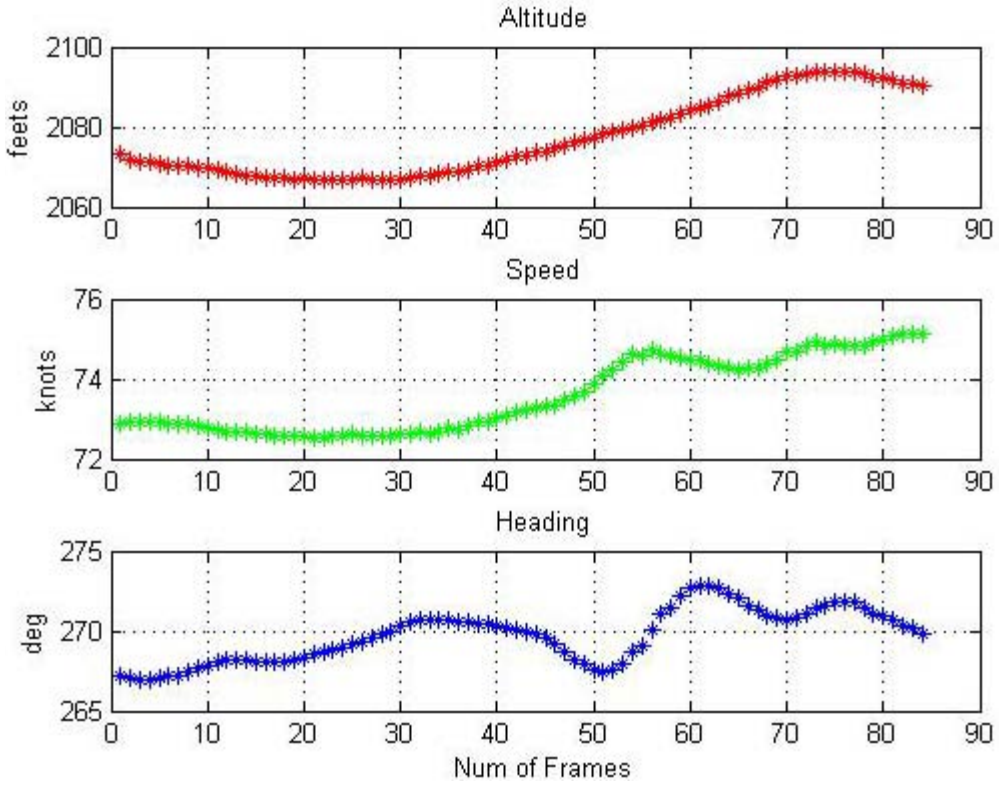

Figure 2.3. Variation in Flight Altitude, Speed, and Heading Angle for Four Segments from Airborne Data

2.1.4. Sensor Data. Sensor data deal with the parameters of the sensor used for the collection of data. For current purposes, the sensors are basically imaging sensors that operate over various frequency bands of the EM spectrum. Many sensors operate in the mid-wave infra red (MWIR) frequency range because this frequency band is sensitive to the thermal contrast as well as reflectance and has desirable spatial resolution. Significant thermal contrast can be found between metallic and non-metallic mines and typical backgrounds for surface as well as buried mines, making the imaging more convenient than other modalities. The MWIR provides useful data during both day time and night

time imaging. Multi spectral imaging (MSI) sensors in visual and near infrared are also used for the image capture. These sensors facilitate the dual purpose of creating a colored image from the individual bands as well as showing features in visual and near infrared bands that may not be prominent in any one of the single band.

Table 2.1. Various Parameters and Segment Information for a Particular Run

Date	8-May-05		
Time	14.51.12	Afternoon Time Data	
No. of IR segments	57		
No. of MSI segments	57		
	Mean	**Standard Deviation**	**Units**
Altitude	2073.00	149.59	feet
Flight Speed	72.77	3.29	knots
Segment Width	59.95	9.40	meters
Segment Length	172.48	10.74	meters

Figure 2.4 shows an example of the tiled image for the daytime MWIR image segment. Figure 2.5 shows a single frame for red, green, blue, and NIR bands of the MSI sensor. The MSI sensor, however, is unavailable at night time due to the lack of illumination. Figure 2.6 shows the tiled image for the night time MWIR image segment. For the comparison sake, the area covered in night time and day time IR segment is the same. Because MWIR data shows a mix of reflection and thermal signature in contrast to MSI data, which is primary based on reflected data, it is useful even in the night time.

2.1.5. Reconstruction/Registration. The individual overlapping image frames for the FoR obtained using the gimbal needs to be stitched together to create mosaic image of the FoR. This method is called registration. Figures 2.7 and 2.8 show an example for the daytime MWIR and MSI image segments, respectively, for the same segment whose tiled image is shown in Figure 2.4. The colored image in Figure 2.7 and elsewhere are generated using the red, green, and blue bands. Figure 2.9 shows the corresponding night time data for MWIR. One of the same terrain features is indicated by a red circle in all three images for easy comparison.

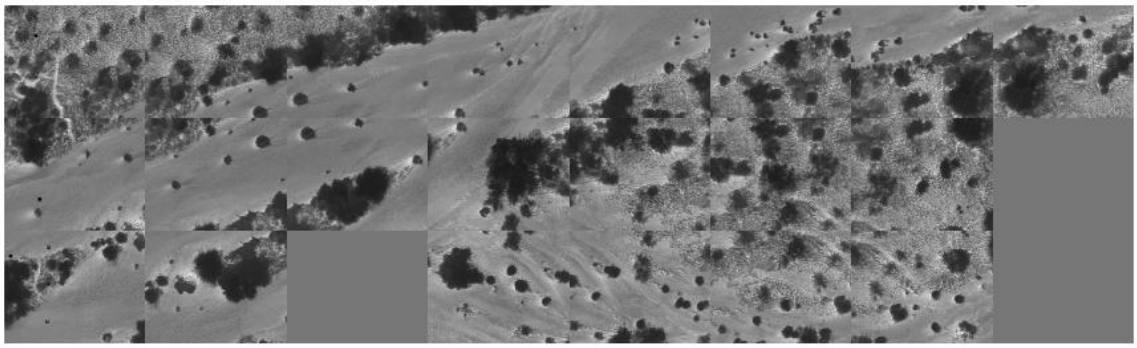

Figure 2.4. Tiled Image Segment for MWIR Data

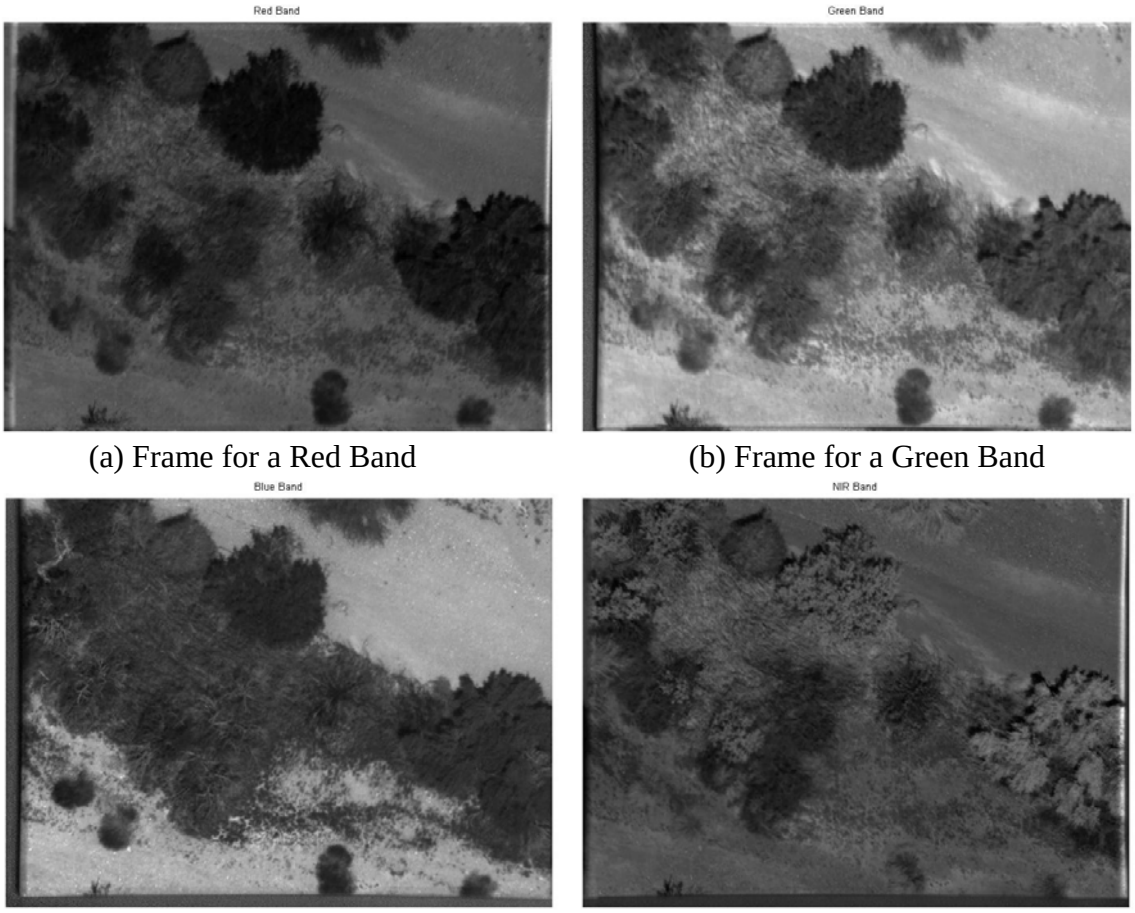

(a) Frame for a Red Band (b) Frame for a Green Band

(c) Frame for a Blue Band (d) Frame for a NIR Band

Figure 2.5. Red, Green, Blue, and NIR Frames for an MSI Image Segment

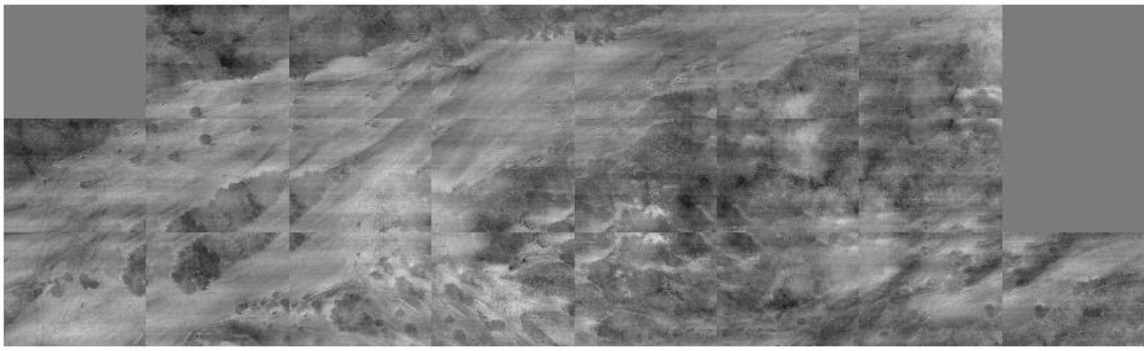

Figure 2.6. Tiled Image Segment for Night Time MWIR Data

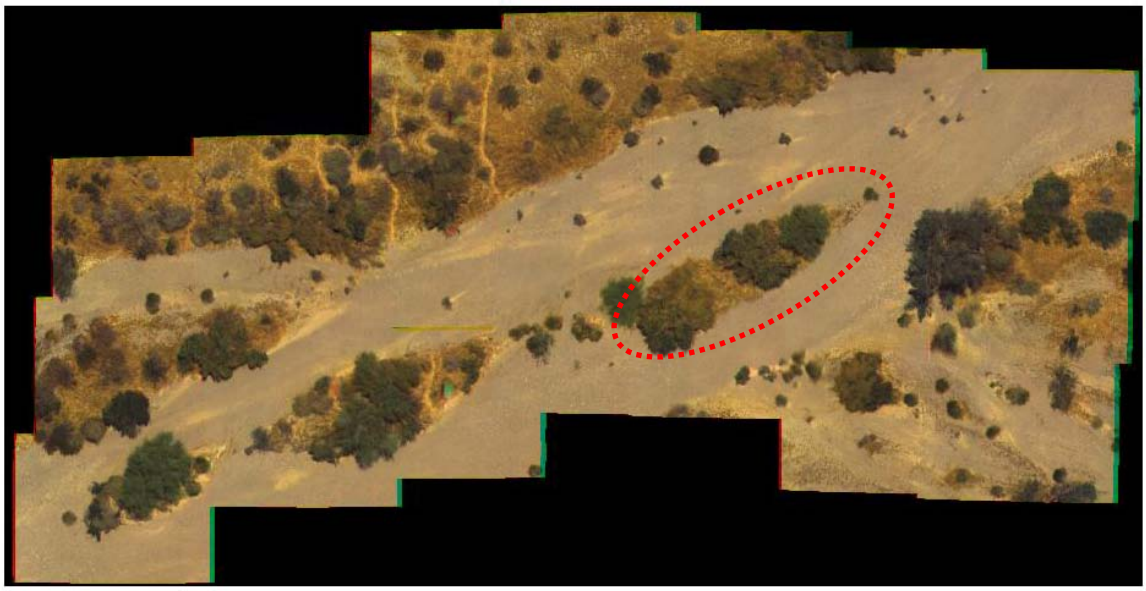

Figure 2.7. Afternoon Time MSI Registered Image Segment

The registration is possible due to the availability of Meta data as well as in-step and in-flight overlap between image frames. Due to the computation complexity of image based registration, it is desirable if part of processing can be done with registration based only on the geolocation in Metadata. However, the registration/reconstruction error will be worse in those cases when the overlap between image frames is not enough or cannot be used due to computational costs. The resulting larger registration error has bearing on minefield performance especially for patterned minefields since the detected mines may loose their linearity.

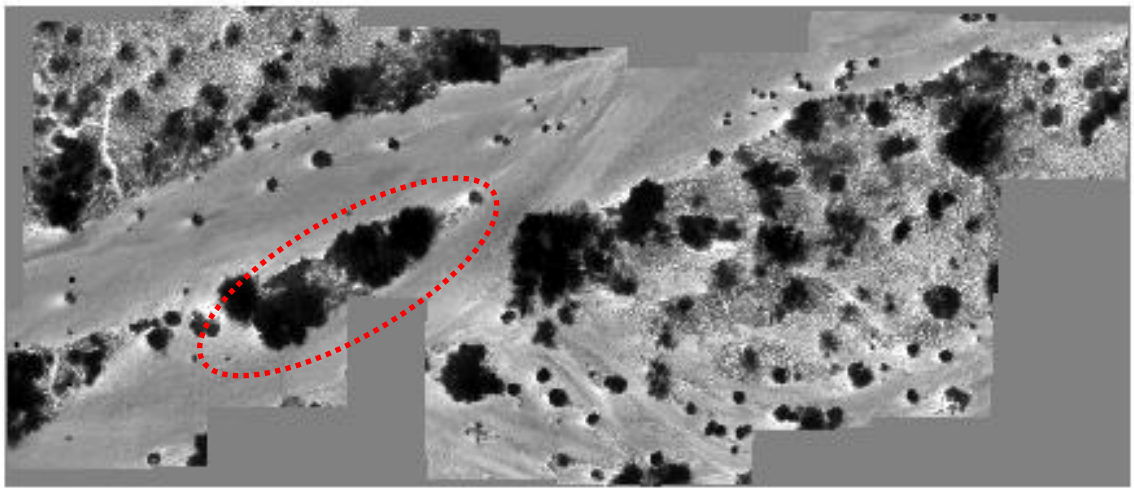

Figure 2.8. Afternoon Time MWIR Registered Image Segment

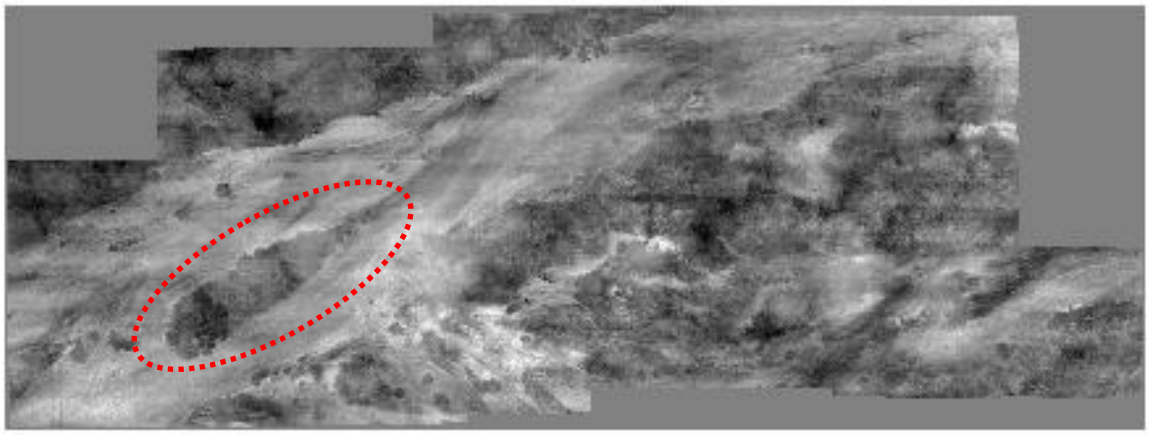

Figure 2.9. Night Time Segment for MWIR Data

Mine level detection of the mine like targets, can either be performed at the frame level or at segment level. However, some prejudice might be associated at the frame level calculation due to duplication of the false alarms in adjacent (both in-step and in-swath) frames resulting in biased performance because contribution from one false alarm may be recorded multiple times. Because of this reason, good registration is important in order to accurately transform these individual frames in a single coordinate system. Thus

reconstruction is also the method by which the anomaly detections of individual frames are resolved to identify unique detections in FoR.

2.2. MINE DETECTION

The purpose of mine detection block is to detect the location of potential mines once the anomaly values are assigned to each pixel. Mine detection step is intermediate step before the minefield detection that provides the information about the detection of mine like targets along with certain inevitable false alarms. Mine detection depends on a slew of factors including the type of sensor(s), target signature (signal to clutter ratio), size of the target, resolution of the sensor, type of the background, and the algorithm (anomaly detection, false alarm mitigation methods) used.

In the proposed simulation system, only a set of potential mine locations and potential false alarm locations are simulated. Thus it is important to assign an appropriate anomaly detection statistics to the mine and false alarm points. Different models for the distribution of anomaly detection statistics can be used which depend on the detection algorithm. One of the popular algorithms used for anomaly detection is RX [Reed and Yu, 1990]. The corresponding detection statistics under the white Gaussian background follow the central F-distribution. However, the distribution of RX detection statistics can be quite different for a more general background due to cultured clutter and spatial correlation in the background data that influences the system performance. One of the major reasons for deviation from the ideal behavior is the assumption of a white Gaussian background, that is not always true due to the presence of different classes of terrains [Stein et al., 2002], and the presence of multi resolution feature spaces [Noiboar and Cohen, 2007]. A number of other distributions for anomaly detectors are proposed based on different features which are discussed in Section 4.5.

The performance of the sensor at the mine level detection is parameterized in terms of the probability of detection (PD) and corresponding false alarm rate (FAR) (false alarms per m^2). A mine level ROC (Receiver Operating Characteristic) curve is drawn showing the mine level performance in terms of PD and FAR. The issue in this case of mine detection performance modeling is to develop a model for the selected mine detection algorithm to assign proper test statistics to mine and false alarm detections and

estimate mine level performance (in terms of PD and FAR) for a given sensor, target, and background under reasonable assumptions.

2.3. THRESHOLDING AND TARGET SELECTION

The anomaly detection algorithm assigns a confidence value or some other metric to a point being a likely mine. The next step is to threshold the list of these locations to obtain the set of valid anomalies that are statistically distinct from the neighboring background and highly prospective mines. These sets of anomalies are then passed for the minefield level processing. Another reason for the performing thresholding operation is to effectively reduce the number of targets that will be passed for the minefield detection. Thresholding algorithms used for the selection of targets affect the minefield detection performance. Three different thresholding schemes are discussed in section 3.3. False alarm mitigation (FAM) techniques can also be applied before passing the thresholded targets for the minefield level processing. FAM techniques try to reduce false alarms by exploiting the shape, photometric, polarity, spectral and other properties of the mine targets to reject likely false alarms. Detailed FAM techniques are discussed in [Menon 2005]. However for present implementation, these techniques are not modeled.

2.4. MINEFIELD DETECTION

Locations of targets obtained after target selection and thresholding are then used to detect the presence of the minefield and eventually evaluate the minefield confidence metric for the given FoR. The minefield detection performance depends on the type of minefield, characteristics of the background, mine level performance and the minefield algorithm. In a typical implementation separate algorithms are used for patterned and scattered minefields. Numerous algorithms are available in the literature for these two types of minefields. The empty boxes test (EBT) algorithm [Lake et al., 1997], linear pattern detection [Malloy, 2003; Muise and Smith, 1995], robust mine detection algorithm [Robins and Robinson, 1995], and Hough line transforms [Carlson et al., 1994] are some of the patterned minefield detection algorithms available in the literature. Scatter Number [Earp, 2000b] and Scatter Log weighted [Earp et al., 1995] are some of the techniques used for scattered minefield detection.

The performance of the system at the minefield detection level is defined in terms of the minefield probability of detection and the corresponding false alarm rate (false alarms per km^2). The system specifications are often defined in terms of the operating point on this curve. Another factor that may impact the evaluation of minefield performance is the minefield scoring method used. Two possible scoring methods are also discussed in Section 3.4.

3. SIMULATION SYSTEM

This section presents an overview of the simulation system which is being used to simulate and evaluate the performance of a typical airborne minefield detection system. A graphical user interface called "*SimulAMFD*" is developed to facilitate this evaluation [Agarwal and Agarwal, 2006]. The GUI provides an input interface between the user and the modeling software and allows the user to specify different design parameters, evaluate mine and minefield level performance, and analyze individual mine and minefield detection algorithms. This simulation system estimates airborne mine and minefield performance under different sensor and minefield layout scenarios. The methodologies and models used for data collection, mine detection, and minefield detection are discussed below separately. The simulation system allows estimating mine and minefield level performance for a particular choice of data collection parameters and algorithms. It is also possible to compare analytical and simulation-based results for selected detection scenarios for validation purposes. The simulation system also has the flexibility to conduct design trade-off by comparing performance between different choices of sensor-related parameters.

3.1. DATA SIMULATION

Data collection is the first step for any minefield detection system. The data for the simulation are generated in a manner that closely resembles the data collection in various airborne minefield detection programs. A large number of parameters are involved in the simulation of data for an airborne minefield detection system. Most of these parameters are used to model the flight path over the simulated background and minefield scenario. Table 3.1 gives a list of the parameters needed for modeling and analysis of data collection scenarios. The parameters shown in Table 3.1 are directly provided to the simulation system. A number of other parameters are also used, which are derived using these parameters. The input and derived parameters are discussed in the following subsections in more detail.

Table 3.1. Data Collection Parameters for Simulation

DATA COLLECTION PARAMETERS			
Platform Data	**Sensor and Gimbal Data**	**Background Data**	**Minefield Data**
Nominal Flight Speed (*V*)	Camera Resolution (*NxM*)	Length	Minefield Layout
Variation in Flight Speed	Camera Orientation	Breadth	Minefield Distribution
Nominal Flight Altitude (*A*)	FOV (FOV_x , FOV_y)	Background Anomaly Density	Minefield Position
Variation in Flight Altitude	Frame rate (*H*)	Spatial Distribution	Mine Size and Material
Flight Angle	Number of Steps per FoR (*s*)	Anomaly Statistics	Mine Statistics
Flight Position	Side step Overlap (λ_y)		
	Number of Swath per FoR (*S*)		

3.1.1. Platform Data. The flight speed (knots) and corresponding variation are provided directly in the simulation tool. Similarly, the flight altitude (feet) and its corresponding variation are also predefined. The flight angle in degrees is the heading angle of the flight with respect to the X axis on the ground. The flight angle can be a fixed number or may have some variation. The variations in flight speed, flight altitude, and flight angle can be modeled using Uniform or Gaussian distribution. For this, appropriate inputs (minimum and maximum values for Uniform distribution and mean, standard deviation values for Gaussian distribution) are provided to the simulation system. The flight position is the position where the flight path for a given run will start. Similar to the flight angle, the position can be a fixed X and Y locations or it can be distributed according to Uniform distribution for which the start and end positions for both the X and Y directions will be provided.

3.1.2. Sensor and Gimbal Data. The field of view, number of rows and columns, and altitude define the GSD, which in turn defines the target size. Camera Orientation defines the orientation for the data collection. It can be either 0 degree, which is the default orientation for step–stare data collection (in which the columns of an image frame are in the in-flight direction and the rows of an image frame are in the across- flight

direction), or 90 degrees, which is the default orientation for push broom data collection. The number of rows and columns define the size of an image frame. If the image size is given by NxM in pixels and FOV_x and FOV_y are the field of view in 'x' and 'y' direction, then resolution/ground sample distance (GSD) of the sensor (in inches), r is given as

$$r = \frac{\pi * A * FOV_x}{15M} = \frac{\pi * A * FOV_y}{15N} \text{ (inch)} \tag{3.1}$$

where altitude A is in feet and FOV_x and FOV_y are in degrees.

Now, the length (X) and width (Y) of the image (in meters) for the step-stare mode is given by

$$X = 0.0254rM \text{ , } Y = 0.0254rN \tag{3.2}$$

and for the push broom mode is given by

$$X = 0.0254rN, \quad Y = 0.0254rM \tag{3.3}$$

The frame rate is defined as the number of image frames per second and it is provided in Hz. The number of steps depends on the mode of the data collection. For the push broom mode, the number of steps is equal to one, whereas for the step stare mode, the number of steps is greater then one and is derived based on the requirements of swath width. Side step overlap λ_y can be controlled by the gimbal, and it is taken as an independent variable. A positive value of λ_y represents the corresponding fraction of overlap between images in the direction perpendicular to the flight, and a negative value represents a holiday (or a gap) between frames. The number of steps and side step overlap along with other parameters define the swath width which determines the width of the minefield encountered in the run and has bearing on the minefield detection. The swath per FoR is predefined number that dictates the length of the FoR.

In-flight overlap depends on the frame rate of the sensor, the flight speed, and the frame length. The in-flight overlap λ_x is given by

$$\lambda_x = 1 - \frac{Vs}{1.94384XH} \tag{3.4}$$

where V is the flight speed in knots, s is the number of steps per swath, and H is the frame rate of the sensor in Hz. The swath width W and length L of an FoR is then calculated as

$$W = (1-\lambda_y)sY + \lambda_y Y\,,\; L = (1-\lambda_x)SX + \lambda_x X \tag{3.5}$$

where S is the number of swaths per FoR.

3.1.3. Background Data. Background data such as length, breadth (meters), and anomaly density (per meter square) are directly provided to the simulation system. Length and breadth define the size of the simulated background area. A set of parameters is needed to be provided to define distribution of anomaly statistics. Different anomaly detection (AD) algorithms can be used to generate AD values for the simulation. The anomaly statistics are dictated by the AD algorithms. AD algorithms calculate the test statistics at all the pixel locations on the image to find those pixels which are statistically different from the background. This test statistics depends on number of factors such as background type, AD algorithm used, time of the day, etc. This test statistics can then be modeled using various statistical distributions. RX is one of the most popular AD algorithms, whose test statistics can be modeled by Beta distribution or Gamma distribution as explained in [Ganju, 2006]. Another distribution that can be used to model the RX anomaly values is central F distribution which is used in this thesis and discussed in Section 4.3. Distributions, other than these can also be used to model the test statistics. Thus, for modeling the anomaly values, input parameters corresponding to a particular distribution are provided as inputs to the simulation system. The parameters can be degrees of freedom (numerator, denominator) for a central F distribution, shape parameters for a two-parameter Beta distribution, and a shape parameter and scale

parameter for a two-parameter Gamma distribution. Spatial distribution deals with statistical models that can be used to model the spatial locations of these anomaly values. Similar to anomaly statistics, spatial distribution requires inputs for some mathematical (or statistical) models used to model the spatial locations of the background anomaly values. Poisson distribution is currently implemented to model the spatial distribution of background anomaly.

3.1.4. Minefield Data. In the present tool, nine from many possible minefield templates used in minefield deployment [FM 20-32, 1998] have been implemented. Among these, scattered and patterned minefields are the two most commonly used templates. Figures 3.1 and 3.2 show representative spatial distributions of the two minefield templates, respectively. For patterned minefield, mines are arranged in a three rows that are not necessarily straight or linear.

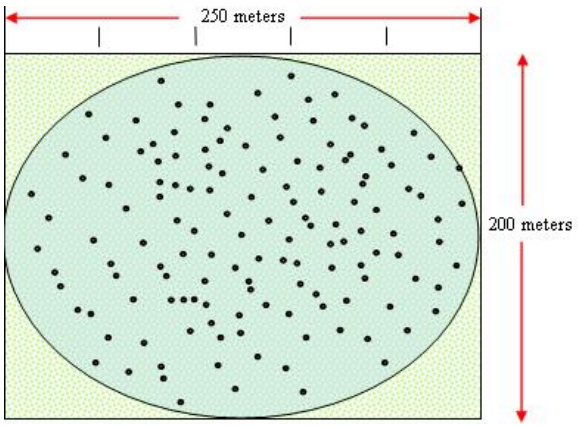

Figure 3.1. Minefield Template Used for Generating a Scattered Minefield

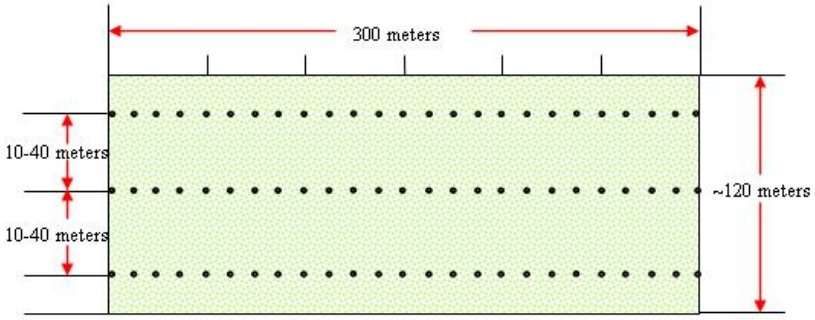

Figure 3.2. Minefield Template Used for Generating a Patterned Minefield

The minefield position provides information about the locations where a minefield is placed in the simulated background. Mine statistics describe various statistical models that are used to model the anomaly detection statistics at the locations of mines. Similar to the false alarm statistics, a set of parameters is needed to be provided for the distribution of mine statistics. One such model is discussed in section 4.1.

Figures 3.3 and 3.4 represent simulated runs. Figure 3.3 shows a simulated run in which the segment passes over the minefield completely and thus constitutes a minefield segment, whereas in Figure 3.4 the run completely misses the minefield. The flight angle is assumed to be uniformly distributed with the minimum and maximum flight angle $(\pm\Delta\theta)$ specified as $\pm 10^0$. The altitude and flight speed is assumed to be constant and kept at 2050 ft and 75 knots, respectively. The flight position is also assumed to be uniformly distributed along the '*x*' direction (minefield depth) and kept constant along the '*y*' direction (minefield front). The background point locations are simulated as Poisson distribution with a specified density. A part of these background points constitute the mine level false alarm for the background. In the current simulation, a density of 0.01 background points per meter square is used because in most cases the highest false alarm rate considered at the mine level is 0.01 FA/m^2. The minefield layout of a patterned or scattered minefield is designed according to specified templates. In all simulations, the flight path is taken to be approximately perpendicular to the minefield front. However, a variation of approximately 15^0 is allowed. Green dots (.) represent the background clutter, and red diamonds represent the mines. Represented segments and frames are also highlighted along with the flight start position and flight angle.

3.2. EVALUATING MINE LEVEL PERFORMANCE

Once the data are generated corresponding to the provided parameters, the next step is to evaluate the mine level performance. Mine level performance depends on the AD algorithm (such as RX etc.) which is captured by the Figure 2.1. The anomaly values obtained from the AD algorithm are thresholded and for each threshold, the probability of detection (PD) of a mine and corresponding false alarm rate (FAR) are calculated. The PD and FAR depend on the distribution of the anomaly values for the false alarm and mine targets. Mine level ROC curves are then drawn to plot the PD against the FAR.

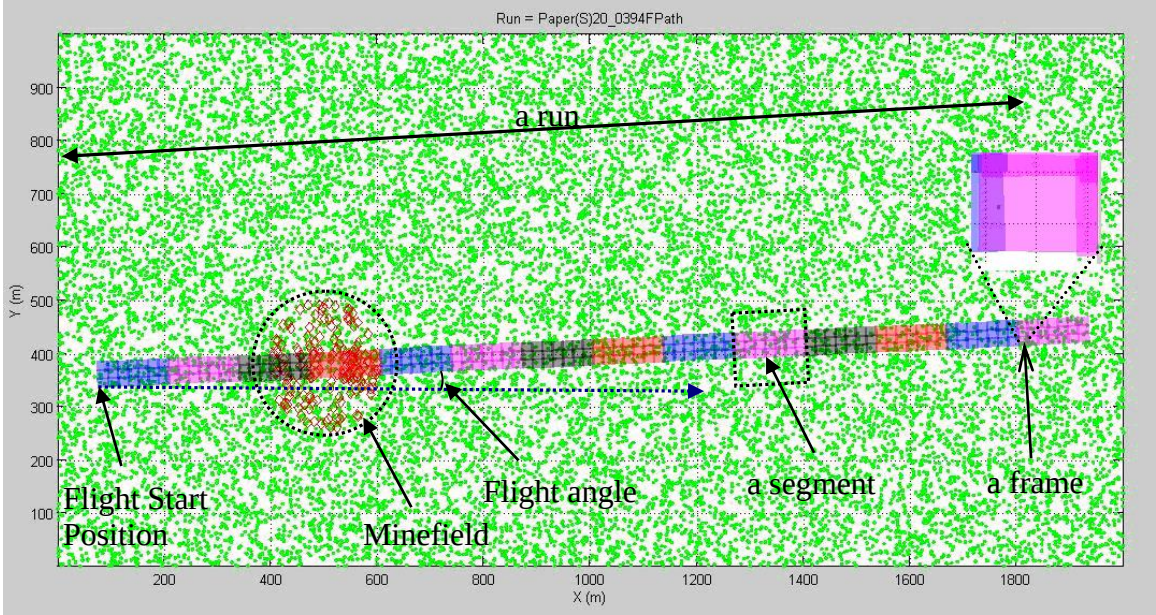

Figure 3.3. Simulated Run Passing Over the Minefield Completely

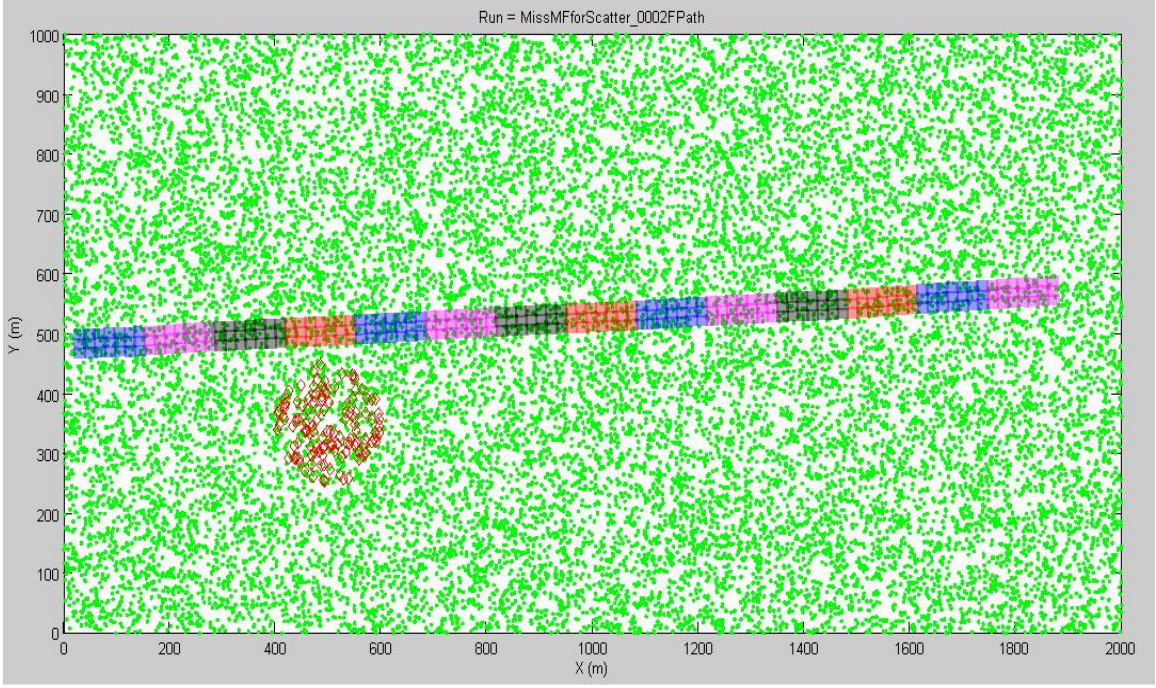

Figure 3.4. Simulated Run Missing the Minefield Completely

3.3. THRESHOLDING SCHEMES

The anomaly detection values are thresholded to obtain the set of most likely anomalies which are statistically distinct from the neighboring background. The threshold plays a significant role because the targets selected at this level participate in the minefield level detection. The selected targets should be such that a reasonable number of false alarms are passed while selecting certain levels of mines for effective minefield detection. A number of thresholding schemes for this purpose can be used. Each thresholding scheme affects the probability of minefield detection and corresponding false alarm rate in a different manner. Three different thresholding methods are discussed in this section.

3.3.1. Fixed Threshold. This is a straightforward scoring approach in which only the targets with detection statistics above the specified threshold are allowed to take part in scoring. The threshold is provided by the user in the modeling tool. This scoring approach provides reasonable performance for the cases where the non-maximal suppressed anomaly values follow almost the same statistical distribution for all FoRs. Thus, this scoring scheme can yield very good minefield detection performance if the background is homogeneous. It is, however, often impossible a priori to select an appropriate value of threshold because a desired value of the threshold may differ from terrain to terrain due to differences in the background data. The threshold will also depend on the time of day due to shadows and other effects. Moreover, due to the difference in background features from one FoR to another, the number of detections may be very large in some FoR and very small in other FoR.

3.3.2. Constant Target Rate. The constant target rate (CTR) implies that in each FoR, a fixed number of target locations with the highest detection statistics are selected. Number of targets is provided as an input in the modeling tool. Effectively the detection threshold changes from one FoR to another FoR in this case, depending on the selected target rate per FoR. The minefield level performance becomes subjective for this thresholding scenario because the number of false alarms selected per FoR remains same irrespective of the type of terrain. The minefield detection in this case should rely on a metric different then the number of detections. The detection of mines for this thresholding scheme may result in poor performance in a non-homogeneous background

because the probability of selecting some fixed number of mine targets in a highly cluttered area will be less than the probability of detecting the same number of mine targets in a low cluttered area. Moreover, if the number of targets is not selected appropriately, then it may result in poor minefield performance as well. Thus, this scheme can be used effectively for homogeneous background, but not for non-homogeneous background due to the above stated reasons.

3.3.3. Constant False Alarm Rate. In CFAR case, the detection statistics are modeled by appropriate distribution and a threshold is selected for a desired false alarm rate. The false alarm rate per square meter (ρ_B) is specified. In this thresholding scheme, the expected number of false alarms in a selected area is a constant which depends on the type of distribution that is used to model the detection statistics and the goodness of fit of the model. For each segment, the detection statistics are modeled by an appropriate distribution and the threshold is selected adaptively as shown in [Ramachandran, 2004].

A particular false alarm rate can be used depending on the type of background and terrain. If the background is highly cluttered then it can be anticipated that for a higher detection of mine targets, the false alarm rate should be higher. In contrast, for areas with low natural clutter, a lower false alarm rate can be used to achieve higher detection of mine targets. Thus, CFAR is a very effective scheme for thresholding mine targets, resulting in possibly better mine and minefield detection performance.

3.4. EVALUATING MINEFIELD LEVEL PERFORMANCE

This is the final step in a typical airborne minefield detection system. The minefield level performance depends on the minefield detection algorithm, mine level performance, thresholding scheme, and the minefield scoring method used. Because most of the mines are either scattered or laid in a pattern in a minefield, most of the minefield detection algorithms provide an indication of presence in the form of a minefield confidence metric, which is a quantitative measure of the confidence level for the presence or absence of a minefield in that area. The thresholded anomaly values, along with their spatial locations, are provided as an input to these minefield detection algorithms over which the minefield confidence metric is derived. Various algorithms that are currently being implemented are pattern linear, pattern regular for a patterned

minefield, and scatter number and scatter log weighted for a scattered minefield. These algorithms are explained in detail in Section 7.

Once the minefield level confidence values are obtained the next and final step is to score the minefield for its performance evaluation in terms of an ROC curve. This ROC curve will then represents the probability of detection against the probability of false alarm for a minefield. The minefield confidence statistics effectively represent the likelihood that a minefield is present in this FoR or the likelihood that the given FoR is collected over an actual minefield. These FoRs may be non-overlapping, or a sliding window approach is used to define an overlapping FoR. Scoring can be done either for a segment/FoR or a complete run. Both of these scoring methods are currently implemented in the simulation system.

In scoring the detection performance, the simplest approach is to identify FoRs that are actually over the minefield to establish the ground truth. Once this ground truth is established, each FoR can be scored as a detection or false alarm, and an ROC curve can be drawn. For FoR-wise minefield scoring, one input is required in the simulation system. If the input is between 0 and 1(inclusive), then the ratio of the area occupied by the mines to the area of the FoR should be greater than the input to be called a minefield FoR. However, if the number is greater than 1, then that many mines should be detected in a FoR for it to be called a valid minefield FoR. The main problem with this approach is that at times an FoR may only be partially over the minefield. In such cases one would have to make an arbitrary choice of when to call a given FoR as belonging to a minefield and when not to do so. The evaluated performance is significantly dependent on this choice. Moreover, the resulting ROC curves give the probability of correct classification of the FoR and not the probability of detection of the minefield.

An alternative, slightly complicated, but more representative approach is to score the runs and not the individual FoR. In this case the scoring is based on actual geo-locations of a minefield. The minefield is defined by its location and extent. Any run that intercepts the minefield suitably is said to be a minefield run. In practice, one run can have more than one minefield, which would be evaluated as independent minefields. A minefield is said to be detected if any FoR that falls over the minefield is flagged as containing a minefield. Multiple detections over the same minefield location are

neglected. A similar approach is followed for false alarms. Any FoR that does not intercept a minefield is a likely candidate for a false alarm. However, multiple false alarms that hit in the same area of the field are neglected. Thus, once an FoR is called a false alarm, any other FoR within a specified distance from this FoR will not be counted as a false alarm. It is important to note that the length of this distance over which further false alarms are neglected does not affect the measured false alarm rate; it only limits the maximum false alarm rate that could be reported. Any reasonable size such as 100m or 200m can be used. However, the size should be at least as long as the length of an FoR. If the scoring is done over the complete run, then any FoR having more than zero mine targets can be defined as a valid minefield segment.

4. ANOMALY DETECTION — MODELING RX STATISTICS

AD algorithm calculates the detection statistics at all the pixel locations on the image to find the pixels that are statistically different from the background. This section discusses the modeling of the statistics for an Anomaly Detection (AD) algorithm. RX is one of the most popular algorithms for anomaly detection [Reed and Yu, 1990; Holmes, 1995]. Modeling of the detection statistics for RX algorithm is discussed in this section. Further processing such as False Alarm Mitigation (FAM) can then be used to segregate the possible mine targets from the false alarm depending on various feature classification algorithms such as circularity, radial symmetry, and gray scale moments [Menon et al., 2004]. For the present discussion, the RX algorithm is used to detect the possible mine targets from the background anomaly. False alarm mitigation has not been currently implemented.

4.1. MODELING RX ANOMALY DETECTOR

Various anomaly detection algorithms are proposed for mine level detection in the literature such as RX [Reed and Yu, 1990; Holmes, 1995], and Unmixing Component Analysis [Yanfeng et al., 2006]. An optimal matched response based on a locally estimated first-order Gauss-Markov model for the background and known mine template has been proposed by Liao et al. for anomaly detection [Liao et al., 2001]. For the current discussion, the anomaly detection algorithm considered is RX. The RX algorithm has become the de-facto baseline anomaly detector. This algorithm assumes the available images to be zero mean, uncorrelated, and Gaussian distributed. This assumption is fair enough for most of the low-resolution electro-optical sensors (although many images are not truly Gaussian distributed). By definition, images are not zero mean; however, real images can often be assumed to have a slowly varying mean value. A non-stationary local mean can be subtracted from the image to generate a locally zero mean image, which is then passed through the RX anomaly detector. The RX detector then provides the statistical measure for the presence of an anomaly at each pixel location in the image. However, all pixel RX values are not used because local neighborhood values are often correlated in case of high resolution images. Instead the local maximum in the

neighborhood can be considered as viable anomalies. This is achieved by non-max suppression, which can be viewed as a filter process that only allows the maximum value in a given neighborhood to pass while suppressing all the other RX values. A detailed explanation of the RX anomaly detector and the working of non-max suppression can be found in [Ramachandran, 2004]. This section presents a brief overview of the RX algorithm and outlines its functional working.

The RX algorithm involves three sets of masks: the target mask, the blanking mask, and the demeaning mask. Figure 4.1 shows the geometry of the three masks used in the current implementation. Square or rectangular mask can also be used. The target radius (r_T) defines the target mask (W_T), which defines the size of the target signature, which is assumed to be circular in shape. The annular region between the target radius and blanking radius (r_B) defines the blanking mask and specifies the region that is omitted from the estimation process. This region is excluded because it may typically contain shadows and other reflective effects of the target. Inclusion of this region can distort the target and clutter estimates. The third mask is the clutter mask, which is defined as the annular region between blanking radius (r_B) and demeaning radius (r_D), which defines the extent of the background that is used to compute the background covariance. This demeaning radius also defines the demeaning mask, which is used to compute the local mean for local demeaning of the raw image.

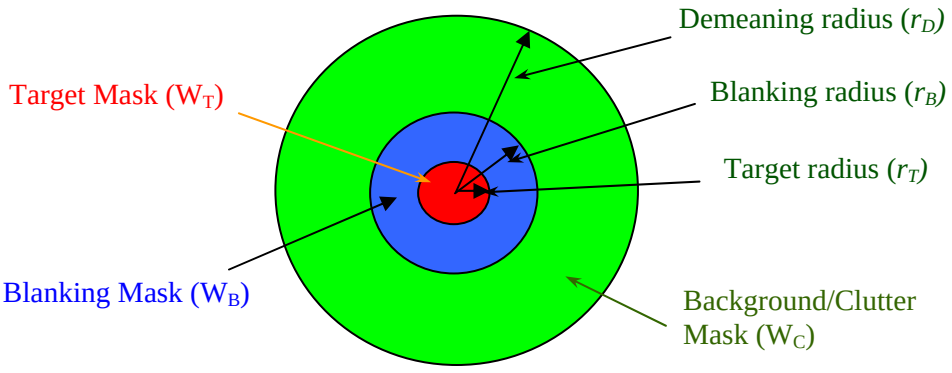

Figure 4.1. Geometry of Masks in RX Anomaly Detection

The target radius and demeaning radius are independent of each other and provide a good estimate of the target statistics and background statistics, respectively. Effectively this RX algorithm accepts the raw image as an input and calculates the convolution with the set of the above three masks. Thus, what is being computed is effectively the signal to clutter ratio for each pixel in the image. The RX output provides an image equal in size to the size of the actual image.

The RX algorithm is generally applicable for multi-band images with zero mean and uncorrelated Gaussian background [Reed and Yu, 1990]. For an image pixel $I(i, j) = I_l$, the RX statistics r for a J band image is given by

$$r = \mu_S^T M^{-1} \mu_S \tag{4.1}$$

where M is the scaled local covariance matrix and μ_S is the target signature given by

$$M = \sum_{l \in W_C} I_l^T I_l , \qquad \mu_S = \frac{1}{\sqrt{N_T}} \sum_{l \in W_T} I_l$$

where $N_C = \pi(r_D^2 - r_B^2)$ and $N_T = \pi r_T^2$ are the number of clutter and target pixels used in estimating M and μ_S respectively.

The scaling of RX statistics presented here is slightly different from that used in other literature [Menon, 2005; Ganju, 2006] to ensure consistency with the origin RX paper [Reed and Yu, 1991]. The difference arises because of the way M and μ_S is defined. The RX statistics 'r' used here can be written as

$$r = (N_T / N_C) r_X$$

where r_X is the RX statistics defined in [Menon, 2005; Ganju, 2006].

Under the assumption of zero-mean uncorrelated Gaussian variable, the probability density functions obtained by Reed and Yu [Reed and Yu, 1990] for the RX statistic for the background location and the target location is given by,

$$f(r \mid H_0) = \frac{r^{\left(\frac{J-2}{2}\right)}}{B\left(\frac{N_c - J}{2}, \frac{J}{2}\right)(1+r)^{(N_c/2)}} \tag{4.2}$$

$$f(r \mid H_1) = \frac{r^{\left(\frac{J-2}{2}\right)} e^{\left(-\frac{a}{2}\right)} {}_1F_1\left(\frac{N_c}{2}; \frac{J}{2}; \frac{ar}{2(1+r)}\right)}{B\left(\frac{N_c - J}{2}, \frac{J}{2}\right)(1+r)^{(N_c/2)}} \tag{4.3}$$

where $f\left(r \mid H_0\right)$ is the probability density function for *x* given that it is not a mine target (null–hypothesis) and $f\left(r \mid H_1\right)$ is the probability density function given that the pixel location belongs to a mine (non-null hypothesis). $F_1(x; y; z)$ is the confluent hypergeometric function, N_c denotes the number of pixels in the clutter template in the neighborhood, J represents the number of bands, and $B(\gamma; \eta)$ denotes the beta density function. The generalized signal to noise ratio (GSNR) or scale factor 'a' is given by

$$a = (SCR) J N_T \tag{4.4}$$

$$SCR = \frac{\bar{\mu}^2}{\sigma^2} = \sum_{i=1}^{J} \mu_i^2 \Big/ J\sigma^2 \tag{4.5}$$

where $\bar{\mu}$ is the mean target signature, σ is the standard deviation of the background area, and N_T is the number of pixels in the target template.

The RX statistics for background location and target location given by Equation (4.2) and Equation (4.3) can also be modeled by the central F and non-central F distribution. The central F distribution is defined as the ratio of two central chi squared variates and non-central F distribution is defined as ratio between non-central chi square and central chi square variates. Central F and non-central F distributions are defined as [Johnson et al.,1995]:

$$f(x:v_1,v_2)=\frac{\left(\frac{v_1}{v_2}\right)^{\frac{v_1}{2}}x^{\frac{v_1}{2}-1}}{B\left(\frac{v_1}{2},\frac{v_2}{2}\right)\left(1+\frac{v_1x}{v_2}\right)^{\frac{v_1+v_2}{2}}},\quad 0\le x;v_1,v_2>0 \tag{4.6}$$

$$f(x:v_1,v_2,a)=\frac{e^{-\frac{a}{2}}\left(\frac{v_1}{v_2}\right)^{\frac{v_1}{2}}x^{\frac{v_1}{2}-1}{}_1F_1\left(\frac{v_1+v_2}{2},\frac{v_1}{2},\frac{v_1a}{2(v_2+v_1x)}\right)}{B\left(\frac{v_1}{2},\frac{v_2}{2}\right)\left(1+\frac{v_1x}{v_2}\right)^{\frac{v_1+v_2}{2}}},\ 0\le x;v_1,v_2,a>0 \tag{4.7}$$

where v_1 is the numerator degrees of freedom (and denominator degrees of freedom ($DOF_{N)}$ and v_2 is the denominator degrees of freedom (DOF_D) and a is the GSNR. Comparing Equations (4.2) and (4.6), the RX distribution under a null hypothesis can be easily transformed into central F distribution with transformation

$$x=r\frac{v_2}{v_1} \tag{4.8}$$

where $v_1 = J$ and $v_2 = N_C - J$ and $B(v_1/2, v_2/2)$ is the complete Beta function.

Thus, RX detection statistics can be modeled into an F distribution by scaling the detection statistics by $J/(N_C - J)$. However, due to a non-ideal environment and with different terrain types and local correlation in the background data, the statistics in

Equation (4.7) often does not follow F distribution. However it is postulated that a scaled RX statistics is defined as

$$x = k\frac{v_2}{v_1}r \tag{4.9}$$

may actually follow F distribution. This scale factor '*k*' is very similar to the scale factor 'λ' used in [Ramachandran, 2004]. This scale factor '*k*' also needs to be estimated. For the present case, the scaling is derived using the statistical method as described in Appendix C. Figure 4.2 shows some F distributions with different DOF_N and DOF_D.

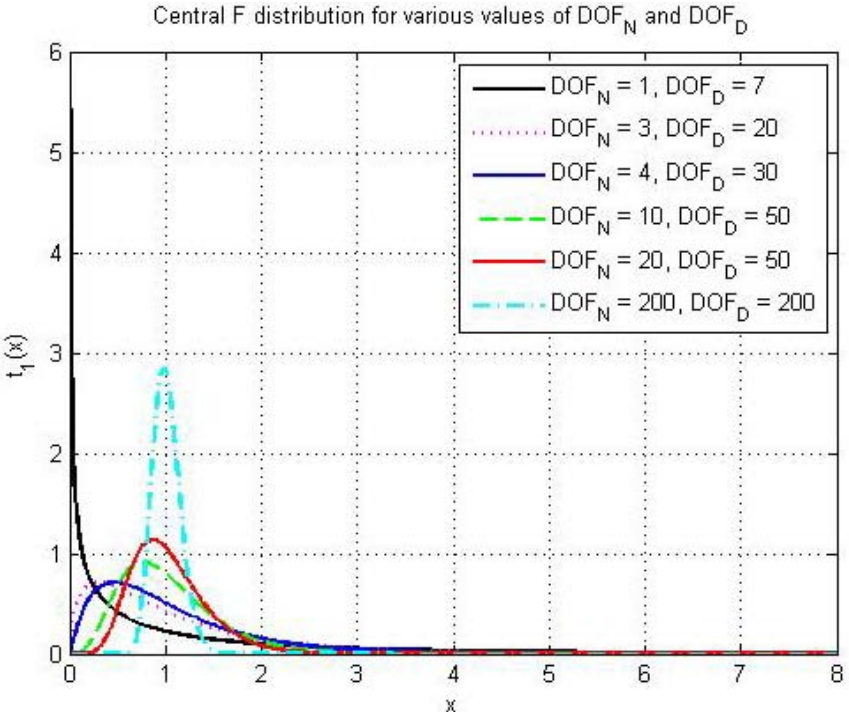

Figure 4.2. PDF for a Central F Distribution with Different Values of DOF_N and DOF_D

4.2. MODELING NON-MAX SUPPRESSION

The signal to clutter image obtained from the RX algorithm is subjected to non-max suppression to obtain the list of anomaly values which are highlighted by the

anomaly detector. Non-maximal suppression is a processing algorithm that suppresses (makes zero) all the targets in a specific neighborhood (*R*-pixel radius) except the local maximum. The target list so obtained is effectively the list of row and column coordinates of the potential targets along with the AD values at respective row and column values. The operation of non-maximal suppression can be explained with the help of Figure 4.3. Let the target location be specified by *l(i,j)* (marked by 'X' in the figure) and let *R* be the radius of the local neighborhood. Only the RX values inside the radius *R* will be considered for the non–maximal operation. The RX value at the central location *l* is set to zero if its value is not the maximum in this *R* pixel neighborhood; otherwise it is left as it is and will be a potential target. The same operation is repeated for each pixel location in the image and all local maxima are selected.

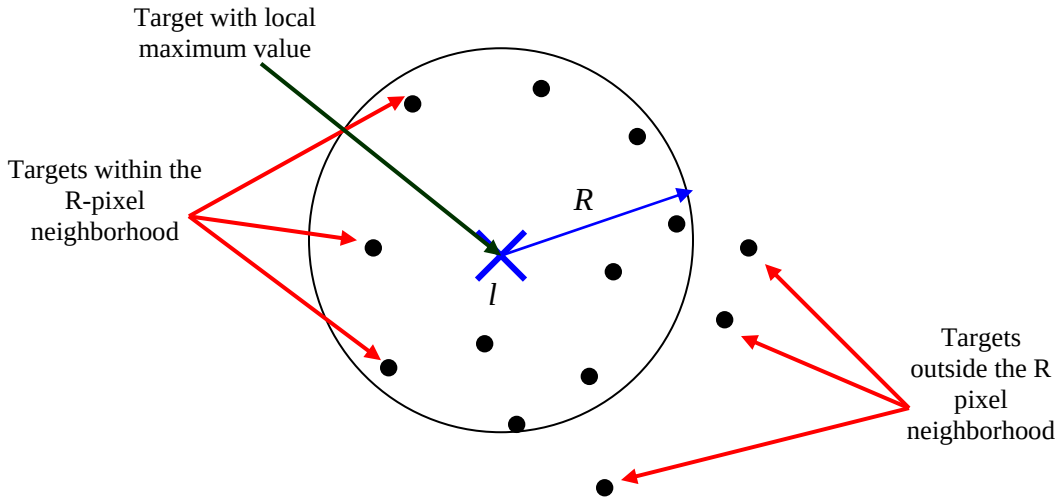

Figure 4.3. *R* -pixel Neighborhood Showing Potential Targets

Let the function *g(l)* represent the mapping function performed by the non-max operation, and let B_r be the *R*-pixel neighborhood. Thus,

$$g(l) = \begin{cases} 1 & if \quad x_l = X_l \equiv \text{local maximum in } B_r \\ 0 & elsewhere \end{cases}$$

If $f(x \mid H_0)$ is the probability density function (PDF) under a null hypothesis, then the probability density function used to model the background clutter statistics after non-max suppression is given by [Ramachandran, 2004]:

$$f^{NM}(x \mid g(l)=1, H_0) = \frac{f(x \mid H_0).e^{-N(1-F_0(x))}}{\int_0^{\infty} f(\bar{x} \mid H_0).e^{-N(1-F_0(\bar{x}))} d\bar{x}} \tag{4.10}$$

where $N = \theta A$ is the expected (average) number of independent targets present in the neighborhood B_r, A is the area of the neighborhood B_r, θ is the density of targets, and $F_0(x)$ is the cumulative distribution function (CDF) for $f(x \mid H_0)$ defined as,

$$F_0(x) = f(\bar{x} < x \mid H_0) = \int_0^{x} f(\bar{x} \mid H_0) d\bar{x}$$

Similarly, the probability density function used to model the mine target statistics after non-max suppression is given by:

$$f^{NM}(x \mid g(l)=1, H_1) = \frac{f(x \mid H_1).e^{-N(1-F_0(x))}}{\int_0^{\infty} f(\bar{x} \mid H_1).e^{-N(1-F_0(\bar{x}))} d\bar{x}} \tag{4.11}$$

where $f(x \mid H_1)$ is the PDF under non null hypothesis.

Figure 4.4 shows the post non-max F distribution for various values of DOF_N, DOF_D and *N*. As seen from the Figure 4.4, the distribution can take different shapes depending on the values of DOF_N and DOF_D. Also, a larger value of *N* has the effect of pushing the distribution towards larger values.

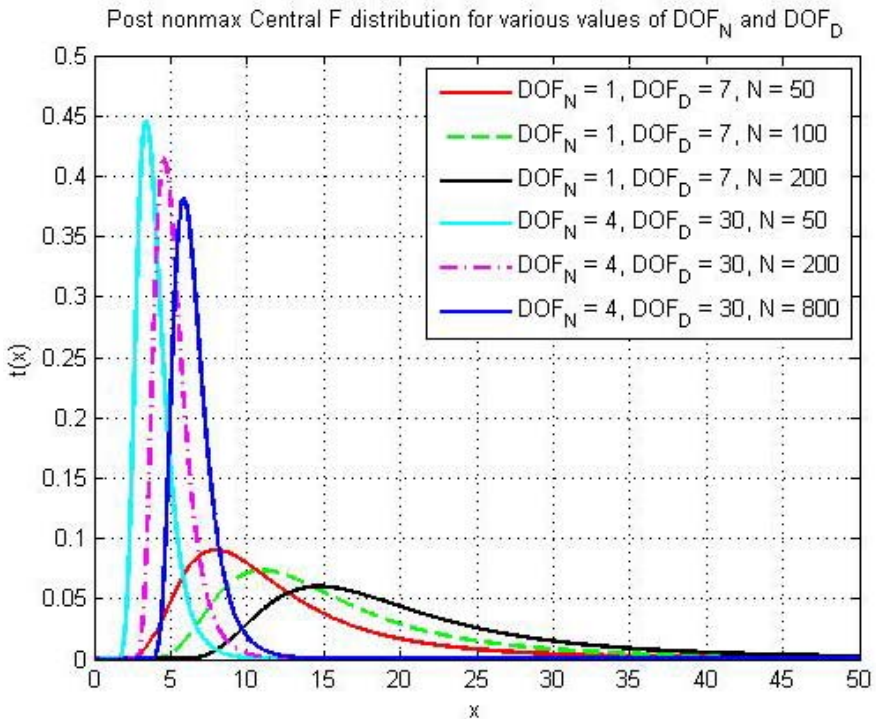

Figure 4.4. Post Non-max PDF for an F Distribution with Various DOF_N, DOF_D, and N

Figure 4.5 shows a simulated PDF of the background and mine RX statistics for different GSNR values after non-max suppression. As shown in the PDF, the detected number of mines and detected anomalies are different for a given threshold. The PDF for background RX values is drawn using Equation (4.10) and corresponding mine RX values is drawn using Equation (4.11). The background and mine RX values are assumed to be modeled as central F and noncentral F distribution, respectively. GSNR is responsible for the statistical difference in the background RX (blue) and mine RX (red, magenta and black) values, which is evident from the Figure 4.5.

4.3. PARAMETER ESTIMATION FOR RX DETECTIONS

Modeling of detection statistics is very useful because it provides valuable information about the spatial correlation and non-homogeneity in the data. In order to compare the performance of the RX anomaly detector for various terrains (sparsely vegetated, densely vegetated, and/or dirt) and for different times of day (morning time, afternoon time), it is very important to model the RX statistics using probabilistic models.

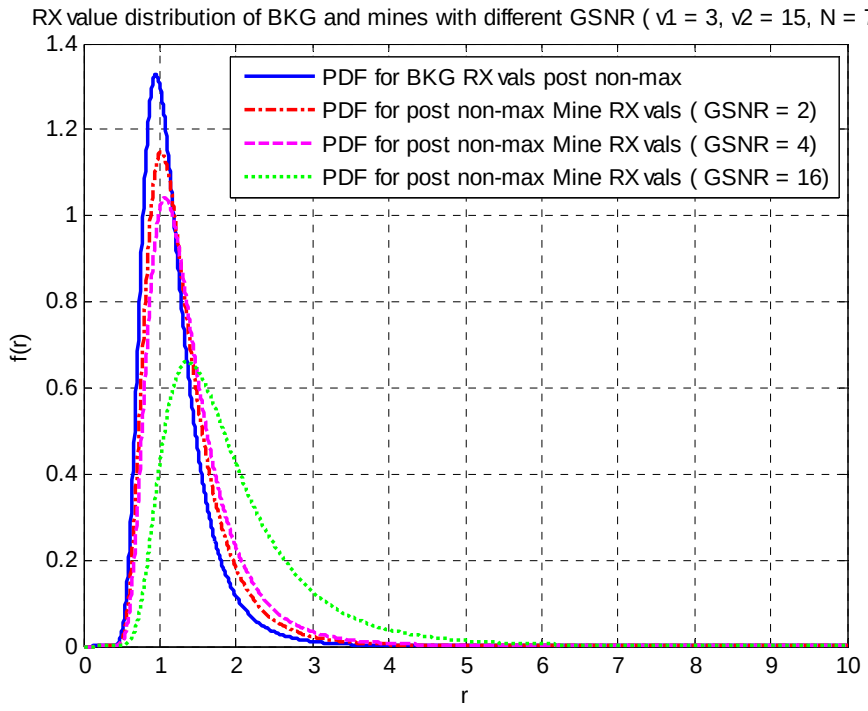

Figure 4.5. PDF for a Post Non-Max Background Anomaly and Mine Anomaly Statistic Value for Different GSNR Values

Previously, RX detection statistics have been successfully modeled using Beta and Gamma distributions [Ganju, 2006; Webb, 2000; Copsey and Webb, 2001; Huiyan et al., 2005]. In this section, the RX detection statistics will be modeled with a central F distribution. The model estimation for the central F distribution is done using the EM (**E**xpectation **M**aximization) technique. Various statistical tests are applied to check the goodness of fit of the modeled distribution with the actual data.

As explained in Section 4.1, the background RX statistics can be modeled by an F distribution i.e.,

$$f(r:v_1,v_2)=\frac{r^{\frac{v_1}{2}-1}}{B\left(\frac{v_1}{2},\frac{v_2}{2}\right)(1+r)^{\frac{v_1+v_2}{2}}},\quad \underline{0}<x;v_1,v_2>0 \tag{4.12}$$

where v_1 = J (number of spectral bands) and v_2 = $N_C - J$ (number of pixels in clutter template – number of spectral bands).

Once the non-max suppression is performed, the post non-max RX statistics becomes

$$f^{NM}(r; v_1, v_2, N) = \frac{f(r)e^{-N(1-F(r))}}{\int_0^\infty f(r)e^{-N(1-F(r))}dr}, \tag{4.13}$$

where $F(r)$ is the CDF of $f(r)$ and N is the number of pixels in the local neighborhood.

The EM algorithm is used to estimate the three parameters (v_1, v_2, and N) for the post non-max central F distribution. Initial parameters that are used to start the EM algorithm are very important and must be carefully chosen. Method of moments is currently used to derive the initial parameters. If there are '*p*' parameters to estimate, then the first '*p*' sample moments are equated to the actual moments of the distribution, given that the actual moments are functions of the parameters of interest. Other details and actual derivation for the initial parameters is discussed in Appendix C.

Estimation is carried out in two steps. The first step deals with the formulation of an update equation for the central F distribution and the second step explains the use of that update equation in estimating the parameters. Appendix B explains the EM algorithm with its mathematical formulation and update equation for estimating the parameters for RX modeling. Once the estimation is completed, various statistical tests are used to measure the goodness of fit of the estimated parameters. These tests are described in detail in Appendix D. The confidence level for the current results is taken to be 0.97. If the chi square test statistics for a particular segment is less than the threshold, then the segment is said to pass the test; otherwise the segment is said to fail the test. Here passing the test implies that a reasonable model is obtained for the RX statistics for the given segment. Thus depending on the confidence level, for the present case it is expected that 97% (because the confidence level is set to 0.97) of the segments for a given dataset will pass the test and 3% will fail. If the percentage of failure is much higher than 3%, then the modeling is bad; otherwise it is good.

4.4. MODELING RESULTS

As mentioned before, in the past RX statistics have been modeled using Beta and Gamma parameters. However in all previous work, frame-wise modeling has been used. For the present case, an attempt has been made at segment wise modeling of the RX statistics with a central F distribution. Estimation using Beta and Gamma distributions is still possible but has not been implemented here.

After the non-max operation there are about 350 samples in each frame. With 21 frames per segment, there are approximately 7000 samples per segment. However, all these samples are not used for modeling, instead, all the samples within 20 pixels of the four edges of the frames are ignored so as to remove the bias caused by corresponding edge pixels. This will reduce the total number of samples used for estimation.

The modeling is done for eight different types of datasets depending on the time of day (morning background segments, afternoon background segments) and background type (sparse vegetation background segments, dense vegetation background segments). Morning segments are chosen between 8:00 am and 9:00 am, and afternoon segments are chosen between 2:00 pm and 3:00 pm. For comparison between the background and minefield segments, both background only and minefield segments are used for the modeling.

For the background segments, all 21 frames (corresponding to seven swath and three steps) are used for the modeling. However, only clean frames (without any fiducial or manmade artifact) are used for modeling in case of the minefield segments. The minefield segments are visually inspected to ignore any frame with fiducials and other artifacts for the modeling purposes. Approximately 50 segments (equivalent to 1050 frames) are being used to generate the modeling results for all eight cases. Three different target radiuses (r_T) of zero, one, and two are used for comparison.

Modeling is done for both single band and multiband data. An individual MSI band 4 (NIR) is used to represent the single band data, and RGB colored band as well as all four MSI bands are used for the multiband modeling. Table 4.1 shows the number of segments and the exact number of frames corresponding to each dataset used for the modeling. Thus, a total of 24 sets (eight datasets and three target radii for each dataset) are being modeled and the fit is checked for the central F distribution.

Table 4.1. Data Type with Number of Segments and Frames Used for Modeling

	Number of Segments Used	**Total Number of frames used**
Morning Background Segments	40	40x21 = 840
Morning Minefield Segments	45	687
Afternoon Background Segments	40	40x21 = 840
Afternoon Minefield Segments	47	736
Sparse Vegetation Background Segments	80	80x21 = 1680
Sparse Vegetation Minefield Segments	50	790
Dense Vegetation Background Segments	59	59x21 = 1239
Dense Vegetation Minefield Segments	68	886

Figure 4.6 shows a representative segment from sparse vegetation background. The corresponding distribution fit for inverse CDF, and PDF is shown in Figure 4.7, for RGB colored registered segment and target radius, $r_T = 2$. The sample values for the F distribution are plotted on the '*x*' axis, and corresponding CDF and PDF values are plotted on the '*y*' axis. First subplot shows the inverse CDF for the actual RX values (blue) and the estimated values (broken red) and corresponding PDF is shown in the second subplot. Third subplot shows the chi square bin error values. Estimated and initial parameters for the EM algorithm are shown in the title of the second subplot of Figure 4.7. The initial 'v_1' and 'v_2' are derived using the method of moments as discussed in Appendix C. An initial value of *N* is chosen to be 100. The pass or fail value (one or zero, respectively) is also shown in the title of the third subplot of Figure 4.7.

Figure 4.8 shows a representative segment for a dense vegetation minefield segment and Figure 4.9 shows corresponding distribution fit for inverse CDF, and PDF for the actual and estimated samples along with the chi square bin error. The RGB colored segment with $r_T = 2$ is used for the distribution fit in this case also.

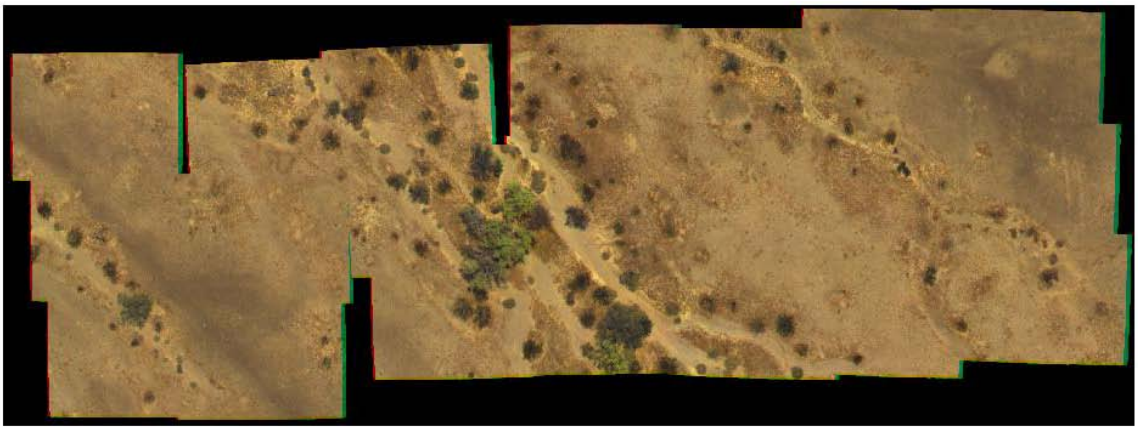

Figure 4.6. Sparse Vegetation Background Segment

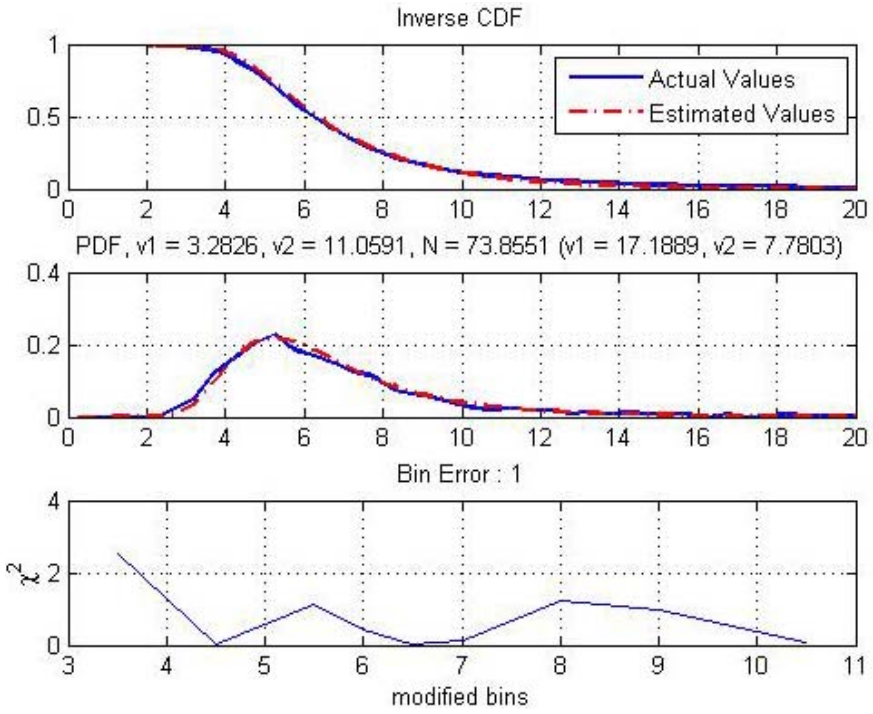

Figure 4.7. Distribution Fit for a Sparse Vegetation Background Segment

Tables 4.2 - 4.9 show the pass percentages for sparse vegetation background segments, dense vegetation background segments, sparse vegetation minefield segments, dense vegetation minefield segments, morning background segments, afternoon background segments, morning minefield segments, and afternoon minefield segments, respectively.

The frames with fiducials are ignored through visual inspection of the frames for the modeling purposes in the case of minefield segments to prevent any biasing caused due to the fiducials.

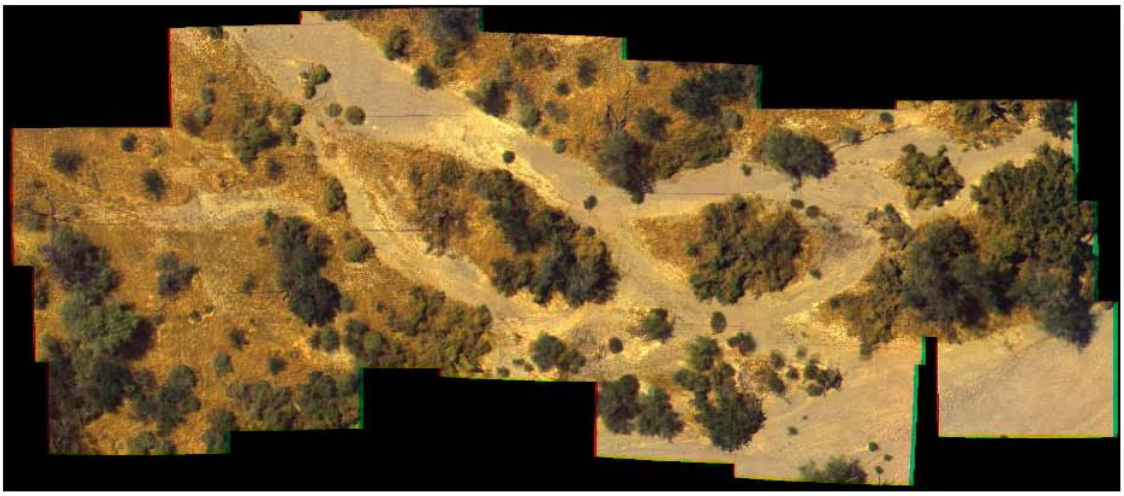

Figure 4.8. Dense Vegetation Background Segment

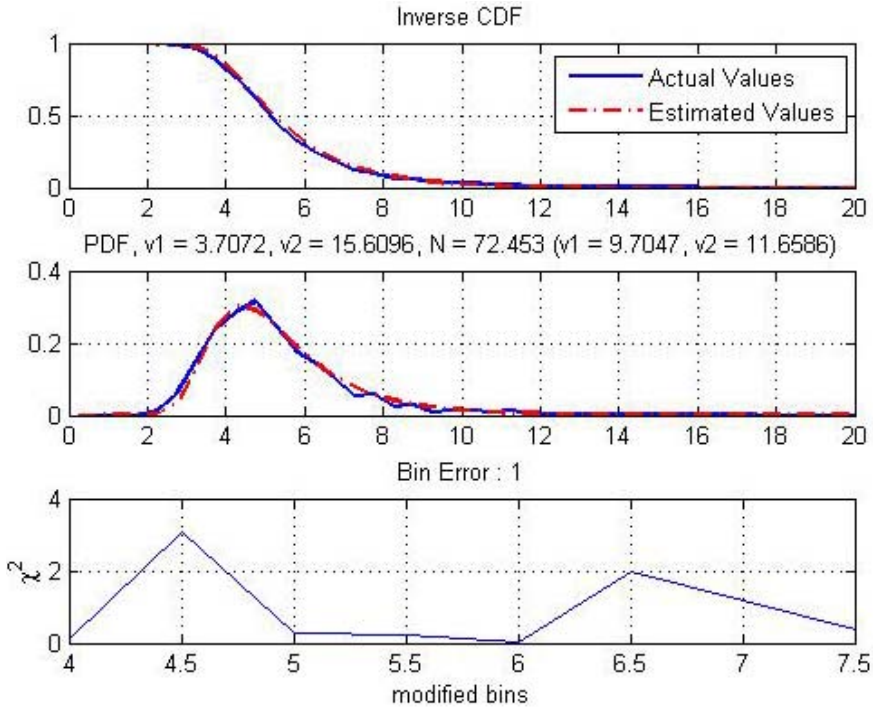

Figure 4.9. Distribution Fit for Dense Vegetation Background Segment

Table 4.2. Pass Percentages for Sparse Vegetation Background Segments

Sparse Vegetation Background Segments			
Band	**Pass Percentages (%) for 97% confidence level, RX**		
	Target Radius 0	**Target Radius 1**	**Target Radius 2**
NIR	83.75	85.00	90.00
RGB Colored	90.00	88.75	96.25
All 4 MSI Bands	81.00	95.00	97.50

Table 4.3. Pass Percentages for Dense Vegetation Background Segments

Dense Vegetation Background Segments			
Band	**Pass Percentages (%) for 97% confidence level, RX**		
	Target Radius 0	**Target Radius 1**	**Target Radius 2**
NIR	66.10	83.05	92.98
RGB Colored	81.36	100.00	96.61
All 4 MSI Bands	81.03	87.70	98.30

Table 4.4. Pass Percentages for Sparse Vegetation Minefield Segments

Sparse Vegetation Minefield Segments			
Band	**Pass Percentages (%) for 97% confidence level, RX**		
	Target Radius 0	**Target Radius 1**	**Target Radius 2**
NIR	80.00	96.00	98.00
RGB Colored	92.00	98.00	100.00
All 4 MSI Bands	90.00	94.00	98.00

Table 4.5. Pass Percentages for Dense Vegetation Minefield Segments

Dense Vegetation Minefield Segments			
Band	**Pass Percentages (%) for 97% confidence level, RX**		
	Target Radius 0	**Target Radius 1**	**Target Radius 2**
NIR	91.10	94.11	95.59
RGB Colored	92.60	98.00	98.53
All 4 MSI Bands	100.00	97.00	97.02

Table 4.6. Pass Percentages for Morning Time Background Segments

Morning Time Background Segments			
Band	**Pass Percentages (%) for 97% confidence level, RX**		
	Target Radius 0	**Target Radius 1**	**Target Radius 2**
NIR	65.00	77.50	90.00
RGB Colored	75.00	95.00	97.50
All 4 MSI Bands	70.00	92.50	97.44

Table 4.7. Pass Percentages for Afternoon Time Background Segments

Afternoon Time Background Segments			
Band	**Pass Percentages (%) for 97% confidence level, RX**		
	Target Radius 0	**Target Radius 1**	**Target Radius 2**
NIR	72.50	85.00	95.00
RGB Colored	75.00	95.00	97.50
All 4 MSI Bands	72.50	87.50	90.00

Table 4.8. Pass Percentages for Morning Time Minefield Segments

Morning Time Minefield Segments			
Band	**Pass Percentages (%) for 97% confidence level, RX**		
	Target Radius 0	**Target Radius 1**	**Target Radius 2**
NIR	75.56	100.00	100.00
RGB Colored	82.22	97.78	97.78
All 4 MSI Bands	75.56	95.46	95.56

Table 4.9. Pass Percentages for Afternoon Time Minefield Segments

Afternoon Time Minefield Segments			
Band	**Pass Percentages (%) for 97% confidence level, RX**		
	Target Radius 0	**Target Radius 1**	**Target Radius 2**
NIR	72.34	95.75	97.83
RGB Colored	87.23	97.87	97.87
All 4 MSI Bands	81.82	97.67	97.78

As shown from Tables 4.2 - 4.9, the pass percentages improve with an increase in the target radius. Moreover, as can be recalled from Section 4.3, at least 97% of the segments should pass the chi square test to expect good modeling. Modeling seems to be

poor for target radius of zero for most of the datasets. Reason for this behavior could be high propensity of single pixel outliers in the image data. However, in most of the practical applications, a target radius of 0 is not used so it can be ignored. However, as the target radius increases, the percentage of the segments passing the chi square test improves with some exceptions. For target radii of one and two, the pass percentages for most of the datasets is near 97% and hence modeling can be considered good. This is also expected because with higher target radius and hence lower effective resolution, the image is effectively independent Gaussian.

Table 4.10 shows the distribution of segments among different datasets in accordance with the confidence level. The total number of segments for each case of different target radii among all the datasets is also mentioned in brackets. As noted earlier, the confidence level is set to 0.97 and hence the segments are characterized accordingly into four major categories:

Category 1 (threshold < 0.95): This category represents those segments that easily passed the chi square test;

Category 2 (0.95 < threshold < 0.97): This category represents those segments that barely passed the chi square test;

Category 3 (0.97 < threshold < 0.99): This category represents those segments that barely failed the chi square test and;

Category 4 (threshold > 0.99): This category represents those segments that easily failed the chi square test.

Category 4 consists mainly of those segments that are highly non-homogeneous. Examples of these segments are shown in Figures 4.10 and 4.14, which represent the non-homogeneity of the background.

Also for a small target radius, the tail of the distribution is heavy compared with a larger target radius especially for the cases when most of the frames are dirt frames. This is demonstrated, in Figure 4.10 which displays the dirt only frame. Figure 4.11 shows both the actual as well as estimated PDF for the same FoR (NIR band only) with target radii of 0 and 2. It can also be seen that as the target radius increases, the heaviness of the tail decreases. However, for both the target radii, this segment passes the chi square test.

Table 4.10. Distribution of the Segments Modeled by Central F According to the Confidence Level

		NIR Band			RGB Band			All 4 MSI Bands		
Dataset Name	**Threshold Range**	**Target Radius = 0**	**Target Radius = 1**	**Target Radius = 2**	**Target Radius = 0**	**Target Radius = 1**	**Target Radius = 2**	**Target Radius = 0**	**Target Radius = 1**	**Target Radius = 2**
Dense Veg. Bkg. (59)	**< 0.95**	37(59)	48(59)	52(57)	47(59)	56(59)	55(59)	46(58)	48(57)	58(59)
	0.95 to 0.97	2	1	1	1	3	2	1	2	0
	0.97 to 0.99	5	3	1	4	0	1	3	3	1
	> 0.99	15	7	3	7	0	1	8	4	0
Dense Veg. MF. (68)	**< 0.95**	59(68)	63(68)	61(68)	63(68)	66(68)	67(68)	64(65)	64(67)	64(67)
	0.95 to 0.97	3	1	4	0	1	0	1	1	1
	0.97 to 0.99	2	1	1	4	1	1	0	1	1
	> 0.99	4	3	2	1	0	0	0	1	1
Sparse Veg. Bkg. (80)	**< 0.95**	64(80)	64(80)	71(80)	69(80)	68(80)	75(80)	59(80)	72(80)	76(80)
	0.95 to 0.97	3	4	1	3	3	2	7	4	2
	0.97 to 0.99	3	4	2	6	4	2	3	3	2
	> 0.99	10	8	6	2	5	1	11	1	0
Sparse Veg. MF. (50)	**< 0.95**	39(50)	47(50)	48(50)	44(50)	48(50)	47(50)	43(50)	46(50)	49(50)
	0.95 to 0.97	1	1	1	2	1	3	2	1	0
	0.97 to 0.99	5	1	0	3	0	0	1	2	0
	> 0.99	5	1	1	1	1	0	4	1	1
Morning Time Bkg. (40)	**< 0.95**	19(40)	31(40)	34(40)	31(40)	36(40)	39(40)	24(40)	37(40)	38(39)
	0.95 to 0.97	7	0	2	1	2	0	4	0	0
	0.97 to 0.99	4	2	2	2	2	0	5	0	0
	> 0.99	10	7	2	6	0	1	7	3	1
Morning Time MF. (45)	**< 0.95**	32(45)	40(45)	45(45)	33(45)	44(45)	43(45)	32(45)	42(45)	42(44)
	0.95 to 0.97	2	5	0	4	0	1	2	1	0
	0.97 to 0.99	4	0	0	2	0	1	3	0	1
	> 0.99	7	0	0	6	1	0	8	2	1
Afternoon Time Bkg. (40)	**< 0.95**	27(40)	34(40)	36(40)	28(40)	36(40)	39(40)	29(40)	31(40)	34(40)
	0.95 to 0.97	2	2	2	2	2	0	0	4	2
	0.97 to 0.99	2	3	0	2	1	0	7	0	1
	> 0.99	9	1	2	8	1	1	4	5	3
Afternoon Time MF. (47)	**< 0.95**	31(47)	44(47)	45(46)	41(47)	45(47)	46(47)	35(44)	40(43)	40(45)
	0.95 to 0.97	2	1	0	0	1	0	1	2	4
	0.97 to 0.99	4	0	0	2	1	1	1	0	0
	> 0.99	10	2	1	4	0	0	7	1	1

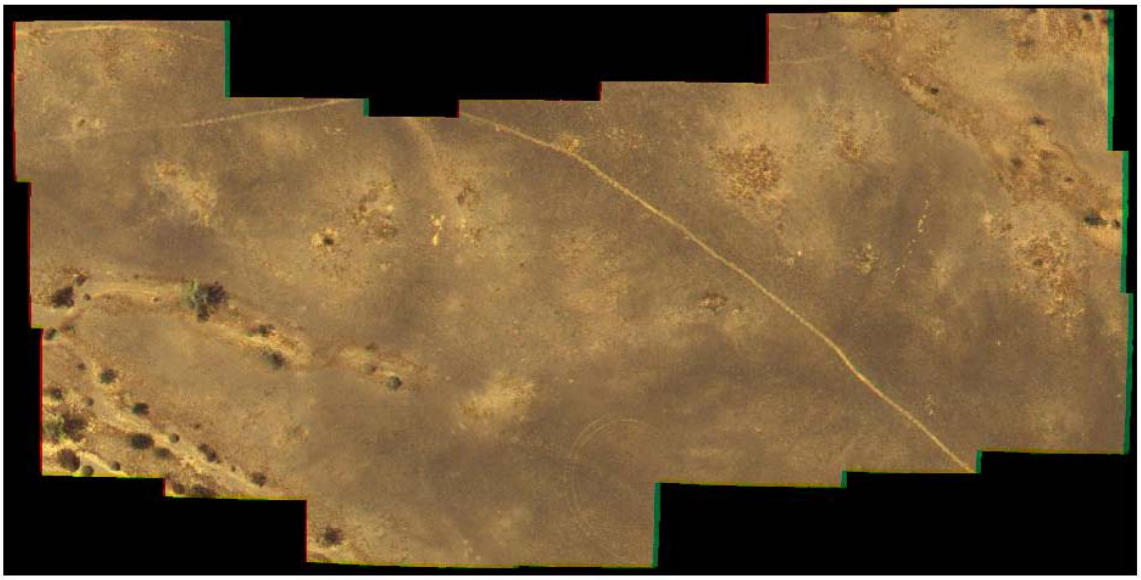

Figure 4.10. Sparse Vegetation Background Segment Predominantly Dirt

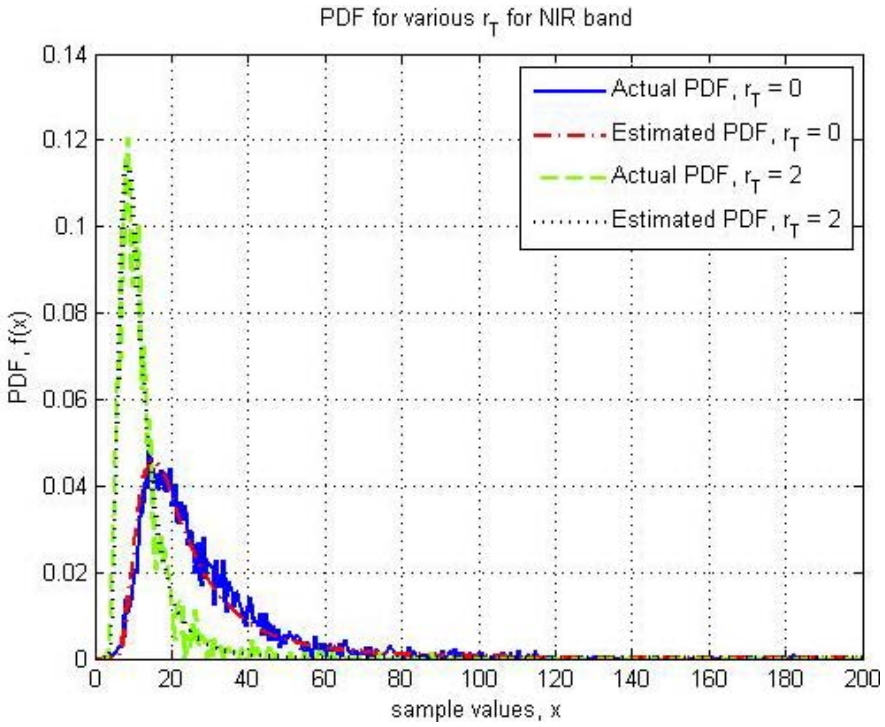

Figure 4.11. Actual and Estimated PDF for the NIR Band for Target Radii Zero and Two

Another interesting case is for the segment, which consists of various backgrounds. For these mixtures of backgrounds, the EM algorithm fails to provide an

accurate fit for the F distribution in accordance with the chi square test. An example for this mixture of backgrounds is shown in the Figures 4.12 and 4.14. Figure 4.12 shows the sparse vegetation segment with two different backgrounds. As shown from the segment, some of the frames (Frames 13 – 21) represent a bright path (encircled in broken cyan) in contrast to other non-bright frames (Frames 1 – 12). For this bright background, the EM algorithm fails to find an accurate fit. However, for the rest of the frames (non-bright), the distribution passes the chi square test. This is common behavior for these types of background mixtures in which a whole segment is punished due to a non-homogeneous background. Figure 4.13 shows the actual and estimated PDF and inverse CDF for bright and non bright background. Figure 4.13(a) shows the actual and estimated PDF, and Figure 4.13(b) shows the corresponding inverse CDF.

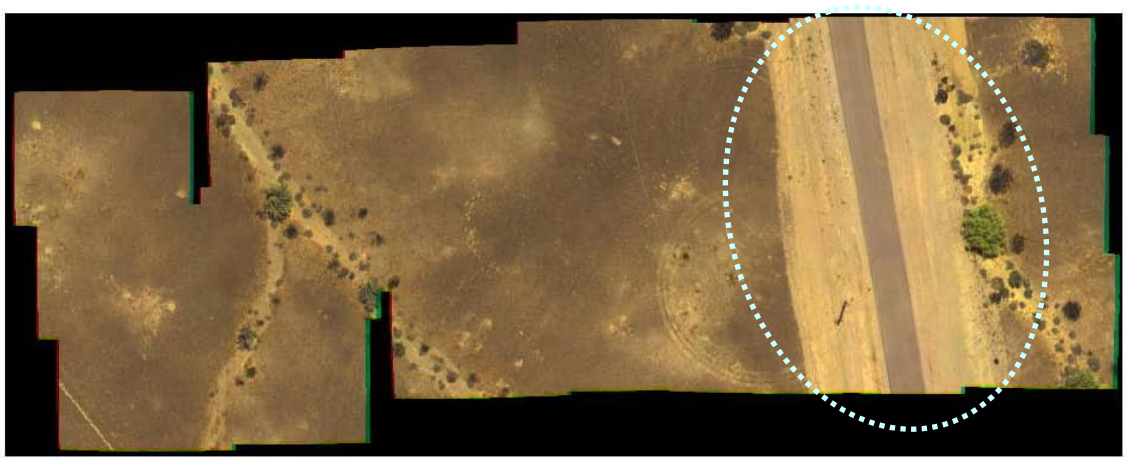

Figure 4.12. Segment Showing the Non-Homogeneous Dirt Background

It is worthwhile to note that EM modeling fails for the bright area, whereas it passes for the rest of the segment. This is also visible from Figure 4.13 (b) in which the actual inverse CDF (blue) and estimated inverse CDF (broken red) are quite off, which results in failure. Also, the actual PDF for the bright area (solid blue) is noisier than the actual PDF for the rest of the segment (broken green).

The presence of different and non-homogeneous backgrounds is one of the main reasons for the failure in distribution fit. In this case, the background is either dirt or

dense vegetation. If the segment is bifurcated on the basis of the background, i.e., if the frames for the dirt and vegetation from the same segment are separated and then passed separately for the modeling then it is evident that for the vegetative frames, the fit passes the chi square test but fails for the dirt frames. Also, the tail for the dirt RX samples is heavier than for the vegetative RX samples. A segment with two different backgrounds (dirt and dense vegetation) is shown in Figure 4.14. Figure 4.15 shows the actual and estimated PDF and inverse CDF for two backgrounds. Figure 4.15(a) shows the actual and estimated PDF, and Figure 4.15(b) shows the corresponding inverse CDF.

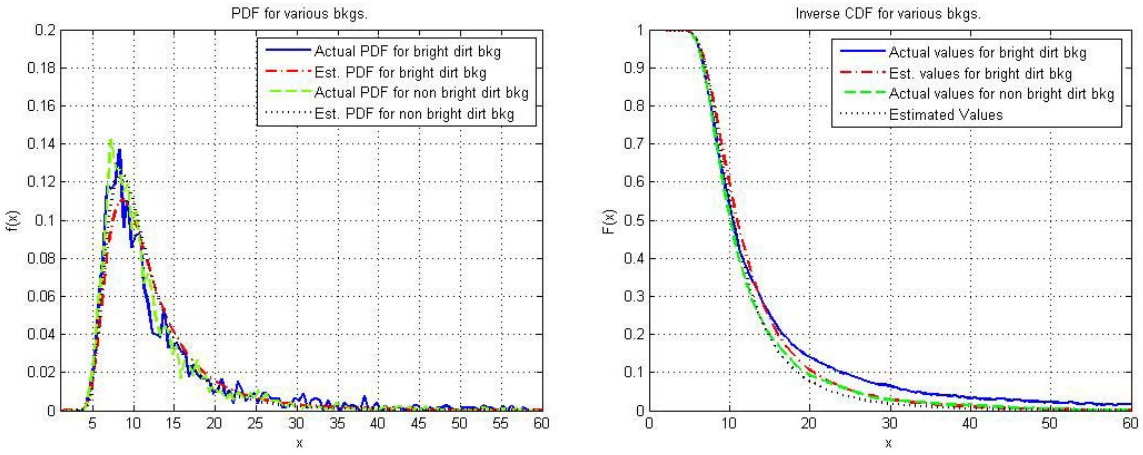

(a) Actual and Estimated PDF (b) Actual and Estimated Inverse CDF

Figure 4.13. Actual and Estimated PDF and Inverse CDF for Bright and Non-Bright Background

As evident from Figure 4.15, for both backgrounds the sample RX values are very different. For vegetation, the actual and estimated PDF are very much on top of each other and hence pass the chi square test; however, for a dirt background, the RX values are quite different and noisier. Also, in contrast to the vegetation frames, the dirt PDF shows a heavy tail. Moreover, for the dirt, the actual and inverse PDF does not have a good fit, which causes the dirt background RX values to fail the chi square test. The difference between the two backgrounds is also visible in the inverse CDFs.

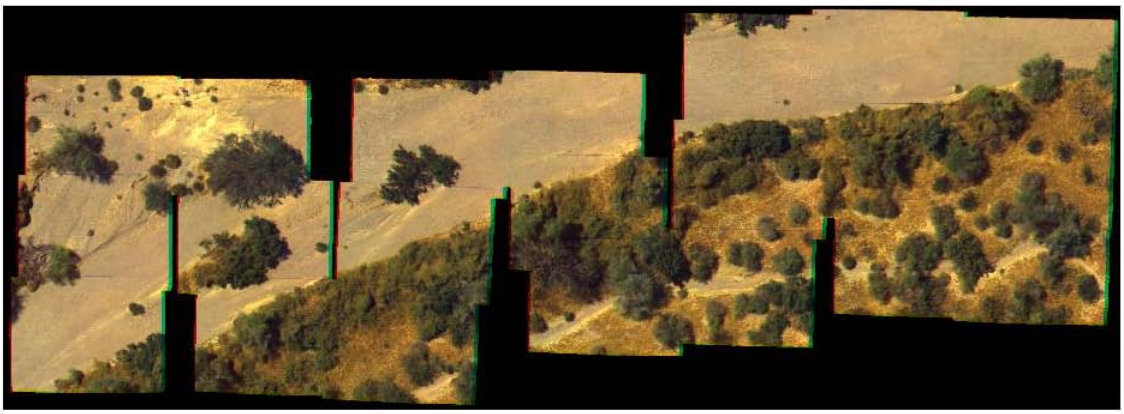

Figure 4.14. Segment Showing Different (Dirt and Vegetation) Background

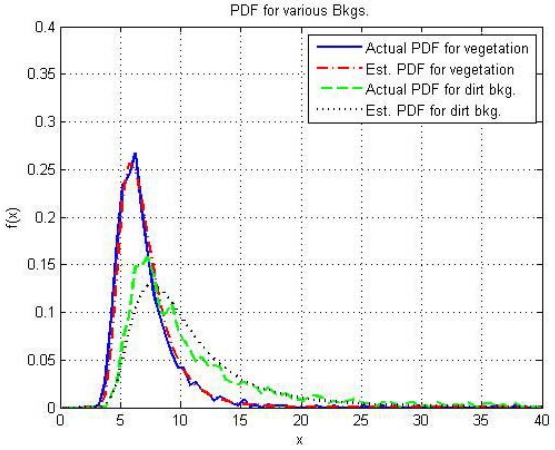

(a) Actual and Estimated PDF

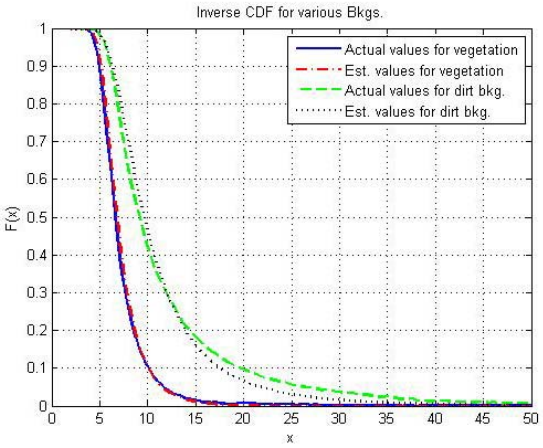

(b) Actual and Estimated Inverse CDF

Figure 4.15. Actual and Estimated PDF and Inverse CDF for Dirt and Dense Vegetation Background

4.5. OTHER ANOMALY DETECTION TECHNIQUES

The RX anomaly detector is one of the most popular techniques used for anomaly detection. Some derivatives of the RX detector such as the normalized RX detector and modified RX detector are also available [Chang and Chiang, 2002]. Number of other anomaly detection algorithms have been proposed and used depending on the situation and other factors. Some of these are unmixing component analysis [Yanfeng et al., 2006], kernel principal component analysis [Gu et al., 2006], cluster-based anomaly detection [Carlotto, 2005], signal subspace processing [Ranney, 2006], support vector data

description [Banerjee et al., 2006], and anomaly detection based on multi resolution features [Shadhan and Cohen, 2006].

False alarm mitigation (FAM) techniques are other general techniques that can be used for anomaly detection. In general, FAM aims to reduce false alarms based on the shape, photometric, polarity, spectral, and other properties of the mine targets to reject likely false alarms. FAM techniques are dependent on a number of factors such as the time of day, size and nature of the mine target, nature of the terrain, and nature of the local background of the target. Moreover, FAM techniques exploit the characteristics of likely mine signatures to reduce false alarms. Thus, FAM serve the dual purpose of providing a measure of mine level detection performance as well as other features that can be used to understand the nature of mine targets and false alarms [Menon et al., 2004]. Circularity, radial symmetry, and gray scale moments are some of the false alarm techniques that can be used as false alarm mitigation techniques. Detailed description of these techniques can be found in [Menon et al., 2004].

Spectral vegetation indices can also be used to detect the presence of live green vegetation and hence for false alarm mitigation. These indices are generated by combining data from multiple spectral bands into a single value. More about these indices is discussed in Appendix A.

5. SPATIAL DISTRIBUTION

This section discusses the spatial distribution of the targets obtained after the anomaly detection. The spatial characteristics (physical locations) of these RX detections can be studied and a spatial distribution can be modeled to fit the spatial location of potential mine detections. Once the modeling for the spatial distribution is successful, the model can be incorporated into simulation.

5.1. SPATIAL POINT PROCESSES

A collection of points each representing the location of an event in space can be termed the spatial point process [Møller and Waagepetersen, 2006]. Mathematically, the spatial point process is defined in the following manner [Cressie, 1991].

Let $\mathbf{s} \in R^d$ be a generic data location in a *d*-dimensional Euclidean space, and suppose the potential datum **Z(s)** at spatial location **s** is a random variable. Now let **s** vary over index set $D \subset R^d$, then the generated multivariate random field or random process

$$\{\mathbf{Z(s)} : \mathbf{s} \in D\} \tag{5.1}$$

is termed the random point process. Realization of such a process is called the spatial point pattern [Møller and Waagepetersen, 2006], **z** of *n* points such that,

$$\mathbf{z} = \{z_1, z_2, ..., z_n\}, n \geq 0 \text{ points contained in } D \tag{5.2}$$

For the current discussion, the point processes are limited to 2D space domains (R^2). If the datum **Z(s)** represent only the location of point, it is called 'simple' point process and if it contains some other markings like color, it is called 'marked' point process. Important inferences about the spatial occurrences of events can be drawn from the simple point process **Z(s)**, where each point in such a random process represents the location of some event. A large variety of events are possible, however, for the purpose of the current discussion, the event is the occurrence of landmines or a false alarm.

Spatial point patterns play a vital role in a wide variety of scientific and engineering problems such as ecology, telecommunication, forestry, biostatistics, geology, and economics. These patterns have also found applications in fields as diverse as archeology, cosmology, and seismology. However, the application of spatial point processes in the field of minefield detection is different from many other applications in a way that for minefield detection, the spatial locations are a mixture of different processes (the presence of a minefield and presence of false alarm/clutter). Also the exact identity of the process associated with each event is unknown. In some cases it's advantageous to model such process using the framework of marked point process [Trang et al., 2007]. The current discussion is however limited to simple point processes.

Spatial patterns can be broadly classified as three distinct spatial distributions: random, aggregated, and regular [Kummamuru, 2002; Reich, 2007] as described next.

5.1.1. Random Point Process. A point pattern is said to be random if the presence and absence of any other location does not affect the relative location of any point. In other words, each point's location is independent of the location of any other point. Checking the spatial randomness of the spatial point process is often the first step in the analysis of spatial point processes. Reliable approach should be used to quantify the randomness because for some observers, random processes can also appear to be clustered. Scale is very important and should be clearly indicated because purely random processes may appear clustered at a larger scale.

5.1.2. Aggregated Point Process. This is the most common type of point processes in real world. As the name indicates, in the aggregated point process, the points occur in lumps of different densities. In this case, the location of any point is not independent of the location of other points but instead the occurrence of one point actually favors the occurrence of other points in its neighborhood resulting in the cluster formation.

5.1.3. Regular Point Process. Point processes in which the points are evenly distributed over a given area approximately forming vertices of regular shapes such as lines, rectangles, squares and triangles are called regular point patterns. In case of regular point process, occurrence of one point disfavors the occurrence of another point in its neighborhood. Both aggregation and regular point processes are the extreme cases for

random point processes. An example resulting in a regular point process is shown by walnut trees [Reich, 2007]. The roots and leaves of a walnut tree produce toxic substances that inhibit the growth of other trees within the immediate vicinity resulting in a regular or uniform spatial pattern. In case of minefield, patterned minefield form an approximate regular point process.

5.2. COMPLETE SPATIAL RANDOMNESS

Complete Spatial Randomness (CSR) is the standard against which spatial point patterns are often compared. The hypothesis of CSR for a spatial point pattern asserts that [Diggle, 2003]:

1. Number of events in any planar region *A* follows a Poisson distribution with mean $\lambda |A|$ where |*A*| is the area of *A* and λ is the intensity that does not vary over the region, and,
2. Events are equally likely to occur anywhere within area *A* and no interactions occur between the events either repulsively (regular point process) or attractively (aggregated point process).

This process has the property that, conditional on $N(A)$, the number of events in a bounded region $A \subset R^d$, the events of the process are independently and uniformly distributed over *A,* i.e., given $N(A)$ = n, the ordered *n* tuple of events $(s_1,...,s_n)$ in A^n satisfies the following identity [Cressie,1991]

$$\Pr(s_1 \in B_1,...,s_n \in B_n) = \prod_{i=1}^{n} (|B_i| / |A|), \qquad B_1,...,B_n \subset A, \tag{5.3}$$

Figure 5.1 shows the CSR process with the total area of the region under study, |*A*| = 1000X1000 m^2, and λ = 0.001/m^2.

5.3. MEASURES OF COMPLETE SPATIAL RANDOMNESS

Various approaches have been used to quantify various types of spatial point patterns against the CSR process. The most common methods are the quadrat method and

distance method. The quadrat method is based on sampling of the area under consideration using small regions called quadrats. A number of statistics have been proposed in the literature based on these quadrat methods. The second type of measures is based on a set of distance measurements made from an event to its k^{th} nearest neighbor or from a randomly selected sample point to its k^{th} nearest neighbor.

5.3.1. Quadrat Measures. This method is one of the very first to be proposed to measure the spatial randomness in point processes. It involves collecting counts of the number of events in subsets of the study region *A*. Traditionally these subsets are rectangular, although any shape is possible. Quadrats may be placed either randomly or laid out contiguously in *A*. The number of events in each quadrat is collected, and these numbers are tabulated as a frequency distribution and are called quadrat counts. Several types of statistics are applied on these quadrat counts to calculate the test statistics. A detailed description and implementation of these statistics based on quadrat measure has been investigated in [Kummamuru, 2002] and more details can be found in [Cressie, 1991].

For a CSR process shown in Figure 5.1, square quadrat (A_i) of size 100x100 m^2 are selected. Now, for each subset A_i (100X100m^2 square) of study region *A*, the number of events is collected. For the CSR process, these events should be samples from Poisson distribution with mean $\lambda |A_i|$ (= 10 in this case) where $|A_i|$ is the area of subset A_i. Figure 5.2 shows the distribution of the number of events in each quadrat (quadrat counts) and corresponding theoretical (Poisson) distribution with mean $\lambda |A_i|$. As shown in Figure 5.2, the two distributions are in complete agreement.

5.3.2. Nearest Neighbor Distance Measures. In these methods, event to event or point to event distances are computed and summarized. Distances can be calculated between events and nearest neighboring events or between sample points and nearest events. Sample points are placed in the study area randomly or systematically. These distances are used as test statistics, and various statistical models are being used to simulate the event to event nearest neighbor distances.

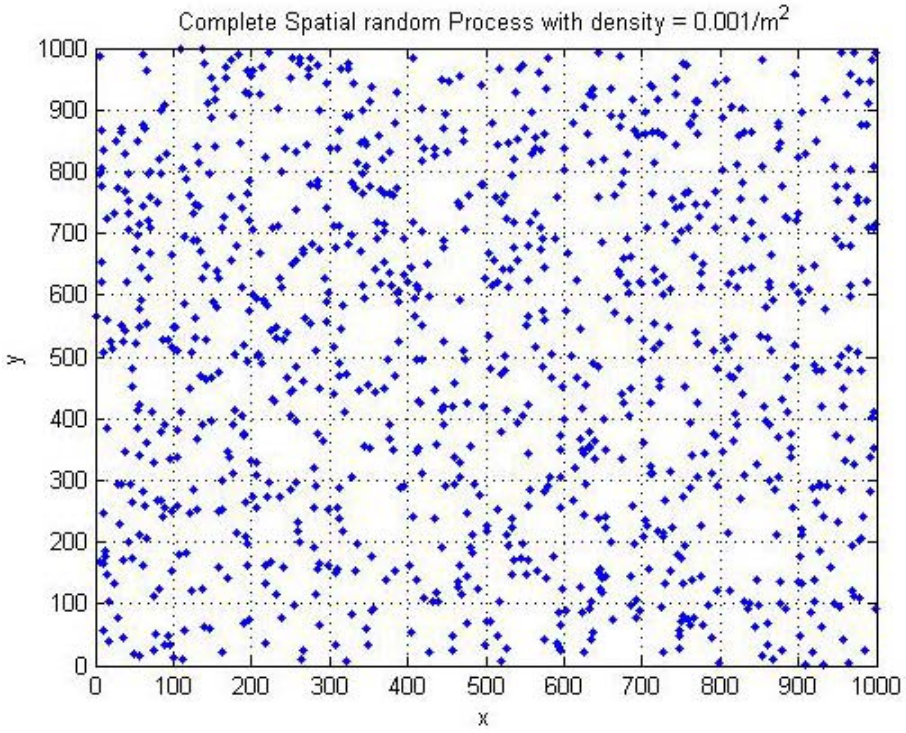

Figure 5.1. Complete Spatial Random Process with Density = 0.001/m^2

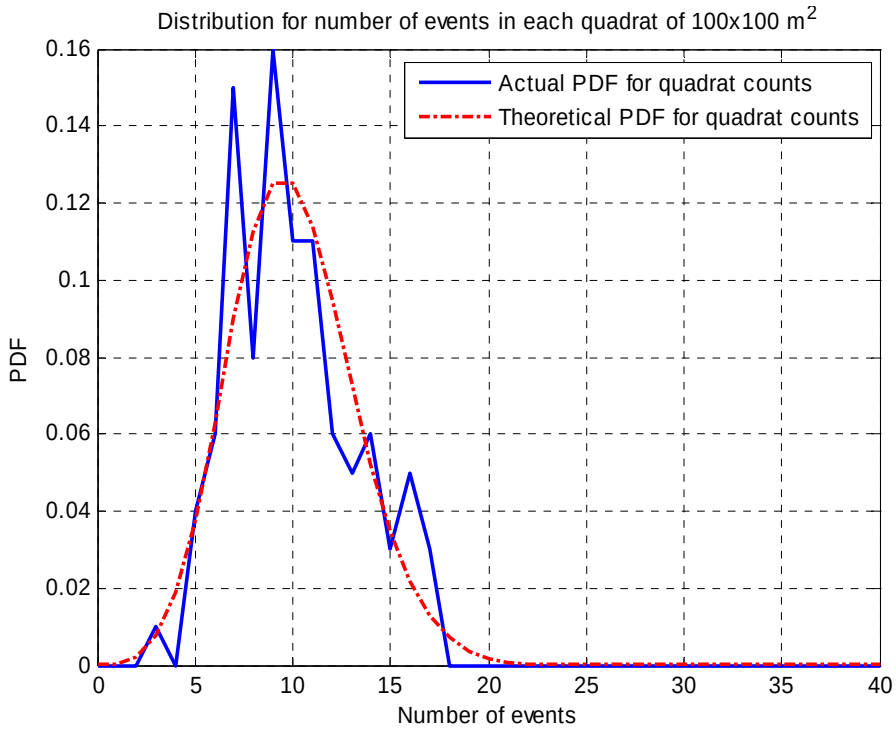

Figure 5.2. Distribution of the Quadrat Counts

For the CSR process, the distribution for event to event nearest neighbor statistics can be derived as below [Corcoran, 2004]. Let λ be the mean number of points per unit area and let D be the distance between an event and its nearest neighbor, and let x be the radius of a circle around the event. The probability that the nearest neighbor of the event lies in the circle of radius x is given by

$$P(D \le x) = 1 - P(D > x) \tag{5.4}$$

Because the process is CSR, the probability of finding no point within radius x (> 0) is given by

$$P(D > x) = e^{-\lambda\pi x^2} \lambda^0 / 0! = e^{-\lambda\pi x^2} \tag{5.5}$$

Thus Equation (5.4) reduces to

$$F_D(x) = P(D \le x) = 1 - e^{-\lambda\pi x^2} \tag{5.6}$$

where $F_D(x)$ is the cumulative distribution function for the nearest neighbor.

Thus, the probability distribution function for the nearest neighbor can be found by differentiating equation (5.5) with respect to *x;* i.e.,

$$f_D(x) = \frac{d}{dx} F_D(x) = \frac{d}{dx}(1 - e^{-\lambda\pi x^2}) = 2\lambda\pi x e^{-\lambda\pi x^2}, \; x > 0 \tag{5.7}$$

Equation (5.7) represents the probability density function for the nearest neighbor distance *x*. The above derivation can be extended for the k^{th} nearest neighbor also. The PDF for the k^{th} nearest- neighbor distance x_k is given as [Cressie, 1991]

$$f_D(x_k) = 2(\lambda\pi)^k x_k^{2k-1} e^{-\lambda\pi x_k^2} / (k-1)!, \qquad x_k > 0 \tag{5.8}$$

where x_k is the k^{th} nearest neighbor distance form an arbitrary event.

Figure 5.3 shows the actual PDF (blue) and theoretical (Equation (5.7)) PDF (broken red) for first nearest neighbor distances for the CSR process shown in Figure 5.1. As shown in Figure 5.3, there is good agreement between the actual and theoretical PDF. For an aggregated process, the actual PDF will be shifted toward the left side because in that case, the nearest neighbor distances will be less as compared to nearest neighbor distances for a CSR point process whose example is shown in Figure 5.1. Also the distribution is shifted toward the right for a regular point process.

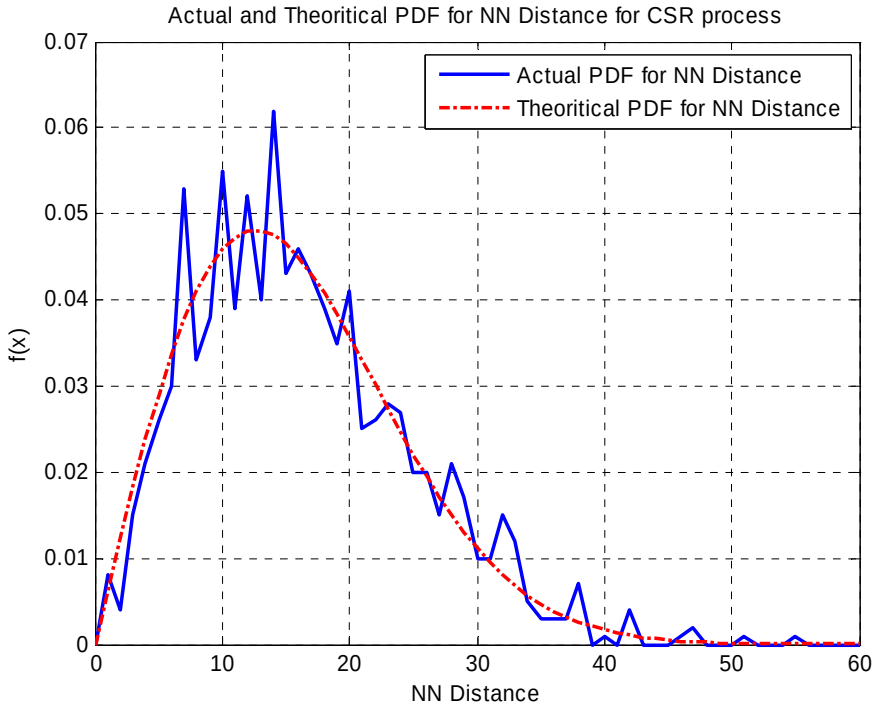

Figure 5.3. Actual and Theoretical PDF for the First NN Distances for CSR Process

5.4. SPATIAL DISTRIBUTION OF MINES AND FALSE ALARMS

This section discusses the nearest neighbor distances for the actual scattered and patterned minefields and false alarms. Corresponding theoretical PDF for these are also drawn and comparisons between actual and theoretical PDF are made.

Figure 5.4 shows the distribution of mines and corresponding nearest neighbor distances PDF for the scattered minefield for probability of detection of 100% and 50%. Figure 5.4(a) shows the distribution of mines in a typical scattered minefield scenario

with density (0.0127mine/m^2) displayed in the title. Figure 5.4(b) shows the comparison between the actual and theoretical (based on CSR assumption) PDF for the nearest neighbor distance (NN Distance) for the same case. Figure 5.4(c) shows the comparison between the actual and theoretical (based on CSR assumption) PDF for the NN distance when only 50% of mines are randomly selected. The actual and theoretical PDF shows good agreement for both the cases, which would suggest that the above scattered minefield can be modeled as CSR process and random detection does not affect the spatial characteristics of nearest neighbor distances for the minefield.

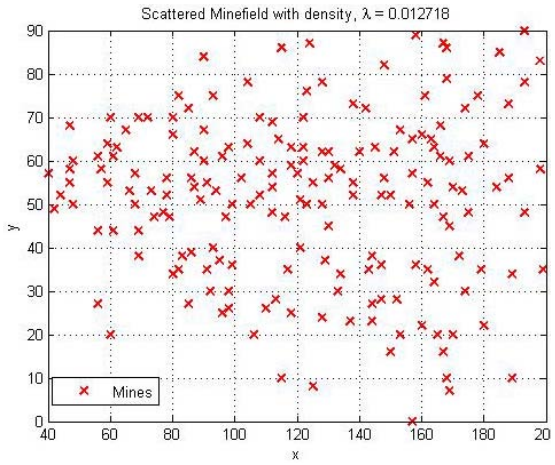

(a) CSR process – Scattered Minefield

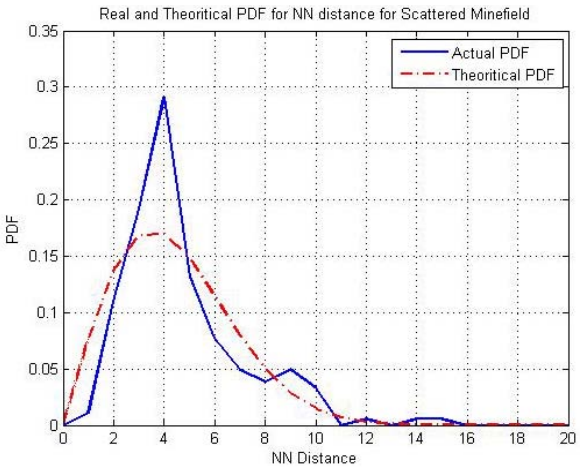

(b) Actual and Theoretical PDF for first nearest neighbor distances

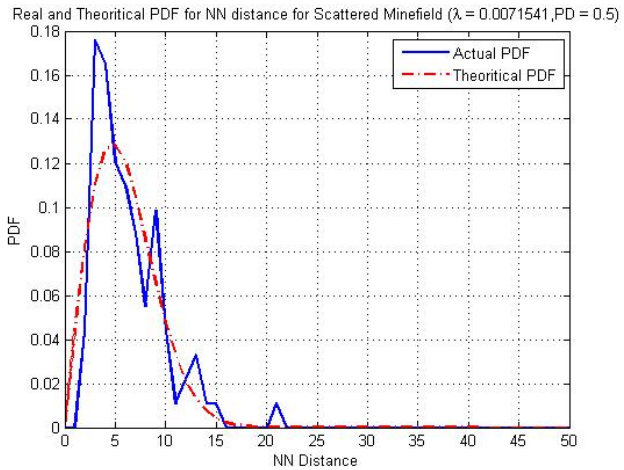

(c) Actual and Theoretical PDF for first nearest neighbor for PD = 0.5

Figure 5.4. CSR Scattered Minefield and Corresponding NN Distribution

For patterned minefield, the nearest neighbor distance is fairly constant with small variation due to placement which can be modeled as a Gaussian distribution. The distribution of nearest neighbor distances (x) can be defined as:

$$f_D(x) = \frac{1}{\sqrt{2\pi\sigma_S^2}} e^{-\frac{(x-S)^2}{2\sigma_S^2}} \tag{5.9}$$

where S is the separation between mines in a row and σ_S^2 is the variance in this separation.

For the random detection of mines with probability of detection, p_d, the distribution of nearest neighbor distances can be derived as:

$$f_D(x \mid p_d) = \sum_{k=1}^{\infty} (1-(1-p_d)^2)(1-p_d)^{2(k-1)} \frac{1}{\sqrt{2\pi\sigma_S^2}} e^{-\frac{(x-kS)^2}{2\sigma_S^2}} \tag{5.10}$$

Figure 5.5 shows the distribution of mines and corresponding nearest neighbor PDF for the patterned minefield for PD of 100% and 50%. Figure 5.5(a) shows the distribution of mines in a typical patterned minefield scenario. Figure 5.5(b) shows the comparison between the measured PDF, theoretical PDF (based on Equation 5.10) and one based on CSR assumption for the nearest neighbor distance (NN Distance) for the case of 100% detection. Figure 5.5(c) shows the comparison between the measured PDF, theoretical PDF and one based on CSR assumption for the NN distance for the probability of mine detection of 50%.

As shown in Figures 5.5(b) and 5.5(c), the actual PDF is regular since the nearest neighbor distances has a prominent peak at the separation distance (4m) for 100% detection of mines. Moreover, for random detection of 50% of mines, the peaks in the PDF are likely to occur at integer multiple of the separation between mines, which is shown in the Figure 5.5(c).

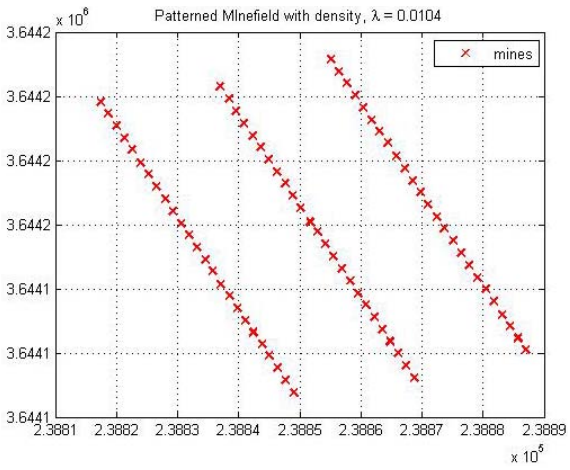

(a) Patterned Minefield

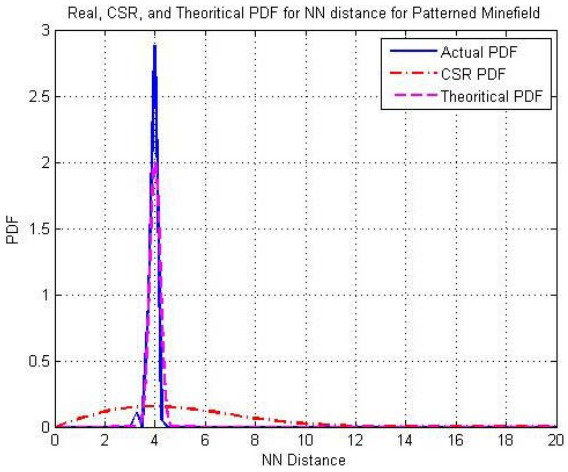

(b) Actual and Theoretical PDF for first nearest neighbor distances

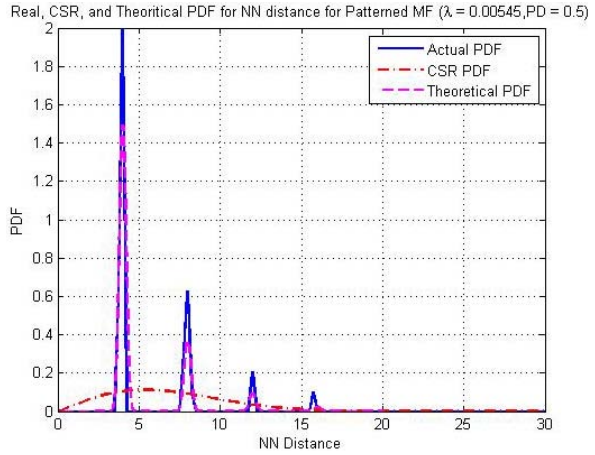

(c) Actual and Theoretical PDF for first nearest neighbor for PD = 0.5

Figure 5.5. Patterned Minefield and Corresponding NN Distribution

Figure 5.6 shows the location of false alarms detected by RX algorithm in one background segment. As is evident from the figure, the false alarms are not distributed randomly but, form clusters (enclosed in broken yellow).

Figure 5.7 shows the distribution of NN distances based on 15 background segments. Blue curve shows the distribution of NN distances for actual false alarms and red curve shows the distribution for Poisson CSR process with the same false alarm rate drawn using Equation (5.7). The false alarm density is equal to 0.01 FA/ m^2.

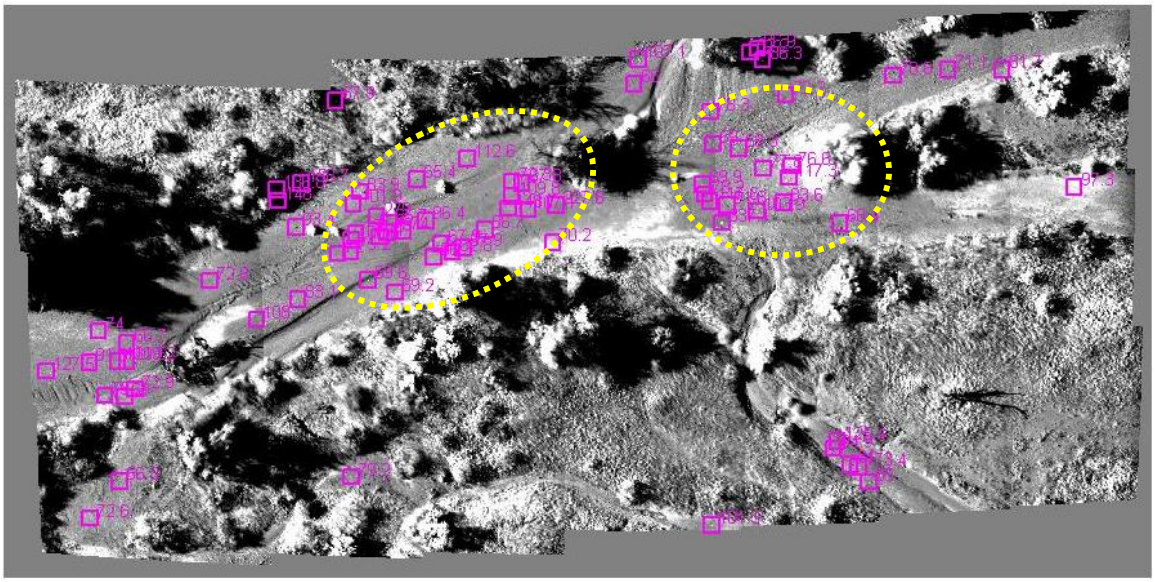

Figure 5.6. Location of False Alarms in a Background Segment

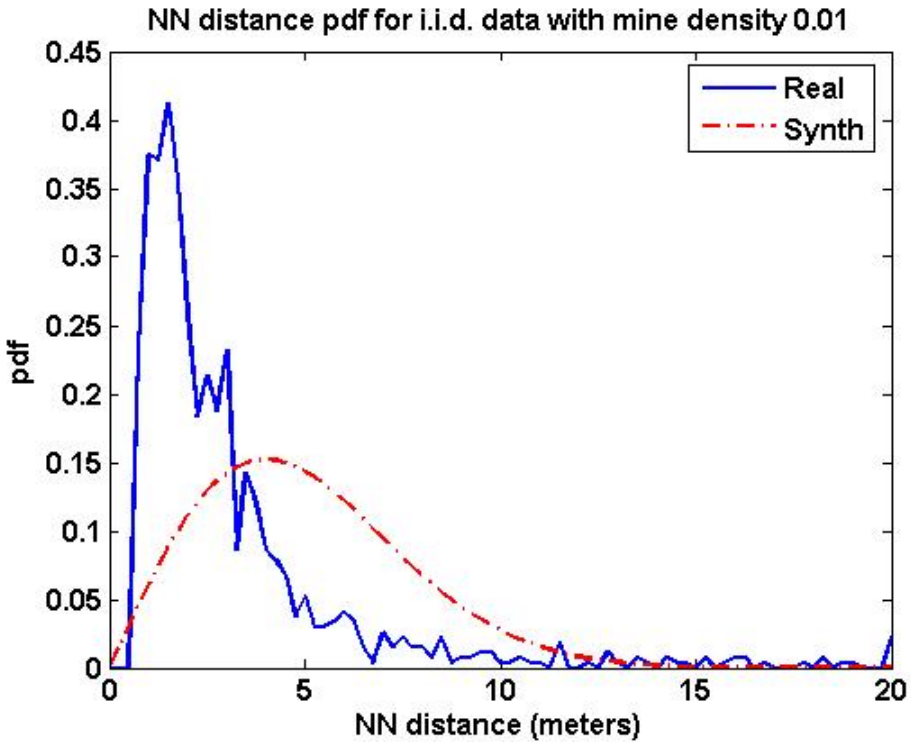

Figure 5.7. Actual and Theoretical Distribution for NN Distances for False Alarms

As shown from Figure 5.7, unlike the NN distances for scattered minefield, the NN distances for the false alarm are not distributed corresponding to CSR process. The false alarms are clustered as shown in Figure 5.6. This can also be interpreted from the Figure 5.7, as the PDF for NN distances for actual false alarms is also biased toward left indicating more false alarms in comparatively small vicinity, like an aggregated process. Thus it becomes necessary to study other spatial distributions to model the spatial locations for the false alarms. This aspect is however not be addressed in this thesis and is left for future work.

6. MINEFIELD DETECTION AND ANALYTICAL MODELS

Once the mine level detection is complete, the next step is to detect the presence of minefields using the information from the mine level results. Minefield detection is dependent on the thresholded mine level detection statistics derived in the previous section. The target locations identified after the non-max suppression and mine level thresholding for each FoR are used for detecting the minefield and eventually evaluating the minefield level confidence metric. Various minefield level detection algorithms are applied on the anomaly detections to derive a metric that provides confidence level for the presence or absence of minefields in that area. As discussed in Section 3, minefield can be either scattered or patterned depending on the position of mines in the minefield and the tactical scenarios. A number of minefield detection schemes are available in literature to detect the presence of patterned or scattered minefields. Discussions on some of these algorithms are presented in this section. This section also explains the analytical and statistical models that are developed and used to estimate the performance for the minefield detection. Separate analytical models are developed for both patterned and scattered minefield for validation.

6.1. PATTERNED MINEFIELD

This section discusses the detection algorithm and analytical model for patterned minefield.

6.1.1. Detection Algorithm. Pattern linear algorithm is one of the algorithm that is used for evaluating the minefield level confidence values for the patterned minefield in which mines are arranged in rows. This algorithm uses the Hough line detector [Carlson et al**.,** 1994] to detect the presence of mines in a linear fashion. The Hough line detector is a powerful and extensive feature detection method well suited for the detection of lines in the presence of noise. It is used to evaluate the maximum number of targets that fall on a line. Hough transform projects each point on a higher dimension parametric space of lines given by:

$$P = x\cos\theta + y\sin\theta, \theta \in (-\pi/2, \pi/2), P \in (-L, L) \qquad (6.1)$$

where P represents the length of normal from the origin and θ is the orientation of P with respect to the X axis. Figure 6.1 shows an example for the Hough transform. Figure 6.1(a) shows the five points in the spatial domain. Hough parameter space corresponding to five points on the line is also shown in Figure 6.1(b).

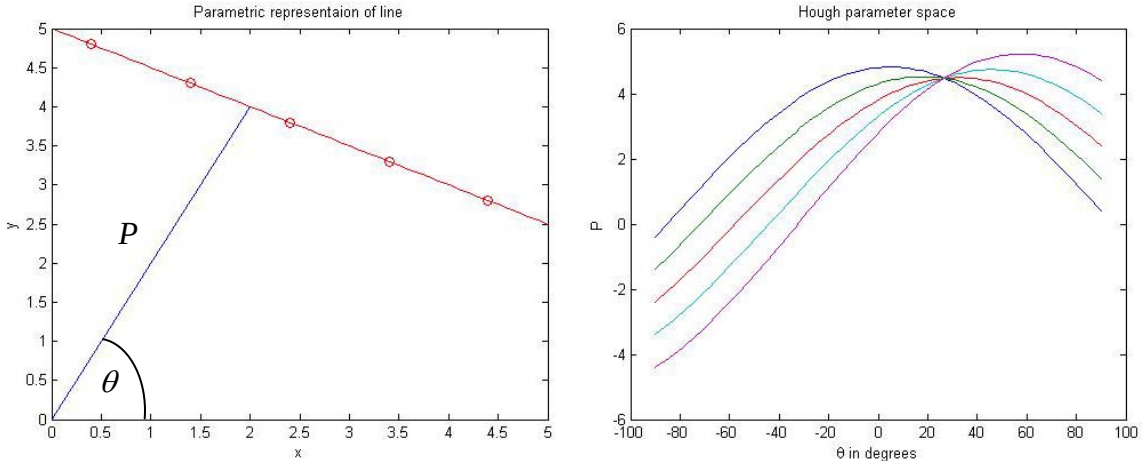

(a) Five data points in spatial domain and a line through them

(b) Hough parameter space showing five sinusoids corresponding to 5 data points

Figure 6.1. Hough Transform Pair Representing the Data Points in Spatial Domain and Corresponding Sinusoids in the Hough Parameter Space

It can be shown that Equation. 6.1 is equivalent to

$$P = \sqrt{x^2 + y^2}\,\sin\left(\theta + \tan^{-1}\frac{x}{y}\right) \tag{6.2}$$

Thus, mapping in this Hough parameter space ($[P,\theta]$) results in a sinusoid with an amplitude and phase dependent on the spatial coordinates (x, y) of the point, i.e., each point in the (x, y) space corresponds to a single sinusoid in the Hough parameter space. Therefore, the set $[P,\theta]$ that satisfies the above equation represents all lines that can pass through line 'P.' These values of P and θ are then collected into a number of bins called *accumulators* depending on the number of sectors in which a segment area is

divided. The number of points in each bin represents the number of points that are collinear on the line present at a distance of P from the origin and angle θ. The accumulator bins can be further evaluated to identify targets on parallel lines by summing targets along the same θ index to accumulate targets.

Another algorithm which can be used is pattern regular. This algorithm is the same as the pattern linear with an exception that it enforces regularity between the targets falling on a line [Lake et al**.,** 1997; Malloy, 2003]. Thus, two detections that are too close together or too far apart are neglected.

6.1.2. Analytical Model. Analytical model for linear pattern for patterned minefield detection algorithm is described next which is applicable for pattern linear detection algorithm. The analytical approach is based on the theoretical estimation of minefield detection performance under certain assumptions**.** Patterned minefields have mines arranged in some specific pattern, often linear. These can be in the form of a number of rows with some predefined spacing between the rows and between individual mines in each row. Let R denote the number of rows of mines in the patterned minefield with M mines in each row. The detection of mines is assumed to be binomial so that if p_d is the probability of the detection of mines, then the probability of detection of n mines in a row is given by

$$P[n \text{ mines} \mid M] = \frac{M!}{n!(M-n)!} {p_d}^n (1-p_d)^{M-n} \tag{6.3}$$

The false alarm detection is assumed to be Poisson with density ρ_B. Thus, when the minefield is not present, the probability of detection in an interrogation area of size A_S is given by

$$P[k \mid \text{Background only}] = \frac{(\rho_B A_S)^k}{k!} e^{-\rho_B A_S} \tag{6.4}$$

The size of the interrogation area A_S depends on the linearity of the minefield. In a linear minefield, this area can be a thin strip. When a minefield is present, the total

detections is given by the sum of mines and false alarms. Thus the probability of the detection of k targets in area A_S when a minefield is present is given by:

$$P[k \mid \text{Minefield}] = \sum_{\lambda=0}^{k} P(\lambda \text{ mine} \mid M).P(k-\lambda \mid \text{Background only}) \qquad (6.5)$$

In a FoR with area A, there are $Q = \text{round}\left[A / A_S\right]$ independent measurements from an interrogation area of size A_S. Similarly for R rows of mines in the FoR, there are R independent measurements for mine statistics. The final minefield confidence can be taken as the maximum of these independent measurements in the FoR. The probability of detection $P_d(k)$ and the probability of false alarm $P_{fa}(k)$ at any threshold k in this case is given by

$$P_d(k) = 1 - \left(1 - \sum_{\lambda=0}^{k} P(\lambda \mid \text{Minefield})\right)^R \qquad (6.6)$$

$$P_{fa}(k) = 1 - \left(1 - \sum_{\lambda=0}^{k} P(\lambda \mid \text{Background only})\right)^Q \qquad (6.7)$$

The false alarm rate at threshold '*k*' can be written as

$$FAR(k) = P_{fa}(k)\frac{10^6}{A} \text{ FA/km}^2 \qquad (6.8)$$

$P_d(k)$ and $FAR(k)$ in Equation (6.6) and (6.7) can be used to draw the ROC curve for analytical performance.

Figure 6.2 shows an analytical ROC curve for patterned minefield with three rows of mines and different distance between mines. Distance of 4m, 5m and 6m is used between mines. For a minefield FAR of 0.5 FA/km^2, corresponding PD are 0.95, 0.72 and 0.57 for case of 4m, 5m, and 6m of separation, respectively. As can be seen from the

figure, minefield performance improves as the separation between mines decreases. This is expected since the number of mines in the minefield increases as the separation between mines is reduced.

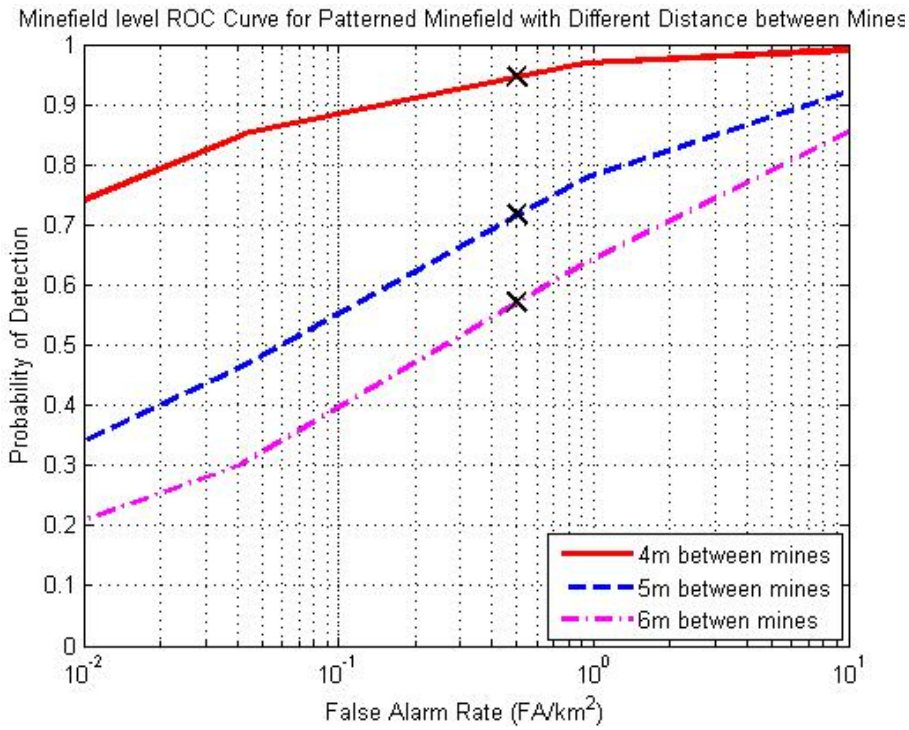

Figure 6.2. Analytical ROC Curve for Patterned Minefield with Different Distance between Mines

Alternatively, R rows of detection (mines) can be scored in which case probability of the detection of mines and of false alarms is given by

$$P_R[n \text{ mine} \mid \text{Minefield}] = \begin{bmatrix} RM \\ n \end{bmatrix} (p_d)^n (1-p_d)^{(RM-n)} \tag{6.9}$$

$$P_R[k \mid \text{Background only}] = \frac{(\rho_B RA_S)^k}{k!} e^{-\rho_B RA_S} \tag{6.10}$$

The probability of detection $P_d(k)$ and the probability of false alarm $P_{fa}(k)$ at any threshold k is given by

$$P_d(k) = \sum_{\lambda=0}^{k} P_R(\lambda \mid \text{Minefield}) \tag{6.11}$$

$$P_{fa}(k) = 1 - \left(1 - \sum_{\lambda=0}^{k} P_R(\lambda \mid \text{Background only})\right)^{(S/R)} \tag{6.12}$$

FAR(k) can be obtained as defined in Equation (6.8) and $P_d(k)$ and *FAR(k)* can be used to draw the analytical ROC curves.

Figure 6.3 shows an analytical ROC curve for patterned minefield with different number of rows in the minefield. Distance between the mines is kept constant and is equal to 5m. For a minefield FAR of 0.5 FA/km^2, corresponding PD of 0.35, 0.85 and 0.98 is obtained for 1, 2, and 3 rows of mine. The minefield performance improves significantly as the number of rows is increased. This is expected since more number of rows of mines in a minefield increases the number of mines available for minefield detection.

6.2. SCATTERED MINEFIELD

Various minefield level detection algorithms and analytical model for scattered minefield are discussed below.

6.2.1. Detection Algorithm. Scatter number is the basic algorithm for evaluating the minefield confidence value for each FoR for a scattered minefield. In this algorithm, the number of detections from the interrogation patch is taken as the confidence value for the minefield. Thus, confidence value λ_{SN} for a FoR is given as

$$\lambda_{SN} = N\{D\} \tag{6.13}$$

where $N\{D\}$ represent the number of detections obtained from the FoR. The statistics are applicable to the CFAR type of thresholding scheme for target detection.

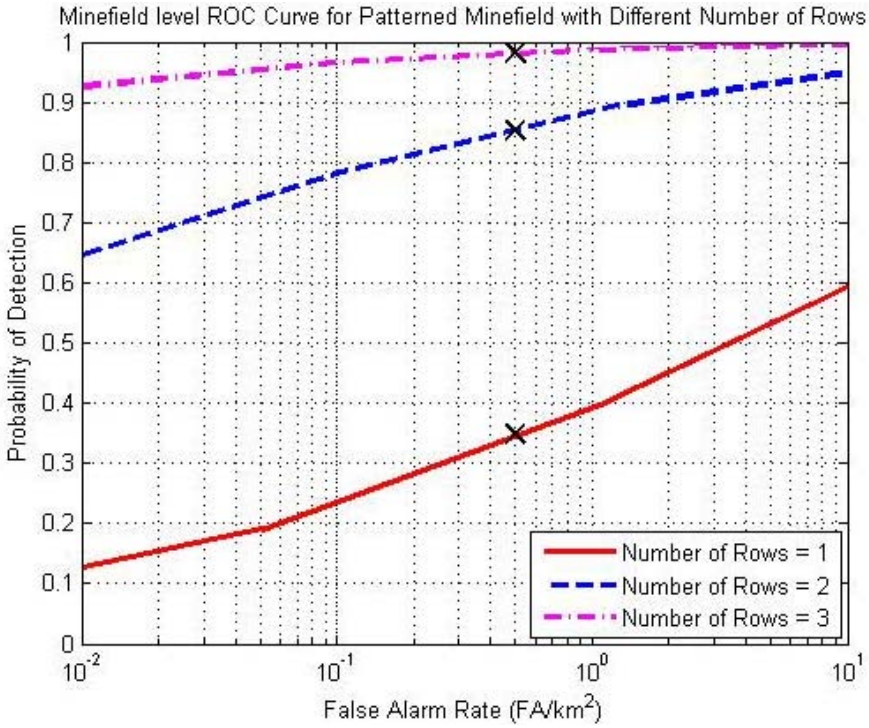

Figure 6.3. Analytical ROC Curve for Patterned Minefield with Different Number of Rows of Mine

The test statistics in Equation (6.13) can be shown to be optimal when both the mines and false alarms follow a CSR distribution and no other information is available to differentiate mines from the false alarms [Earp, 2000b]. This detection scheme is quite popular and used due to quick analysis of scattered minefield.

Scattered log weighted is another algorithm which is similar to the scattered number except that the decision statistics are defined as the average of the log of the detection statistics for all valid detection as proposed by Earp [Earp et al., 1995]. A minefield test statistics obtained based on likelihood ratio is defined as:

$$\Lambda_{\text{minefield}} = \frac{1}{N}\sum_{k=1}^{N} Ll(x_k) \tag{6.14}$$

where $Ll(x)$ is the log-likelihood ratio for the AD values of x_i and N is the number of targets in the FoR.

Using empirical result Earp [Earp, 1995] proposed a log function in place of $Ll(x)$ so that the test statistics is defined as:

$$\Lambda_{\text{minefield}} = \frac{1}{N}\sum_{k=1}^{N}\log(x_k) \tag{6.15}$$

This statistics is applicable to constant target rate (CTR) as well as to constant false alarm rate (CFAR) type target detection. This value represents the minefield confidence value for that segment.

6.2.2. Analytical Model. For a scattered minefield, it is assumed that the mines are laid randomly over an area. Because the deployment of mines within the minefield is random, a suitable model for the distribution can be assumed to be a "completely random" Poisson point process [Earp, 2000a and 2000b]. In this case, the probability of encountering a mine in an area is independent of the probability of encountering a mine in any other area. The false detections are also assumed to be Poisson with a different intensity parameter ρ_B. The probability of getting k false alarm detections from the background in an area A of the FoR can be modeled as

$$P[k \mid \text{Background only}] = \frac{(\rho_B A)^k}{k!}e^{-\rho_B A} \tag{6.16}$$

Let ρ_T be the density of mines (in mines per unit area) in the minefield and p_d be the rate of detections. Then the probability of getting k mine detections in an area A is given by

$$P[k \mid \text{MineField}] = \frac{(p_d \rho_T A + \rho_B A)^k}{k!}e^{-p_d \rho_T A + \rho_B A} \tag{6.17}$$

representing Poisson detection of both the mines and false alarms.

The probability of detection $P_d(k)$, probability of false alarm $P_{fa}(k)$, and FAR at any threshold *k* is given by

$$P_d(k) = \sum_{\gamma=k}^{\infty} P[\gamma \mid \text{MineField}] = 1 - e^{-(p_d \rho_T A + \rho_B A)} \sum_{\gamma=0}^{k-1} \frac{(p_d \rho_T A + \rho_B A)^{\gamma}}{\gamma!} \tag{6.18}$$

$$P_{fa}(k) = \sum_{\gamma=k}^{\infty} P[\gamma \mid \text{Background only}] = 1 - e^{-\rho_B A} \sum_{\gamma=0}^{k-1} \frac{(\rho_B A)^{\gamma}}{\gamma!} \tag{6.19}$$

$$FAR\ (k) = P_{fa}(k) \frac{10^6}{A} \text{ FA/km}^2 \tag{6.20}$$

$P_d(k)$ and *FAR (k)* can be used to draw the analytical ROC curves. Note that an implicit assumption in the model is that the size of FoR is smaller than the minefield and that the FoR is fully over the minefield. Figure 6.4 shows an analytical ROC curve for scattered minefield with different mine densities.

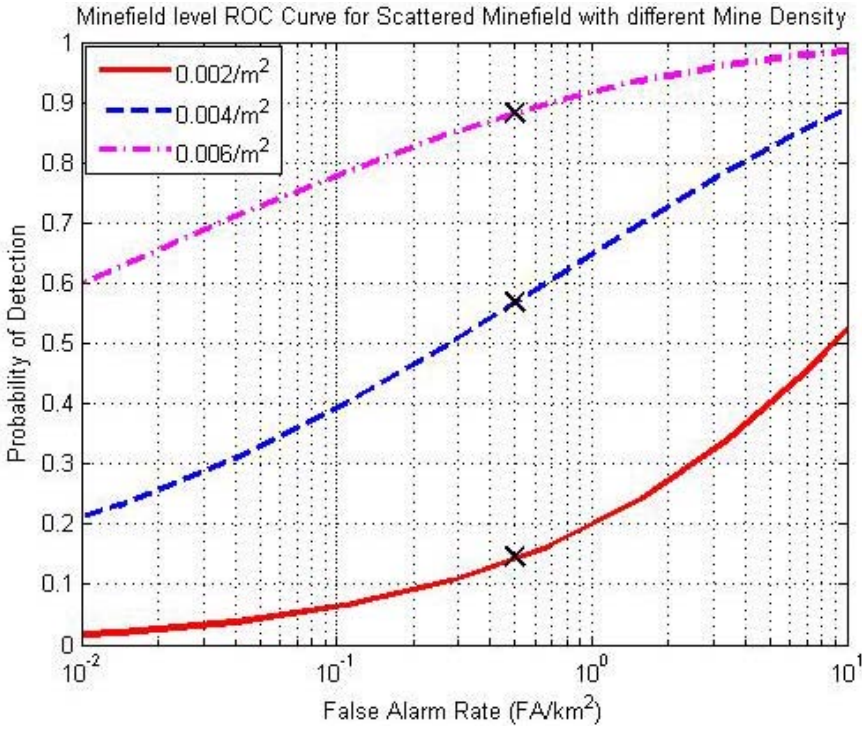

Figure 6.4. Analytical ROC Curve for Scattered Minefield with Different Mine Density

Mine level PD at the FAR of 0.001 FA/m^2 is 0.34. Mine density of 0.002 mines/m^2, 0.004 mines/m^2 and 0.006 mines/m^2 are used. Minefield level PD values of 0.145, 0.567 and 0.882 are obtained corresponding to false alarm rate of 0.5 FA/km^2. PD and FAR are calculated using Equation 6.18 and 6.20, respectively. The minefield performance improves as the mine density increases.

7. SIMULATION RESULTS

This section presents mine and minefield detection results for the simulated parameters. Several variables are used for generating the simulated data, which are tabulated in Table 7.1. Results are generated for both patterned and scattered minefields with different parameters. Parameters whose effects are considered include signal to clutter ratio (SCR), constant false alarm rate (CFAR), swath width, holidays, and segment overlap. Each of these parameters is discussed in the following subsections.

Table 7.1. Simulation Parameters for Scattered and Patterned Minefield Data

	Scattered	**Patterned**	
No. of runs simulated	750	750	
Flight Speed	75	75	knot
Altitude	2050	2050	feet
No. of rows, columns	512, 640	512, 640	pixel
No. of swath, steps	7, variable (1-5)	7, variable (1-5)	
Swath width, FoR length	60 – 290	60 – 290	feet
FoR length	451– 455	451– 455	feet
Bkg. Anomaly distribution	Central F- distribution ($J = 4$, $N_c = 50$)	Central F- distribution ($J = 4$, $N_c = 50$)	
Bkg. spatial distribution	Poisson with density of $0.01/m^2$	Poisson with density of $0.01/m^2$	
Mine Anomaly distribution	Non Central F-distribution ($J = 4$, $N_c = 50$, SCR = 0.5)	Non Central F- distribution ($J = 4$, $N_c = 50$, SCR = 0.125)	
Mine spatial distribution	Poisson with density of $0.004/m^2$	Linear (distance of 9 meters between mines. Three rows with distance of 20m between rows)	
Mine type	SM_A (Small metal)	LM_A_B (Large metal Buried)	
Mine size (No. of Pixels)	6 (13)	12 (50)	inch
Mine level algorithm	CFAR with FAR of 0.001	CFAR with FAR of 0.001	FA/m^2
Minefield Algorithm	Scatter Number	Pattern Linear	

7.1. EFFECT OF SCR

The SCR for the RX detection is defined as in Equation (3.6)

$$SCR = \frac{\bar{\mu}^2}{\sigma^2} = \sum_{i=1}^{J} \mu_i^2 \Big/ J\sigma^2 \tag{7.1}$$

where $\bar{\mu}$ is the mean target signature, and σ is the standard deviation of the background area. Figure 7.1 shows the mine level and corresponding minefield level ROC curves for different SCR values. Figure 7.1(a) shows the mine level ROC curve for a scatterable minefield and Figure 7.1(b) shows the corresponding minefield level ROC curves for SCR values of 0.4 (red), 0.5 (blue), and 0.6 (green) for the scatterable minefield with three steps (swath width of 175 feet). The corresponding GSNR values are 20.8, 26 and 31.2, respectively.

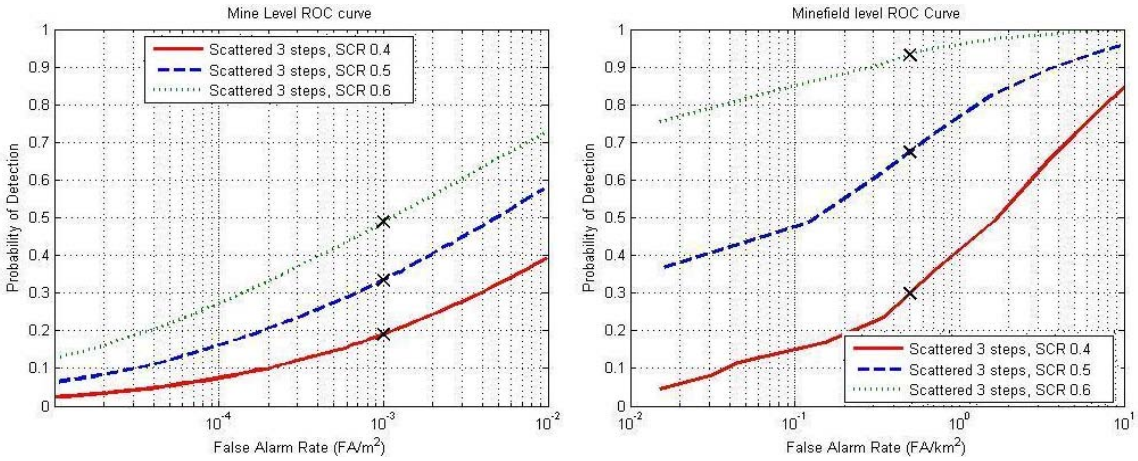

(a) Mine level ROC curve (b) Minefield level ROC curve

Figure 7.1. Mine Level ROC Curve and Corresponding Minefield Level ROC Curve for Different SCR Values

As shown from Figure 7.1, the mine level as well as minefield level performance increase with an increase in the SCR value. This is expected because with an increase in the SCR values, contrast difference between the mine targets and background clutter

increases, which facilitates the detection of mines. The same performance is expected for the patterned minefield. The minelevel PDs for the SCR values at the FAR of 0.001FA/m^2 are 0.19, 0.34, and 0.49, respectively, as indicated by the 'x' mark in Figure 7.1(a). Similarly, minefield PDs at an FAR of 0.5 FA/km^2 are 0.30, 0.68, and 0.93, respectively.

7.2. EFFECT OF CFAR VALUE

In this type of mine level thresholding, the false alarm rate per square meter (ρ_B) is specified. At any selected value of ρ_B , the expected number of false alarms in FoR is constant. Figure 7.2 shows the effect of the CFAR value on the minefield level performance. CFAR values of 0.00005 (red), 0.001 (blue), 0.004 (magenta), and 0.008 (black) are used with scattered minefields with three steps. As shown from Figure 7.2(b), as the FAR value increases, the respective minefield performance decreases. This is because the density of mines is very small as compared with the density of background anomalies (0.004/m^2 of mines in contrast with 0.01/m^2 of background anomalies). As CFAR value increases, the number of detected mines in FoR also increases due to increase in PD. However, the increase is lower as compared to the increase in false alarm.

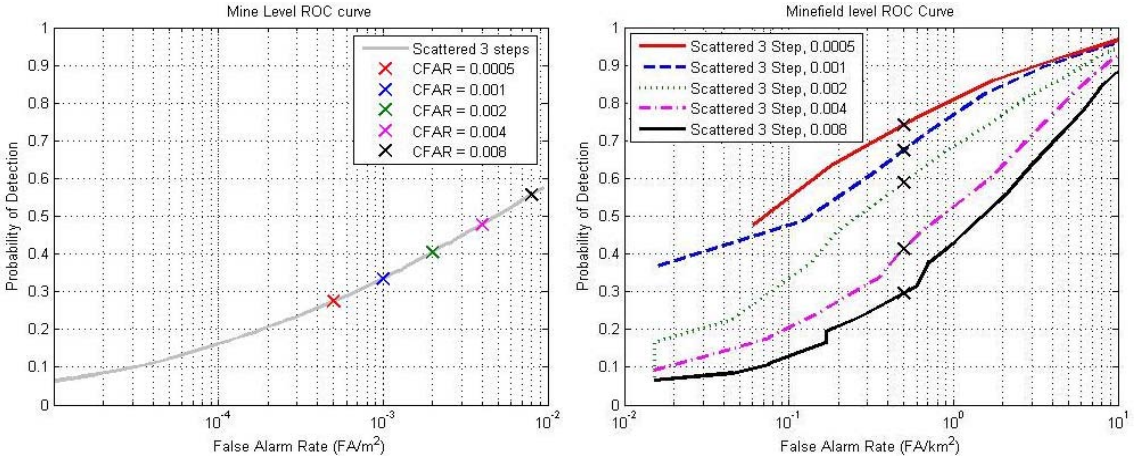

(a) Mine level ROC curve (b) Minefield level ROC curve

Figure 7.2. Mine Level ROC Curve and Corresponding Minefield Level ROC Curve for Different FAR Values for Scattarable Minefield

7.3. EFFECT OF SWATH WIDTH

Figures 7.3 and 7.4 show the simulation results for a swath width of 1 and 5 (steps) for patterned and scattered minefields, respectively. Magenta squares and red diamonds represent the mines in respective figures. All of the segments are represented by different color fills.

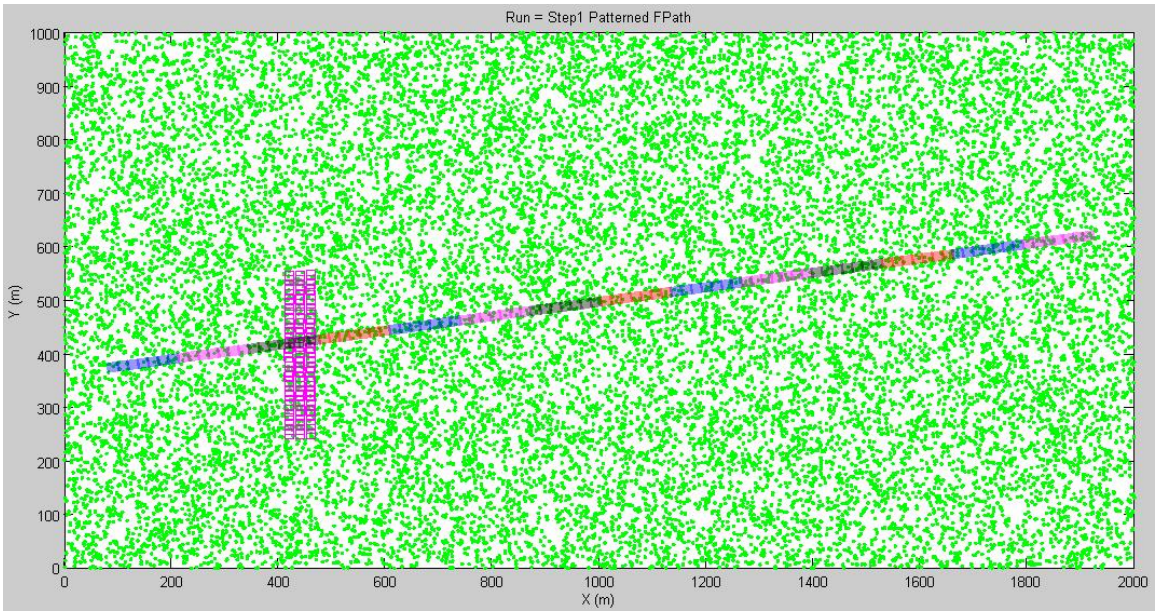

Figure 7.3 Simulated Minefield Layout for a Patterned Minefield with Swath Width of One Step

Figure 7.5 shows the effect of the swath width on the minefield level performance for a patterned minefield with three rows of mine and 20% side step overlap, and Figure 7.6 shows the effect on a scattered minefield. The number of steps of 1 (red), 2 (blue), 3 (green), 4 (magenta), and 5 (black) corresponding to a swath width of 63 ft, 119 ft, 175 ft, 232 ft, and 288 ft, respectively, are used for the results. The mine level FAR is chosen to be 0.001 FA/m^2 for both the scattered and patterned minefields resulting in a corresponding PD of 0.33 for the scattered minefield and 0.51 for the patterned minefield.

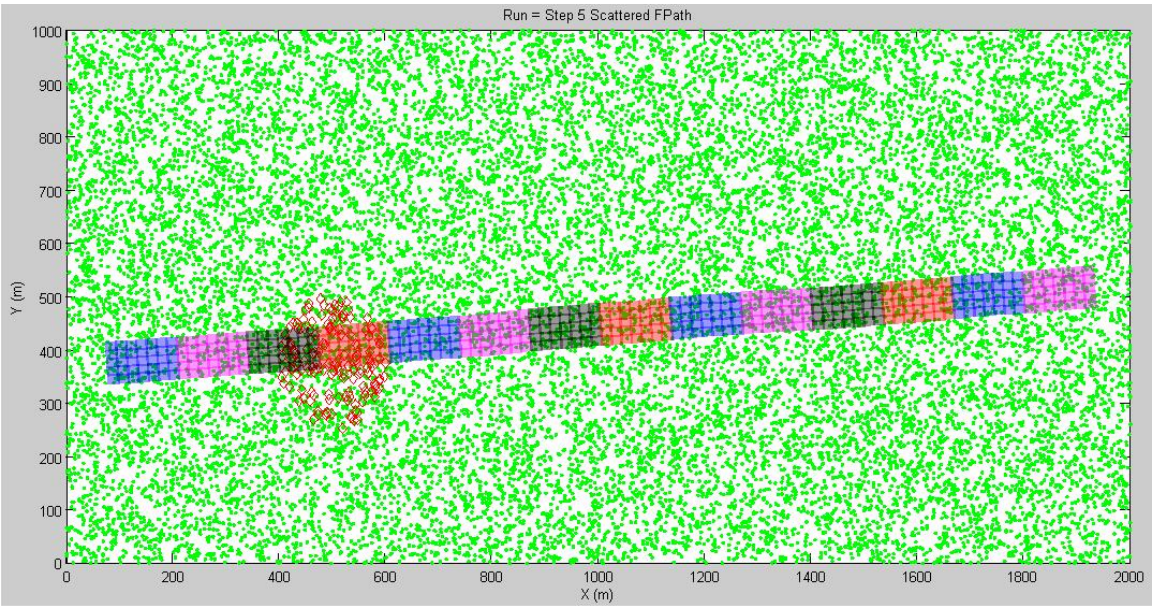

Figure 7.4. Simulated Minefield Layout for a Scattered Minefield with Swath Width of Five Steps

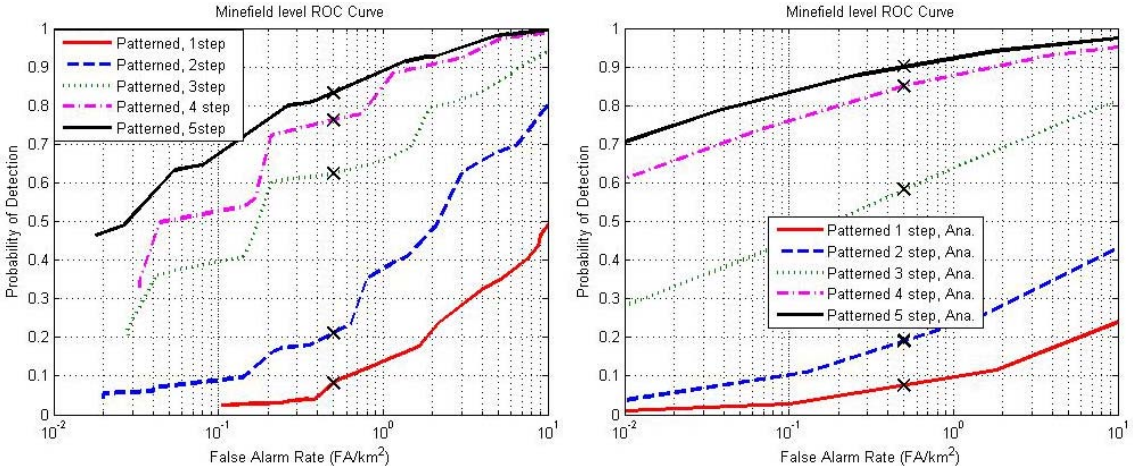

(a) Simulated minefield performance (b) Analytical minefield performance

Figure 7.5. Simulated and Analytical Minefield Level ROC Curves for the Patterned Minefield for Different Swath Widths

As shown from Figures 7.5 and 7.6, a good agreement exists between the simulated and analytical results. Also, for both the scattered and patterned minefields, performance increases with an increasing swath width. This is expected as the minefield

front is wider than the maximum swath width of 288 feet (88 meters). A bigger swath width results in more mine targets in the FoR, which results in more reliable detections. However, increasing the swath width beyond the size of the minefield front may actually result in lower detections. This may happen for smaller tactical scattered minefields.

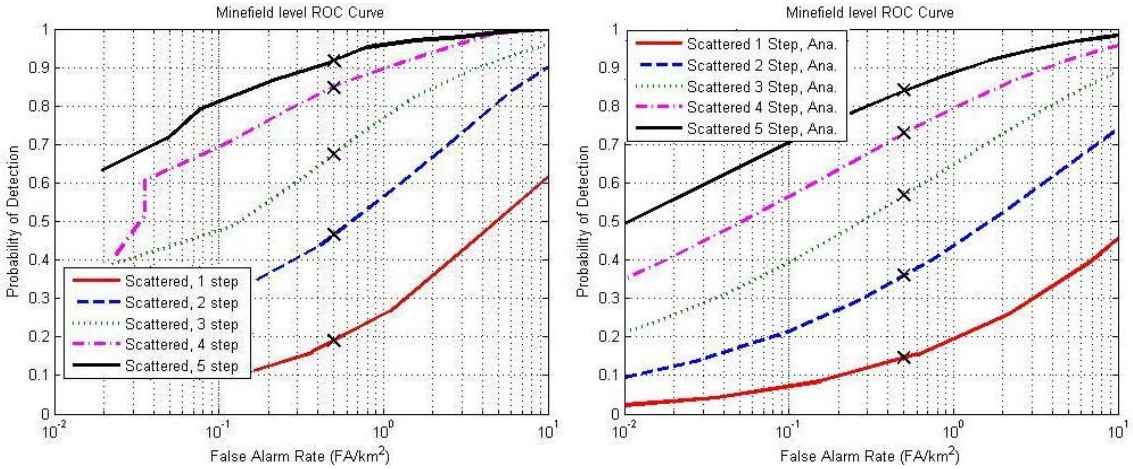

(a) Simulated minefield performance (b) Analytical minefield performance

Figure 7.6. Mine Level ROC Curve and Corresponding Minefield Level ROC Curve for Scattered Minefields with Different Swath Widths

7.4. EFFECT OF HOLIDAYS

Data are collected in the form of frames of images. These frames are then stitched together to form an FoR/segment. This transformation of image frames in a single coordinate system is called image registration and plays a significant role in the mine and minefield level performance evaluation. However, for accurate image registration, it is necessary for some portions of the consecutive frames to overlap in order to provide the control points for the frame to frame registration. Sufficient overlap should be present in both the in-flight and across-flight direction to obtain an accurate and undistorted mosaic of frames. If the overlap among frames is insufficient, then holidays will exist between the frames. Figures 7.7 and 7.8 show the simulation results for the side-step overlap for -20% (holiday) and 20% respectively. As seen from Figure 7.7, a negative side-step overlap is quite visible resulting in the absence of control points in the in-flight direction.

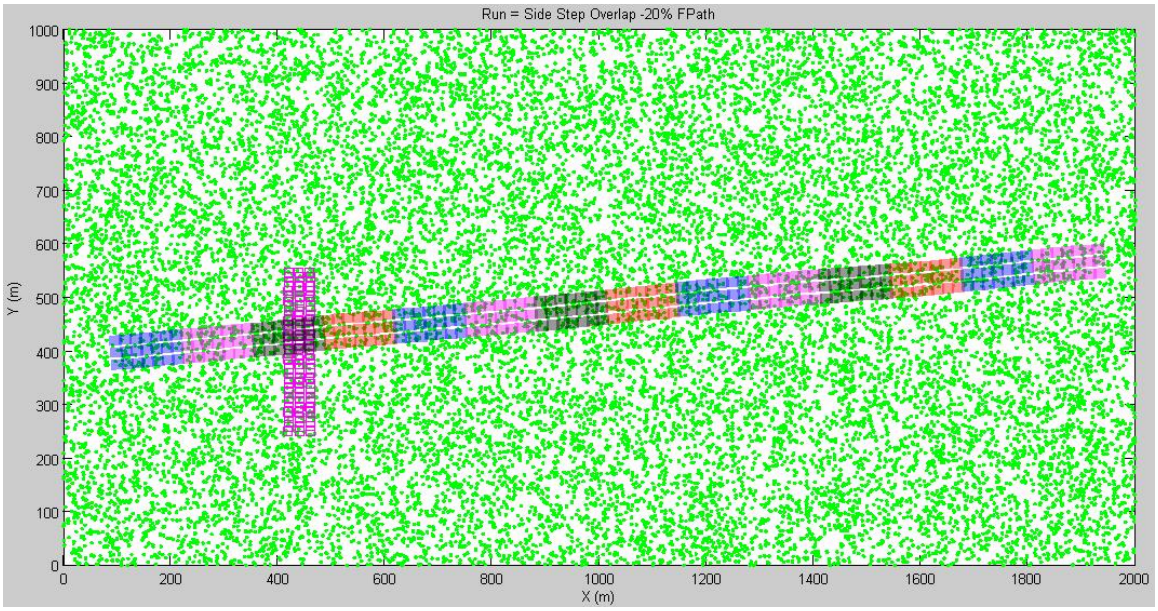

Figure 7.7. Simulated Minefield Layout for a Patterned Minefield with -20% (Holiday) Side-Step Overlap

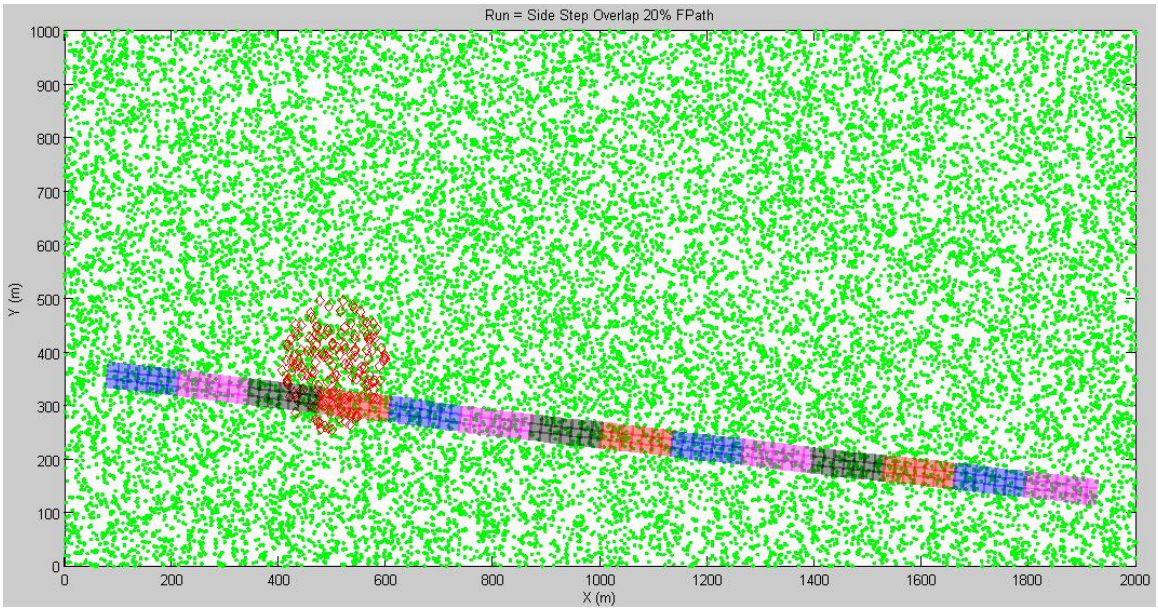

Figure 7.8. Simulated Minefield Layout for a Scattered Minefield with 20% Side-Step Overlap

Although the presence of holidays allows for more area to be covered under each run, the absence of control points results in poor alignment of detection and eventually in

poor minefield performance. This is especially true for patterned minefields due to the presence of a linear pattern. Figure 7.9 shows the effect of side-step overlap on the minefield level performance for a patterned minefield with three rows of mines and scattered minefields. Figure 7.10 shows the corresponding analytical results. Side-step overlap of -20% (holiday, red), 0% (blue), and 20% (green) have been used for the minefield level detection with no registration error. As shown from Figure 7.9 and 7.10, as the side-step overlap decreases, the minefield performance increases. This can be expected because with a decrease in the overlap, the effective swath width of the FoR increases, which results in more targets to be permitted for the performance evaluation for the given mine level FAR. With an increase in the number of allowable targets per segment, the minefield confidence value increases for the segment, resulting in better minefield performance.

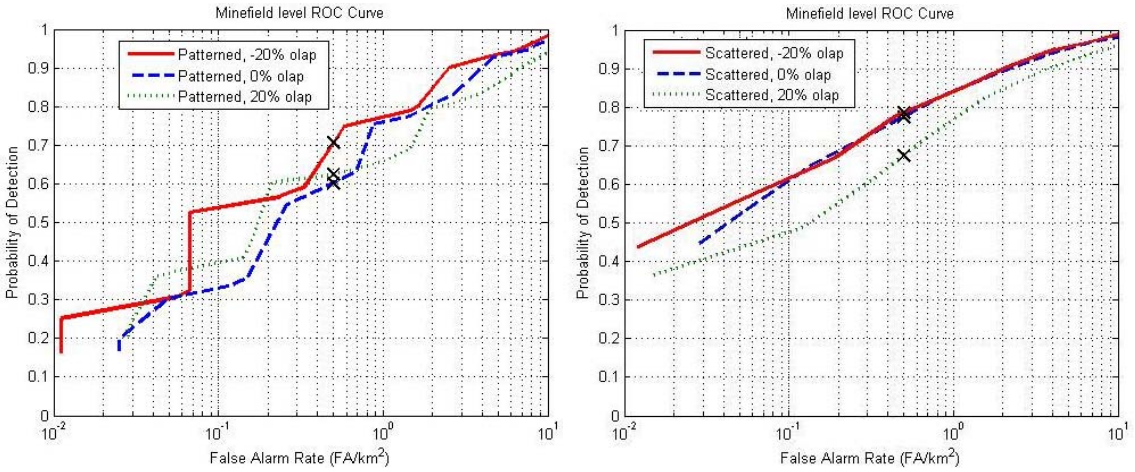

(a) Patterned minefield level ROC curve (b) Scattered minefield level ROC curve

Figure 7.9. Simulated Minefield Level ROC Curves for Patterned and Scattered Minefields with Different Side-Step Overlap

Figure 7.11 shows the minefield performance when some amount of registration error (5m) is present. In this case, the minefield performance for negative overlap case is in fact poorer than positive overlap. This is because for the case of negative overlap (holiday) or no overlap, the image frames are not stitched in any trustworthy fashion

along the steps. Thus, pattern detections suffer because rows or targets that were actually in a linear pattern do not appear to be so. This effect on scattered minefield detection is less pronounced as the detection statistics are based on count and not their distribution.

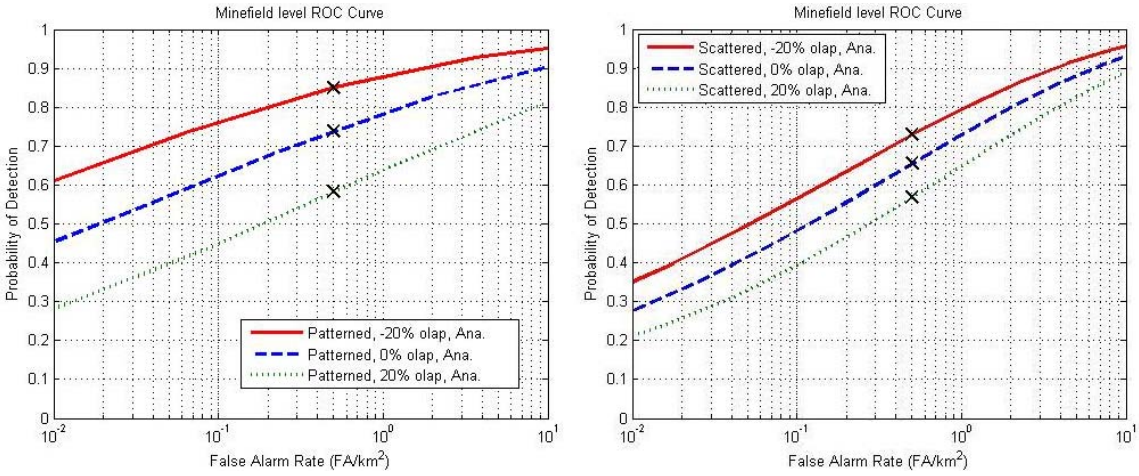

(a) Patterned minefield level ROC curve (b) Scattered minefield level ROC curve

Figure 7.10. Analytical Minefield Level ROC Curves for the Patterned and Scattered Minefields for Different Side-Step Overlaps

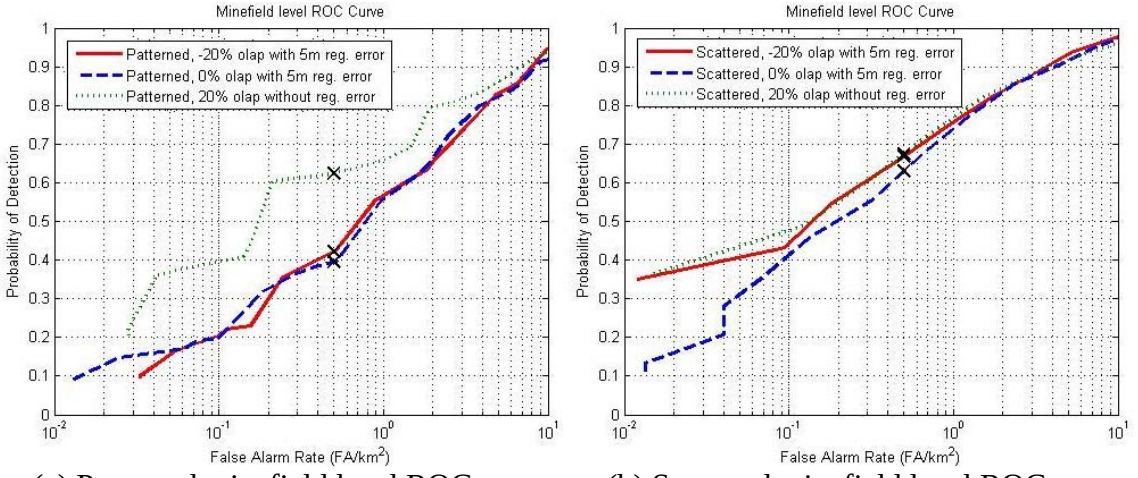

(a) Patterned minefield level ROC curve (b) Scattered minefield level ROC curve

Figure 7.11. Simulated Minefield ROC Curves for Patterned and Scattered Minefields for Different Side-Step Overlaps with a Registration Error of Five Meter

7.5. EFFECT OF SEGMENT OVERLAP

Once the inter-segment (frame to frame) registration is complete, the intra-segment registration must be done so as to reconstruct the complete run. Just like frame to frame registration, the segment to segment registration is also dependent on the amount of overlap available between the consecutive segments. A segment overlap of zero implies that each FoR is disjointed from the others, and an overlap of six implies that every new captured swath and the previous six swaths are used for minefield evaluation.

Examples for the segment overlap of two and segment overlap of four are shown in Figures 7.12 and 7.13, respectively, for a scattered and patterned minefields, respectively. Figure 7.14 shows the effect of segment overlap on the minefield level performance for a patterned minefield with three rows of mine and scattered minefield, respectively. Segment overlaps of zero (red) and six (blue) segments have been used for the minefield level ROC curve.

As shown in Figure 7.14, the minefield performance improves slightly for overlapping FoRs. This is because with the no overlap case, a minefield may lie partially in each of two consecutive FoRs, which implies poor detection in both FoRs, and hence, poor performance.

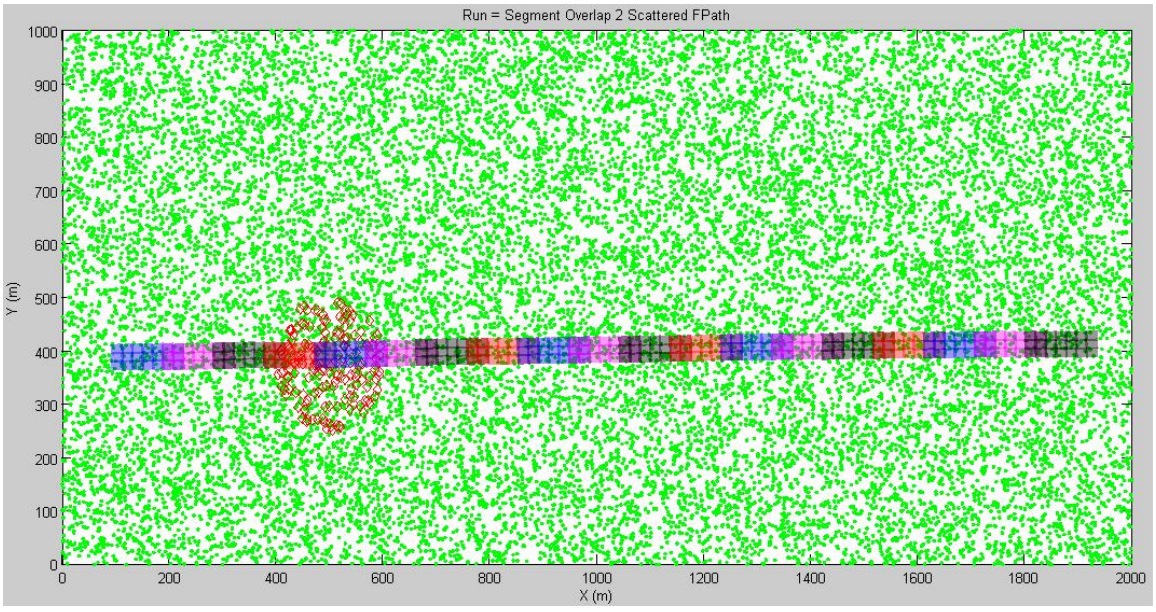

Figure 7.12. Simulated Minefield Layout for a Scattered Minefield with a Segment Overlap of Two Segments

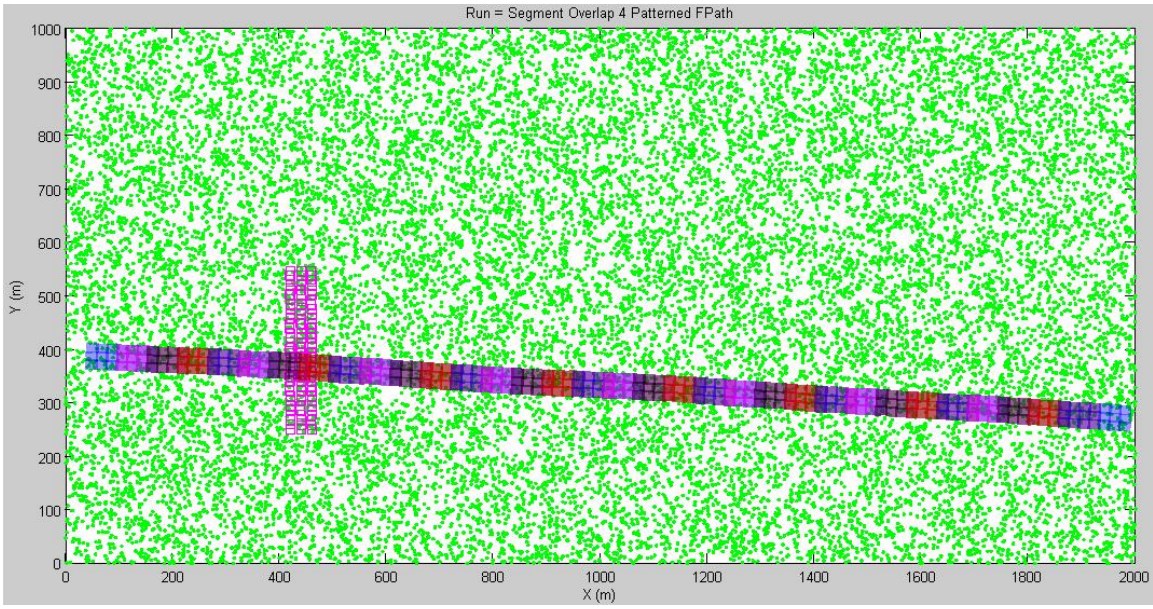

Figure 7.13. Simulated Minefield Layout for a Patterned Minefield with a Segment Overlap of Four Segments

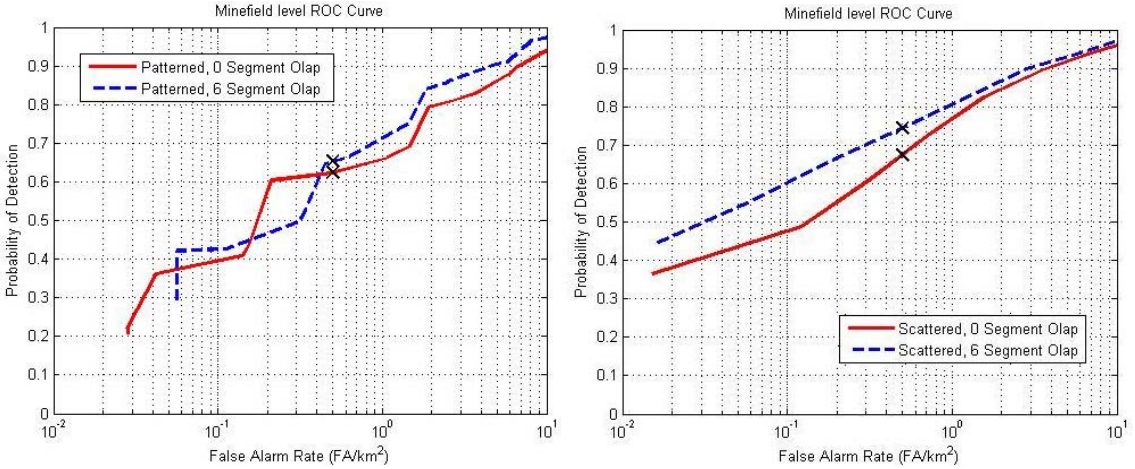

(a) Patterned minefield level ROC curve (b) Scattered minefield level ROC curve

Figure 7.14. Simulated Minefield Level ROC Curves for Patterned and Scattered Minefields for Different Segment Overlaps

8. CONCLUSION AND FUTURE WORK

A typical airborne minefield detection system is modeled and mine and minefield level performance are evaluated based on simulated data under different data collection scenarios. The simulation system created to synthesize representative data under different scenarios of interest is discussed. The parameters that drive the system's performance are identified, and the simulated results are evaluated and discussed. The effects of different thresholding schemes used for thresholding the anomaly statistics on the airborne data are discussed. CFAR seems to be the most effective technique for threshold selection because the threshold is selected adaptively depending on the background statistics. A fixed threshold and constant target rate suffer with potential limitation of poor performance due to non-homogeneity of the background. Non-homogeneity of the background has however not been modeled in the simulation tool.

Central F distribution is successfully used for modeling the RX detection statistics. The parameters for modified central F-distribution are obtained using EM algorithm and the results for modeling different combinations of MSI bands, and different target radii are shown. Eight different data sets are created depending on the type of background, time, and for background only and background with minefield for which the modeling performs quite well. The modeling results seem to be good especially for target radii of 1 and 2. The results for the homogeneous or approximately homogeneous background for a complete FoR excel, whereas for mixture of backgrounds the modeling is generally poor indicating likely multimodal distribution. Modeling performance and fit are shown using both PDF and inverse CDF.

Various spatial distribution techniques used for modeling the spatial locations of the false alarms are discussed. However, a satisfactory match between the actual spatial locations and simulated spatial locations for false alarms must be explored further because actual spatial locations are clustered and do not follow Poisson distribution. Analytical models for both scattered and patterned minefields are effectively derived and implemented in the simulation system. They present a good agreement with the proposed minefield detection algorithms. Simulation results for a range of different parameters and

their effect are discussed in Section 7. The simulated results and analytical results are found to be in good agreement.

The present work has laid the foundation for a simulation-based system capable of evaluating the performance of airborne mine and minefield detection structures. In the future, this research can be extended on a number of grounds. IR data can also be modeled in a similar manner as the MSI data using the EM algorithm. Other anomaly-detection techniques, especially FAM techniques, can also be modeled. It is also useful to model the spatial distribution for the actual locations of the false alarms and then incorporate those values into the simulation system. This will help to complete the modeling tool that is capable of modeling not only anomaly values but also spatial locations in accordance with actual data. The modeling tool can also be improved to include multiple minefields per run. Finally, it is expected to compare the performance of the simulated data with actual airborne collected data.

APPENDIX A.
SPECTRAL VEGETATION INDICES

This section explains the indices that are used to classify the frames as vegetation or non-vegetation. Several Spectral Vegetation Indices (SVIs) are available in the literature that provides a measure of live, green vegetation in an area. These indices are designed to enhance the vegetation signal in remotely sensed data. Most of these indices use a combination of data from various spectral bands (red, blue, green, and near band IR) into a single value. The idea of SVIs is based on the fact that the spectral response of green leaves exhibits a jump in the reflectance in the near infrared NIR portion (700 – 1350 nm) due to the dominant plant pigment, chlorophyll. This response is often called an IR rise [Emch, 2001]. Figure A.1 shows the spectral reflectance curve for dirt (brown), rock (black), and vegetation (green). The IR rise phenomenon for the green vegetation is quite visible from the figure. As seen in figure, the plants also exhibit pronounced absorbance of the bluish (400 - 500 nm) and reddish (600 – 700 nm) wavelengths thus appearing green. This absorption of red or blue bands along with IR rise can be exploited to provide a unique index for the vegetation cover. Different SVIs are discussed in the following Subsections.

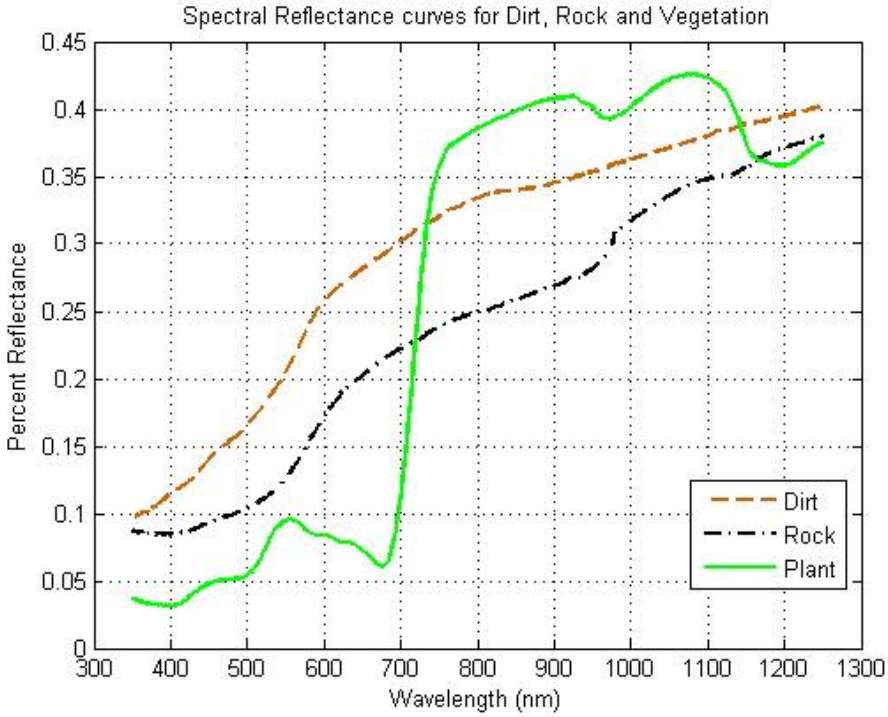

Figure A.1. Spectral Reflectance Curves for Different Land Forms

A.1. Simple Ratio or Ratio Vegetation Index (SR or RVI)

One of the simple SVI metric is a simple ratio between NIR and red bands. Thus,

$$\text{SR or RVI} = \text{NIR/RED} \tag{A.1}$$

SR values for the bare soil are generally near 1 because for the bare soil, the Red and NIR bands have similar reflectance. For the live vegetation, the SR increases. The SR values are unbounded and can range from 0 to infinity. Figure A.2 shows an example for SR for a dense vegetation frame. The red and NIR bands appears in the top part of the figure. The PDF of the SR values is also shown in Figure A.2. On the SR image, red dots indicate the pixels having an SR value greater than 3 (representing high likelihood of vegetation). From the figure, it can be noted that the SR is quite effective in detecting the presence of live vegetation. The red points fall approximately on top of the vegetation areas. The SR values are not estimated for edge pixel of 20 pixels width.

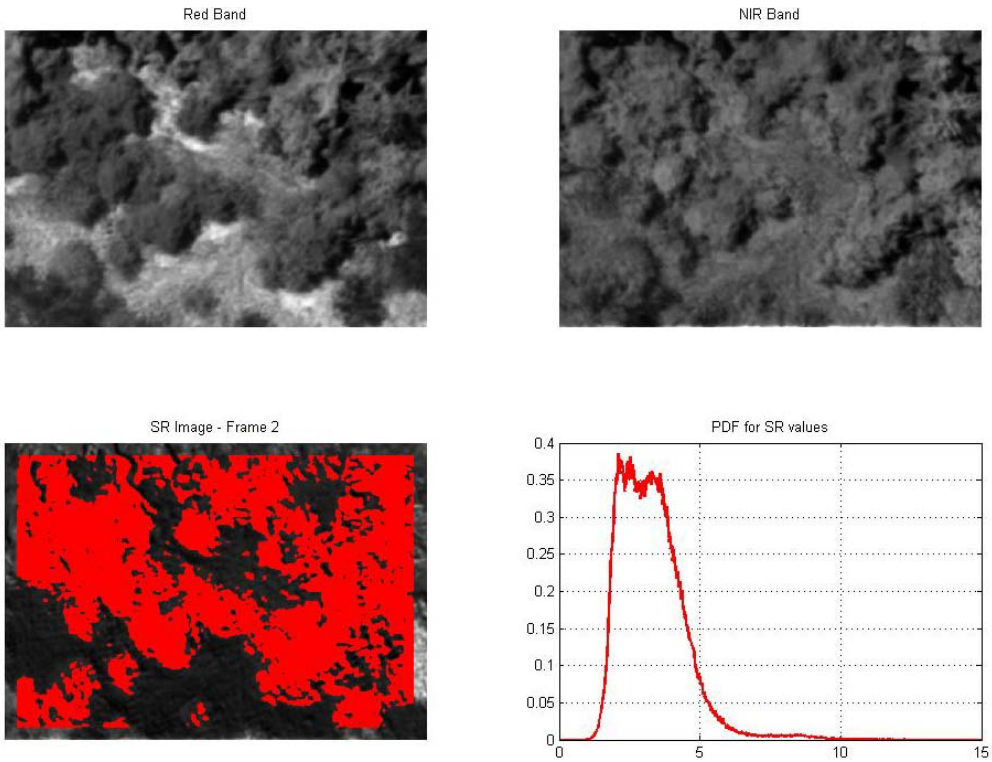

Figure A.2. Red Band, NIR Band, Simple Ratio (SR) Image and Histogram for the Vegetation Frame. The Red Dots Indicate the Pixels Having an SR Value Greater than 3

A.2. Normalized Difference Vegetation Index (NDVI)

NDVI is defined as:

$$NDVI = (NIR - RED)/ (NIR + RED) \quad (A.2)$$

As shown from Equation (A.2), the difference between the NIR and RED bands is divided by their sum. This normalization is used to minimize the effect of variable irradiance levels. NDVI is always bounded between -1 and 1. A higher positive value of NDVI indicates the presence of green vegetation, whereas a value close to 0 indicates a non-vegetation background or dead vegetation. Free-standing water (e.g., oceans, seas, lakes, and rivers) which has low reflectance in both NIR as well as visible bands, results in very low positive or slightly negative NDVI values, whereas clouds and snowfields exhibit negative values for this index.

Figure A.3 shows the individual red and NIR bands along with the NDVI image and the PDF for the NDVI values for a dirt frame. Threshold of 0.4 is used to classify the live vegetation with other areas. As shown from Figure A.3, the histogram for the dirt only frame is symmetric and has the peak at 0.26. Moreover, for the dirt frame, no pixel is chosen for an NDVI value greater than 0.4. Figure A.4 shows the individual red and NIR bands along with the NDVI image and the PDF for the NDVI values for a vegetation frame. In this case, for a threshold of 0.4, most of the vegetative region is correctly identified as vegetation. This indicates that NDVI can act as a good classifier to differentiate between vegetation and non-vegetation features.

In Figure A.4, some regions with shadow are also detected as vegetation along with the actual vegetation. This suggests that although NDVI is a good classifier for the vegetation, some false alarms can be produced due to the presence of shadows or the misalignment of bands.

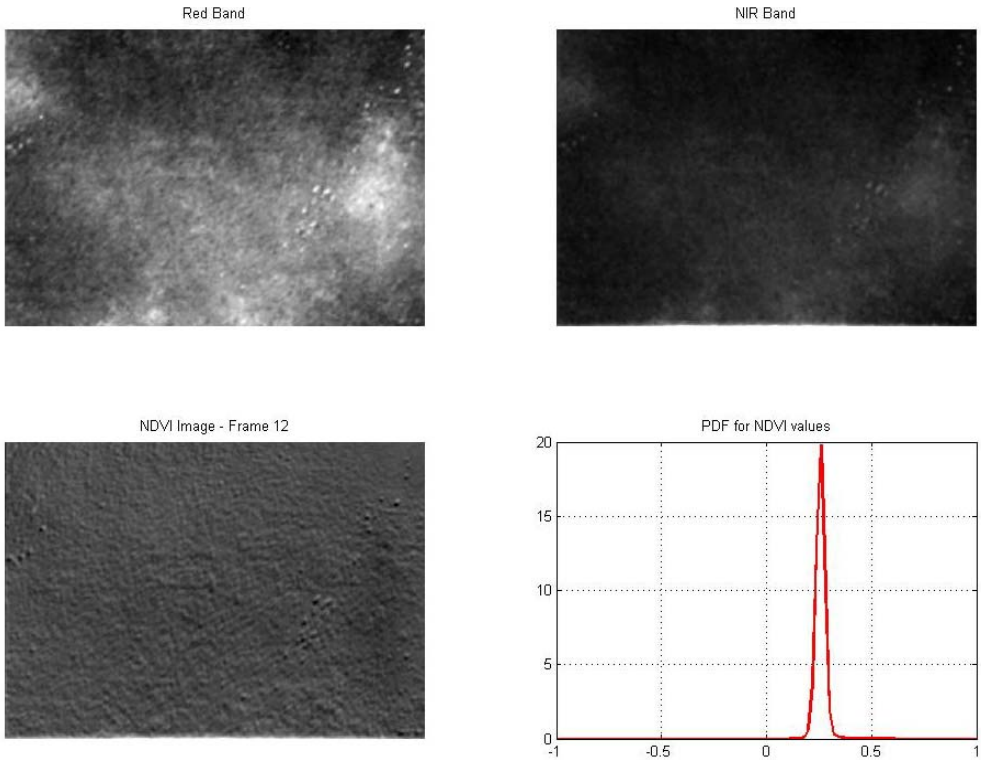

Figure A.3. Red Band, NIR Band, NDVI Image and Histogram for the Dirt Only Frame

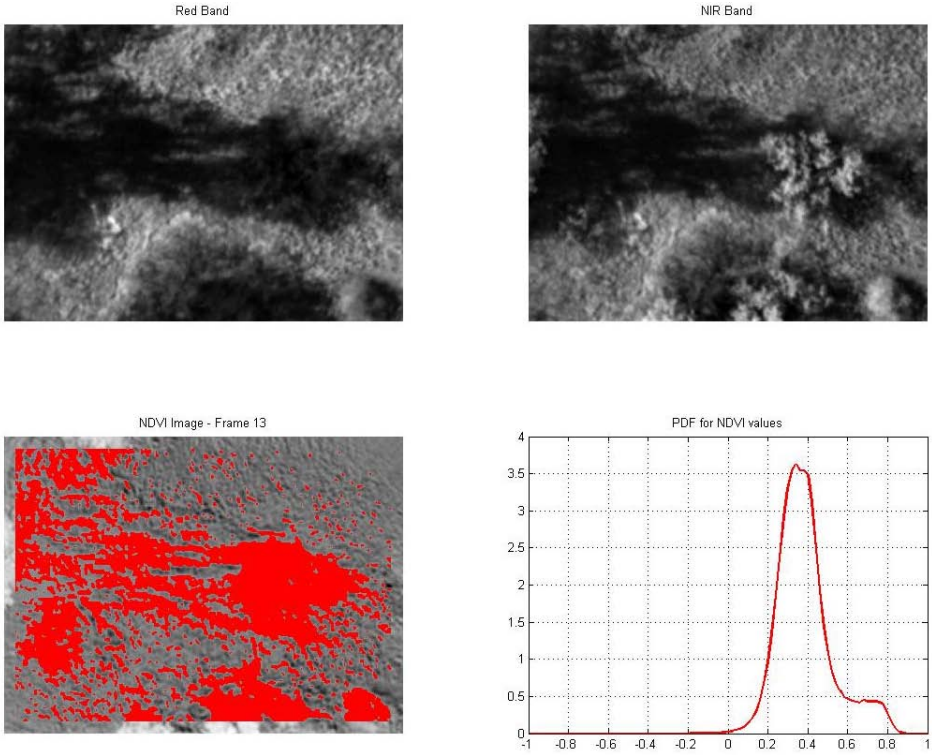

Figure A.4. Red Band, NIR Band, NDVI Image and Histogram for the Vegetation Frame. The Red Dots Indicate the Pixels Having an NDVI Value Greater than 0.4

A.3. Normalized Difference Vegetation Index with Blue ($NDVI_B$)

Because both the red and blue colors are absorbed by chlorophyll in live green vegetation, the blue band can also be used to calculate the NDVI. Thus, in that case $NDVI_B$ is defined as

$$NDVI_B = (NIR - BLUE)/ (NIR + BLUE) \quad (A.3)$$

Figure A.5 shows an example for a blue band, NIR band, $NDVI_B$ image, and $NDVI_B$ histogram using a blue band instead of a red band for the same frame used for NDVI demonstration. Also, an $NDVI_B$ value of 0.6 has been used to threshold the pixels as compared with a threshold of 0.4 used in NDVI thresholding in Figure A.4. Comparing Figure A.4 and A.5, it can be seen that both metrics are effective for classification of vegetation. Most importantly, in the case with blue band, the shadow is considerably lower in the $NDVI_B$ thresholded image.

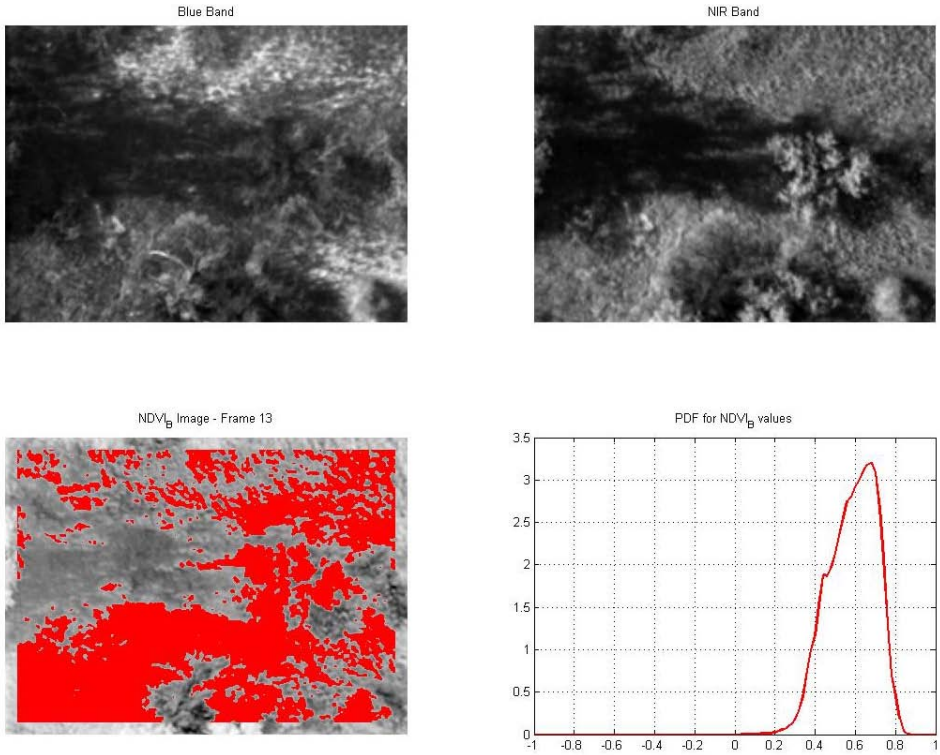

Figure A.5. Blue Band, NIR Band, $NDVI_B$ Image and Histogram for the Vegetation Frame. The Red Dots Indicate the Pixels Having $NDVI_B$ Value Greater than 0.6.

Figure A.6 shows the combined NDVI and $NDVI_B$ values along with red, blue, and NIR bands. It clearly shows that in the $NDVI_B$ image, the shadows are not detected as vegetation. The vegetation and non-vegetation areas in the frame are also differentiated even if they are in the shadow as shown in Figure A.6. The dirt road under the shadow (encircled in broken cyan) has lower (appear dark) $NDVI_B$ values. However, vegetation under the shadow (encircled in broken yellow) has higher (appear bright) $NDVI_B$ values. Thus $NDVI_B$ using the blue and NIR bands is more effective and offers more resistance to the areas having considerable shadows as compared with NDVI using the red and NIR bands. One of the primary reasons for this improvement could be because the blue color is more ambient (due to sky) and hence the areas with shadows have higher blue illumination as compared to red illumination.

As shown in Figures A.2, A.3, A.4, A.6, and A.5 the vegetation indices are easy and effective indicators that can be used to analyze the presence of green vegetation in the target being observed. This ability is exploited in the current discussion to classify the image frames as being densely vegetative or sparsely vegetative. The data are needed to be classified as dense vegetation or sparse vegetation for the modeling purposes to analyze the effect of vegetation on the RX detection statistics and the distribution of F distribution that is used to model them.

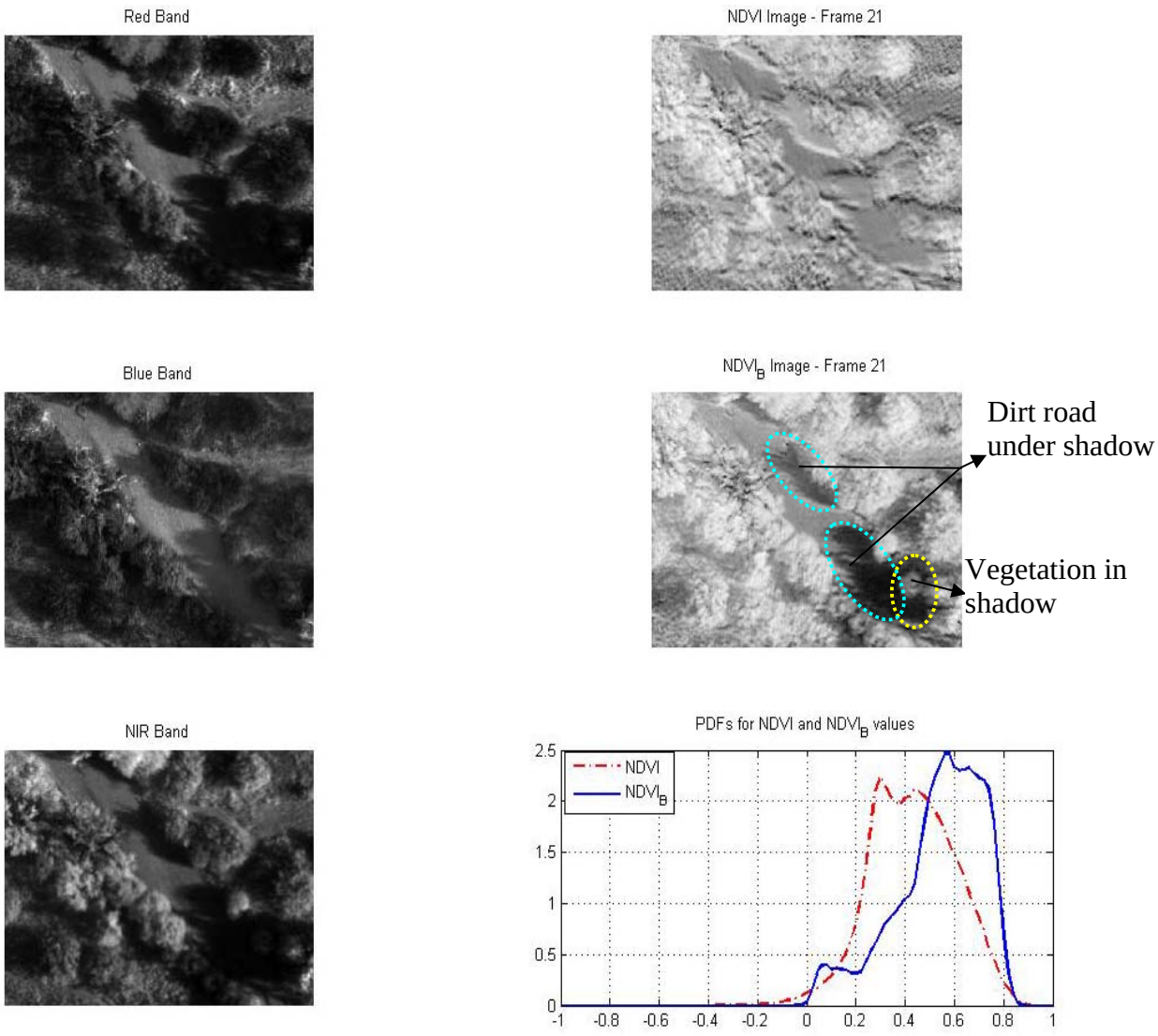

Figure A.6. Red, Blue, and NIR Bands with NDVI and $NDVI_B$ Images. The NDVI and $NDVI_B$ Value Histograms are Also Shown

APPENDIX B.
THE EM ALGORITHM

The EM (**E**xpectation–**M**aximization) algorithm is a general algorithm for the maximum likelihood estimation [Trees, 2007]. It is best employed for incomplete data sets or for data sets with missing values. The term "EM" was coined by Dempster et al., in a paper in 1976. In this thesis, the EM algorithm is used for parameter estimation to model the RX test statistics in the form of a modified F distribution.

The EM algorithm estimates the parameters of the underlying distribution by finding the maximum likelihood function $f(\Theta \mid x)$ for the parameter/parameters Θ given the observed samples $'x'$ in an iterative fashion starting from an initial guess. Each iteration consists of the following two steps [Ganju, 2006; Bilmes, 1998]:

STEP 1: ***Expectation Step*** – This step finds the distribution of the complete data with respect to the known values of the observed data and current estimate of the parameters. The step involves the formulation of the estimation of the likelihood (or log-likelihood) function of the complete data given the observed samples and the current fit of parameters.

STEP 2: ***Maximization Step*** – Effectively, this step maximizes the expectation computed in the first step; i.e., this step re-estimates the anticipated likelihood parameters under the assumption that the distribution found in the first step is correct.

Both of the above steps are carried out iteratively until the terminating condition is reached. The terminating condition can either be the maximum number of iterations reached or else no significant improvement over the previous values of the likelihood. It has already been proved in literature that with each successive iteration, the likelihood estimate either improves or remains unchanged (attain local maximum) [McLachlan and Krishnan, 1997].

The mathematical formulation for the EM algorithm can be explored in [Ganju, 2006; McLachlan and Krishnan, 1997].

B.1. Formulation of update the equation for the RX statistic

The above-said EM algorithm is applied on the RX statistics in the following manner. Post non-max RX statistics can be written as

$$f(r) = \frac{1}{K} f_1(r) e^{-N(1-F_1(r))} \tag{B.1}$$

where
$$f_1(r) = \frac{r^{\left(\frac{v_1}{2}-1\right)}}{B\left(\frac{v_1}{2}, \frac{v_2}{2}\right)(1+r)^{\left(\frac{v_1+v_2}{2}\right)}} \tag{B.2}$$

and $F_1(r)$ is the CDF of $f_1(r)$ and K is given as:

$$K = \int_0^\infty f_1(r) e^{-N(1-F_1(r))} dr = e^{-N} \int_0^\infty f_1(r) e^{NF_1(r)} dr \tag{B.3}$$

Uisng the substitution, $NF_1(r) = u$ it can be shown that

$$K = \frac{1-e^{-N}}{N}, N \neq 0 \tag{B.4}$$

Shown above is a general result applicable to all types of distributions under non-max suppression.

Now taking the natural logarithm of Equation (B.1)

$$\ln f(r) = \left(\frac{v_1}{2}-1\right)\ln r - \ln\left(B\left(\frac{v_1}{2}, \frac{v_2}{2}\right)\right) - \left(\frac{v_1+v_2}{2}\right)\ln(1+x) - N(1-F_1(r)) - \ln K \tag{B.5}$$

Taking the derivative of Equation (B.6), w.r.t. v_1, v_2, and N, and substituting, $B(x,y) = \frac{\Gamma(x)\Gamma(y)}{\Gamma(x+y)}$, provide the update equation for the EM algorithm for parameter estimation. Taking derivative w.r.t. to v_1 to obtain:

$$\frac{\partial \ln[f(r)]}{\partial v_1} = \left[\frac{1}{2}\ln x - \frac{1}{2}\left(\Psi\left(\frac{v_1}{2}\right) - \Psi\left(\frac{v_1+v_2}{2}\right)\right) - \frac{1}{2}\ln(1+x) + NI_1 \right] \tag{B.6}$$

where $\psi(x)$ is a digamma function defined as

$$\psi(x) = \frac{d(\ln(\Gamma(x)))}{dx},$$

and $$I_1 = \frac{\partial}{\partial v_1} F_1(r) = \frac{\partial}{\partial v_1} \int_0^r \frac{r^{\frac{v_1}{2}-1}}{B(v_1/2, v_2/2)(1+r)^{\frac{v_1+v_2}{2}}} dr .$$

In the similar manner, the derivative of Equation (B.1), w.r.t. v_2, is obtained as

$$\frac{\partial \ln[f(r)]}{\partial v_2} = \left[-\frac{1}{2}\left(\Psi\left(\frac{v_2}{2}\right) - \Psi\left(\frac{v_1+v_2}{2}\right)\right) - \frac{1}{2}\ln(1+x) + NI_2 \right] \tag{B.7}$$

where $$I_2 = \frac{\partial}{\partial v_2} F_1(r) = \frac{\partial}{\partial v_2} \int_0^r \frac{r^{\frac{v_1}{2}-1}}{B(v_1/2, v_2/2)(1+r)^{\frac{v_1+v_2}{2}}} dr$$

Also taking the derivative wrt *N* can be obtained as:

$$\frac{\partial \ln[f(r)]}{\partial N} = \left[-1 + F_1(r) - \frac{1}{e^N - 1} + \frac{1}{N} \right]. \tag{B.8}$$

The derivative of the beta function with respect to v_1 and v_2 is defined as

$$\frac{\partial B(v_1/2, v_2/2)}{\partial v_1} = \frac{1}{2}\left(\Psi\left(\frac{v_1}{2}\right) - \Psi\left(\frac{v_1+v_2}{2}\right)\right) B\left(\frac{v_1}{2}, \frac{v_2}{2}\right)$$

$$\frac{\partial B(v_1/2, v_2/2)}{\partial v_2} = \frac{1}{2}\left(\Psi\left(\frac{v_2}{2}\right) - \Psi\left(\frac{v_1+v_2}{2}\right)\right)B\left(\frac{v_1}{2}, \frac{v_2}{2}\right)$$

I_1 and I_2 can also be simplified using the above equalities as:

$$I_1 = \frac{1}{2}\int_0^r f_1(r)\left(\ln\left(\frac{r}{1+r}\right)\right)dr - \frac{1}{2}\left(\Psi\left(\frac{v_1}{2}\right) - \Psi\left(\frac{v_1+v_2}{2}\right)\right)F_1(r),$$

$$I_2 = \frac{-1}{2}\int_0^r f_1(r)\left(\ln(1+r)\right)dr - \frac{1}{2}\left(\Psi\left(\frac{v_2}{2}\right) - \Psi\left(\frac{v_1+v_2}{2}\right)\right)F_1(r).$$

Equation (B.6), (B.7) and (B.8) are the required update equations corresponding to the three parameters to be estimated, which will be used in the next step.

B.3. Parameter Estimation from update equations

Once the update equations are obtained, the information matrix is constructed. The information matrix, 'I_m,' is a square matrix whose dimensions depend on the number of parameters to be estimated. For the current estimation problem, 'I_m' is therefore a 3x3 matrix. The information matrix for the current case is approximated as

$$I_m = \begin{bmatrix} \sum_{j=1}^{n}\left[\frac{\partial \ln[f(r)]}{\partial v_1}\right]^2 & 0 & 0 \\ 0 & \sum_{j=1}^{n}\left[\frac{\partial \ln[f(r)]}{\partial v_2}\right]^2 & 0 \\ 0 & 0 & \sum_{j=1}^{n}\left[\frac{\partial \ln[f(r)]}{\partial N}\right]^2 \end{bmatrix}$$

Let v_1^k , v_2^k , and N^k be the estimates of the parameters in the k^{th} iteration. Then the estimate of these parameters in the $(k+1)^{\text{th}}$ iteration/step is given by

$$\begin{bmatrix} v_1 \\ v_2 \\ N \end{bmatrix}^{k+1} = \begin{bmatrix} v_1 \\ v_2 \\ N \end{bmatrix}^{k} + \lambda \left(I_m\right)^{-1} \begin{bmatrix} \sum_{j=1}^{n} \frac{\partial \log[f(r)]}{\partial v_1} \\ \sum_{j=1}^{n} \frac{\partial \log[f(r)]}{\partial v_2} \\ \sum_{j=1}^{n} \frac{\partial \log[f(r)]}{\partial N} \end{bmatrix}^{k} \tag{B.9}$$

where λ is the scaling factor.

These new estimates of the underlying parameters, 'v_1^{k+1}', 'v_2^{k+1},' and 'N^{k+1},' are then used in three update equations, (B.6), (B.7) and (B.8) to yied a new information matrix, I_m. Information matrix is used in Equation (B.9) to obtain a new set of parameters in the $(k+2)^{\text{th}}$ iteration. The process continues until the parameters converge to a steady state value.

B.4. EM algorithm – Convergence Properties

Like any other non-converging optimization problem, it is possible for the parameters to converge at a local or a saddle point rather than converging at the global minima. This depends mostly on the type of log-likelihood function. If the log-likelihood function is unimodal, then the convergence of the likelihood function and the parameters is unique. However, in cases when the likelihood function is multimodal, the likelihood function and parameters may converge to some saddle point.

In some cases, if the number of parameters to be estimated in a distribution is large, then the parameters are observed to undergo periodic oscillations after a certain number of iterations [McLachlan and Krishnan, 1997]. This is because as the number of parameters increases, the likelihood surface tends to become flat and thus rather than converging to a steady value, the parameters tend to converge to a range. Under this phenomenon, the EM is said to converge to a circle rather than a single point.

Another important factor deciding the convergence of the EM algorithm is the initial starting point induced in the EM algorithm. It has been reported that if the log - likelihood function has several maxima, minima, or stationary points, than the convergence of the EM algorithm to the right point depends on the choice of the starting point [Wu, 1983]; i.e., if the starting point is near to some saddle point or local point, then it is highly possible that the parameters converge to that saddle point or local point. For the present estimation problem, the initial parameters are derived using methods of moments explained in detail in Appendix C.

APPENDIX C.

ESTIMATING INITIAL PARAMETERS FOR RX DISTRIBUTION

Initial parameters play an important role for parameter estimation using EM approximation. These initial parameters must be carefully chosen so that the parameters converge to the right values. For this reason, alternatives have been searched so as to find the best way to provide the initial parameters to the EM algorithm. One way that is adopted here is based on *Method of Moments* [Pearson, 1902]. In this method, moments for the observed data are used. If there are '*p*' parameters to estimate, then the first '*p*' sample moments are equated to the actual moments of the distribution, given that the actual moments are functions of the parameters of interest.

For the central F distribution, the probability density function is defined as

$$f_1(x) = \frac{\left(\frac{v_1}{v_2}\right)^{\frac{v_1}{2}} x^{\frac{v_1}{2}-1}}{B\left(\frac{v_1}{2},\frac{v_2}{2}\right)\left(1+\frac{v_1 x}{v_2}\right)^{\frac{v_1+v_2}{2}}} \qquad \text{(C.1)}$$

where 'x' is the random variable, 'v_1' is the numerator degrees of freedom, and 'v_2' is the denominator degrees of freedom.

The central F distribution can be transformed into RX statistics as

$$f_1(r) = \frac{(r)^{\frac{v_1}{2}-1}}{B\left(\frac{v_1}{2},\frac{v_2}{2}\right)(1+r)^{\frac{v_1+v_2}{2}}} \qquad \text{(C.2)}$$

where $r = x\frac{v_1}{v_2}$.

The RX statistics, '*r*' needs to be multiplied by the factor of '*k*.' Then the scale factor '*k*' takes care of other non ideal factors as discussed in section 4.1.

For the present case the distribution under concern is post non-max RX detection, not RX detection itself. However, because moments of post non-max RX detection

statistics do not have a closed form expression, this method cannot be used to estimate parameters in that case. But 'v_1,' 'v_2,' and 'k' can be estimated using this method and promoted as initial parameters for the EM algorithm of parameter estimation.

The first three moments about the mean or standardized moments (mean, variance, and skewness) for the transformed and scaled central F distribution function are defined as follows [Johnson, 1995]:

Mean ($k\frac{v_2}{v_1}\mu$) : $$k\frac{v_2}{v_1}\mu = \frac{v_2}{v_2-2}, \qquad v_2 > 2 \qquad \text{(C.3)}$$

Variance ($k^2\frac{{v_2}^2}{{v_1}^2}\sigma^2$): $$k^2\frac{{v_2}^2}{{v_1}^2}\sigma^2 = \frac{2{v_2}^2 v_1 + 2{v_2}^3 - 4{v_2}^2}{v_1{v_2}^3 + 20v_2v_1 - 8{v_2}^2v_1 - 16v_1}, \quad v_2 > 4 \qquad \text{(C.4)}$$

Skewness (S) : $$S = \frac{(2v_1 + v_2 - 2)\sqrt{(4v_2 - 32)}}{(v_2 - 6)\sqrt{({v_1}^2 + v_1v_2 - 2v_1)}}, \qquad v_2 > 6 \qquad \text{(C.5)}$$

where $$\mu = E\{r\},$$
$$\sigma^2 = E\{(r-\mu)^2\},$$
$$S = E\{(r-\mu)^3\}/\sigma^3.$$

The value of 'v_2/v_1' and 'k' are the scale that is required to be multiplied by the RX detections to make it a central F distribution as explained above. As shown from Equation (C.5), no scale is included for the skewness calculation because it is a ratio between the two scaled quantities.

This is now just a linear equation to solve for three unknowns given three equations in those unknowns. The solution is derived below in detail:

From C.3, $$v_1 = k\mu(v_2 - 2) \qquad \text{(C.6)}$$

Using this value of v_1 and putting it in C.4 and simplifying gives:

$$k = \frac{2\mu}{\sigma^2(v_2 - 4) - 2\mu^2} \tag{C.7}$$

Substituting Equation (C.7) into (C.6) to obtain

$$v_1 = \frac{2\mu^2(v_2 - 2)}{\sigma^2(v_2 - 4) - 2\mu^2} \tag{C.8}$$

Substituting Equations (C.7) and (C.8) into Equation (C.5) and simplifying to get

$$v_2 = \frac{4\mu^2 - 8\sigma^2 + 6S\mu\sigma}{S\mu\sigma - 2\sigma^2} \tag{C.9}$$

Thus from the observed samples, the mean, variance, and skewness can be easily obtained, which can then be used in equations (C.9), (C.8), and (C.7) to derive the estimates of ‘ v_2 ’, ‘ v_1 ,’ and ‘ k ,’ respectively.

The RX detections are multiplied by the scale factor ‘ k ’ before passing them into the EM algorithm whereas scale factor of 'v_2/v_1' is dynamically applied inside the EM algorithm. ‘ v_1 ’ and ‘ v_2 ’ are used as the initial parameter values for the numerator degrees of freedom and denominator degrees of freedom, respectively. The initial estimate of the third parameter ‘*N*’ is kept equal to 100 for all the cases of parameter estimation. In the future, it may be possible to include '*k*' as part of EM update equations so that value of '*k*' is estimated along with v_1, v_2, and *N*.

APPENDIX D.

TEST STATISTCS TO MEASURE THE GOODNESS OF FIT

Once a set of model parameters is estimated for a given set of observations, a metric to define the goodness of fit is of interest. Various statistical test schemes are available to measure the goodness of fit between the observed and estimated values of the distribution. Some commonly used goodness of fit tests are as follows:

D.1. Cramer Von – Mises (CVM) Test

The test statistics for this test is given by [Bain and Engelhardt, 1991]:

$$CM = \frac{1}{12n} + \sum_{i=1}^{n}\left[F\left(x_{i:n};\theta\right) - \frac{i-0.5}{n} \right]^2 \qquad \text{(D.2)}$$

where,

n = Number of observations,

$F\left(x_{i:n};\theta\right)$ = CDF of the ordered observations, given θ,

θ = Parameter vector of the given distribution.

Here, an approximate size 'α' test of $H_0 : X \sim F$ is to reject H_0 *if* $CM \geq CM_{1-\alpha}$.

D.2. Kolmogorov – Smirnov (KS) or Kuiper Test

With same assumption as D.1., [Bain and Engelhardt, 1991], the statistics 'D' is given as:

$$D^+ = \max_i \left[\frac{i}{n} - F\left(x_{i:n};\theta\right) \right], \; D^- = \max_i \left[F\left(x_{i:n};\theta\right) - \frac{i-1}{n} \right] \text{ and } D = \max\left(D^+, D^-\right)$$

$$V = D^+ + D^-$$

The statistic given by 'D' is known as the "Kolmogorov-Smirnov" or "KS" statistic, and the statistic given by 'V' is known as the "Kuiper" statistic. Here also, the 'α' test of $H_0 : X \sim F$ is to reject H_0 *if* $KS \geq KS_{1-\alpha}$..

D.3. Chi – Square Test

The test statistics for the Chi Square test are given by [Bain and Engelhardt,

1991]:

$$\chi^2 = \sum_{i=1}^{n} \left[\frac{(O_i - E_i)^2}{E_i} \right] \qquad \text{(D.1)}$$

where, χ^2 = Test Statistic,

n = Sample size,

O_i = Number of observation falling into ith cell, and

E_i = Expected number of observations to fall in the ith cell.

Here, Hypothesis $H_0 : X \sim F$ is rejected if $\chi^2 \geq \chi^2_{1-\alpha}$, where α is the given confidence interval.

The chi–square test is the most flexible and general test. The main limitation of CVM and KS tests is unavailability of critical values except for a few distributions such as exponential, weibull, and Normal required for these tests, though they can be derived for other distributions also. For the cases in which the distribution is completely specified, these tests perform well. However, if the parameters are estimated from the data, then the power of these tests is reduced. This is because new critical values need to be formulated and these must be obtained for the specific parametric form that is to be tested. For the chi-square test, this does not create any problems because in this test the number of degrees of freedom is adjusted in accordance with the parameters that are estimated from the data. Because of this flexibility, this test is used for testing the modeling results.

The degrees of freedom for the chi-square test are calculated in the following manner. First the samples are grouped in bins such that each bin has a certain number of samples. For the present scenario, the samples are grouped together such that each bin has 10 samples. If the number of bins is 'n_b' and 'p' parameters are estimated from the data, then the degree of freedom, 'v,' is given as

$$v = n_b - (p + 1)$$

The test statistics are calculated for a particular FoR as per Equation (D.1). Once the degrees of freedom and test statistics are calculated, the threshold is found for the given confidence interval. Since the test statistics follows a chi-square distribution with v degrees of freedom, hypothesis $H_0 : X \sim F$ is rejected if $\chi^2 \geq \chi^2_{1-\alpha}$, where α is the given confidence interval.

BIBLIOGRAPHY

1. Agarwal, S. and Agarwal, S. (2006). "SimulAMFD: A User Guide," *User Manual*, UMR, July 2006.

2. Agarwal, S. (2003). "Airborne Mine Detection Program Oct 2002 data processing," *Presentation to NVESD at AiTR Meeting*, February 14, 2003, Fort Belvoir.

3. Bain, L., Engelhardt, M (1991). "Introduction to Probability and Mathematical Statistics," *Duxbury Press*, Belmont, California (Second Edition).

4. Banerjee, A., Burlina, P. and Diehl, C. (2006). "A Support Vector Method for Anomaly Detection in Hyperspectral Imagery," *IEEE Transactions on Geoscience and Remote Sensing*, Vol. 44, No. 8, pp. 2282-2291, August 2006.

5. Bilmes, J. A. (1998). "A Gentle Tutorial of the EM Algorithm and its Application to Parameter Estimation for Gaussian Mixture and Hidden Markov Models," *International Computer Science Institute, Berkeley CA and Computer Science Division, Department of Electrical Engineering and Computer Science, U.C. Berkeley*, TR-97-021, April 1998.

6. Carlotto, M. J. (2005). "A Cluster-Based Approach for Detecting Man-Made Objects and Changes in Imagery," *IEEE Transactions on Geoscience and Remote Sensing*, Vol. 43, No. 2, pp. 374-387, February 2005.

7. Carlson, B. D., Evans, E. D. and Wilson, S. L. (1994). "Search radar detection and track with the Hough transform. I. system concept," *IEEE Transactions on Aerospace and Electronic Systems*, Vol. 30, No. 1, pp. 102 – 108, January 1994.

8. Chang, C. and Chiang, S. S. (2002). "Anomaly Detection and Classification for Hyperspectral Imagery," *IEEE Transactions on Geoscience and Remote Sensing*, Vol. 40, No. 6, pp. 1314-1325, June 2002.

9. Copsey, K. D, Webb A. R (2001). "Bayesian Gamma mixture models for target recognition," *Proceedings of CIMA*, Bangor, Wales, June 2001.

10. Corcoran, J. N. (2004). "Spatial Point Processes," *Department of Applied Mathematics, University of Colorado, Boulder*, Fall 2004. (http://amath.colorado.edu/courses/7400/2004fall/002/Web/SS-11.ppt).

11. Cressie, N. A. C. (1991). “Statistics for Spatial Data,” *Wiley series in probability and statistics, John Wiley & Sons*, 1991.

12. Dempster, P., Laird, N. M. and Rubin, D. B. (1977). “Maximum Likelihood from incomplete data via the EM algorithm (with discussion),” *Journal of the Royal Statistical Society*, Series B, Vol. 39, No. 1, pp. 1-38, 1977.

13. Diggle, J. P. (2003). “Statistical Analysis of Spatial Point Patterns,” *Academic Press*, 2003.

14. Dincerler, V. (1995). “Landmines and Mine Clearance Technologies,” *Special Rapporteur, International Secretariat*, October 1995. (http://www.hartford-hwp.com/archives/27a/013.html)

15. Earp, S. L., Elkins, T. J. and Conrath, B. C. (1995). "Detection of random minefields in clutter," *Proceedings of the SPIE, Detection Technologies for Mines and Minelike Targets*, Vol. 2496, pp. 543-555, June 1995.

16. Earp, S. L. (2000a). “A system model for airborne countermine surveillance systems,” *Technical Paper*, February 2000.

17. Earp, S. L. (2000b). “Unpatterned minefield detection, the Poisson model,” *Technical Paper*, December 2000.

18. Earp, S. L. (2002). “A performance model for the detection of patterned minefields,” *Technical Paper*, July 2002.

19. Emch, M (2001). “Biophysical Interpretation of Vegetation Spectral Reflectance,” *Course notes for Application of Remote Sensing*, August 6-17, 2001. (http://www.storm.uni.edu/rs/2001/vh3.html)

20. ESTCP Cost and Performance Report (1999). “Assessment of the remote minefield detection system (REMIDS*),*” *U.S. Department of Defense*, September 1999.

21. FM 20-32 (1998). "Mine /Countermine Operations," *Army Field Manuals, FM 20-32*, Department of the Army, Washington DC, May 1998. (http://www.globalsecurity.org/military/library/policy/army/fm/20-32/)

22. Ganju, R. (2006). “Expectation Maximization and its Application in Modeling, Segmentation and Anomaly Detection,” *Thesis*, UMR, May 2006.

23. Ghaffari, M., Manthena, D., Ghaffari, A., Hall, E. L. (2004). “Mines and human casualties, a robotics approach toward mine clearing,” *Proceedings of the SPIE - Intelligent Robots and Computer Vision XXII: Algorithms, Techniques, and Active Vision*, Vol. 5608, pp. 306-312 , October 2004.

24. Gu, Y., Liu, Y. and Zhang, Y. (2006). “A Selective Kernel PCA Algorithm for Anomaly Detection in Hyperspectral Imagery,” *IEEE International Conference on Acoustics, Speech and Signal Processing*, Vol. 2, pp. 725-728, May 2006.

25. Haskett, H. T. and Reago, D. A. (2001). “Identification of optimal bands in the 3-5 um region for lightweight airborne mine detection system (LAMD),” *SPIE-Detection and Remediation of Mine and Minelike Targets VI*, Vol. 4394, pp. 246 - 257, April 2001.

26. Holmes, Q. A. (1995). “Adaptive Multispectral CFAR Detection of Landmines,” *Proceedings of the SPIE, Detection Technologies for Mines and Minelike Targets*, Vol. 2496, pp. 421 - 432, 1995.

27. Huiyan, Z., Yongfeng, C., Wen, Y. (2005). "SAR Image Segmentation Using MPM Constrained Stochastic Relaxation," *Proceedings of SPIE, MIPPR 2005: SAR and Multispectral Image Processing*, Vol. 6043, pp. 794 - 799, November 2005.

28. Johnson, N. L., Kotz, S.,Balakrishnan, N. (1995) “Continuous Univariate Distributions - Volume 2,” *John Wiley and Sons, INC.*, 1995.

29. Kiryati, N. and Gofman, Y. (1996). “Detecting symmetry in grey level images: The global optimization approach,” *Proceedings of the 13th International Conference on Pattern Recognition*, Vol. 1, pp. 889 - 894, 25 – 29, August 1996.

30. Kummamuru, S. (2002). “Spatial Point Processes for Airborne Minefield Detection,” *Thesis*, UMR, May 2002.

31. Lake, D. E., Sadler, B. M. and Casey, S. D. (1997). “Detecting regularity in minefields using collinearity and a modified Euclidean algorithm," *Proceedings of SPIE, Detection and Remediation Technologies for Mines and Minelike Targets II*, Vol. 3079, pp. 500-507, July 1997.

32. Liao, W. J., Chen, D. H. and Baertlein, B. A. (2001). “Algorithms for detection of surface mines in multispectral IR and visible imagery,” *Proceedings of SPIE Detection and Remediation Technologies for Mines and Minelike Targets VI*, Vol. 4394, pp. 310 - 320, 2001.

33. Malloy, N. (2003). “A linear pattern detector,” *Report, Multisensor Science LLC*, June 27, 2003.

34. McLachlan, G. and Krishnan, T. (1997). “The EM Algorithm and Extensions,” *Wiley series in probability and statistics, John Wiley & Sons*, 1997.

35. Menon, D. and Agarwal, S. (2003). “Radial anomaly detector for small circular targets,” *Draft Paper for NVESD*, December 2003.

36. Menon, D., Agarwal, S., Ganju, R. and Swonger, C. W. (2004). "False-alarm mitigation and feature-based discrimination for airborne mine detection," *Proceedings of the SPIE, Detection and Remediation Technologies for Mines and Minelike Targets IX*, Vol. 5415, pp. 1163-1173, September 2004.

37. Menon, D. (2005). “A Knowledge Based Architecture for Airborne Minefield Detection,” *Thesis*, UMR, August 2005.

38. Møller, J. and Waagepetersen, R. P. (2006). “Modern statistics for spatial point processes,” *Department of Mathematical Sciences*, Aalborg University, June 2006.

39. Muise, R. R., and Smith, C. M. (1995). “Linear density algorithm for patterned minefield detection,” *Proceedings of SPIE, Detection Technologies for Mines and Minelike Targets*, Vol. 2496, pp. 586-593, June 1995.

40. Noiboar, A. and Cohen, I. (2007). "Anomaly detection based on wavelet domain garch random field modeling," *Thesis*, Israel Institute of Technology, January 2007.

41. Pearson, K. (1902). “On the Systematic Fitting of Curves to Observations and Measurements,” *Biometrika*, Vol. 2, pp. 1- 23, November 1902.

42. Ramachandran, H. (2004). "Background modeling and algorithm fusion for airborne landmine data," *Thesis*, UMR, May 2004.

43. Ranney, K. I. (2006). “Hyperspectral Anomaly Detection Within the Signal Subspace,” *IEEE Transactions on Geoscience and Remote Sensing Letters*, Vol. 3, No. 3, pp. 312-316, July 2006.

44. Reed, S. and Yu, X. (1990). “Adaptive multiple-band CFAR detection of an optical pattern with unknown spectral distribution,” *IEEE Transactions on Acoustics, Speech and Signal Processing*, Vol. 38, No. 10, pp. 1760–1770, October 1990.

45. Reich, R. M. (2007). “Introduction to Spatial Statistical Modeling of Natural Resources,” *Slide Presentations, Colorado State University*, May 2007. (http://www.warnercnr.colostate.edu/~robin/slides-a.pdf)

46. Robins, G. and Robinson, B. L. (1995). “Pattern minefield detection from inexact data,” *Proceedings of SPIE, Detection Technologies for Mines and Minelike Targets,* Vol. 2496, pp. 568-574, June 1995.

47. Shadhan, L. and Cohen, I. (2006). “Detection of Anomalies in Textures Based on Multi-resolution Features,” *IEEE 24th Convention of Electrical and Electronics Engineers*, pp. 354-358, November 2006.

48. Simrad, J. R. and Mathieu, P. (1998). “Airborne far IR minefield imaging system (AFIRMIS): Description and Preliminary Results,” *Proceedings of the SPIE, Detection and Remediation of Mine and Minelike Targets III*, Vol. 3392, pp. 84 - 95, April 1998.

49. Sriram, P., Agarwal, S., Mitchell, O. R. (2002). “Gray-scale moment invariants for airborne mine detection, discrimination and false alarm mitigation,” *Proceedings of SPIE, Detection and Remediation Technologies for Mines and Minelike Targets VII*, Vol. 4742, pp. 974-985, August 2002.

50. Stein, D., Beaven, S., Hoff, L. E., Winter, E., Shaum, A. and Stocker, A. D. (2002). “Anomaly detection from Hyperspectral imagery,” *IEEE Signal Processing Magazine*, vol. 19, No. 1, pp. 58–69, Jan. 2002.

51. Trang, A., Agarwal, S., Regalia, P., Broach, T., Smith, T. (2007). “A patterned and un-patterned minefield detection in cluttered environments using Markov marked point process,” *Proceedings of the SPIE, Detection and Remediation of Mine and Minelike Targets XII*, Vol. 6553, No. 8, pp. 1-12, April 2007.

52. Trees, H. L. V. (2007). “Detection, Estimation and Modulation Theory - Part I,” *John Wiley and Sons*, 2007.

53. Webb, A. R. (2000). “Gamma mixture models for target recognition,” *Pattern Recognition*, vol. 33, pp. 2045–2054, 2000.

54. Witherspoon, N. H., Holloway Jr., J. H., Davis, K. S., Miller, R. W., and Dubey, A. C. (1995). "The coastal battlefield reconnaissance and analysis (COBRA) program for minefield detection," *Proceeding of the SPIE- Detection Technologies for Mines and Minelike Targets*, Vol. 2496, pp. 500 - 508, April 1995.

55. Wu, C. F. J. (1983). "On the Convergence Properties of the EM Algorithm," *The Annals of Statistics*, Vol. 11, No. 1, pp. 95-103, March 1983.

56. Yanfeng, G., Ye, Z. and Ying, L. (2006). "Unmixing Component Analysis for Anomaly Detection in Hyperspectral Imagery," *IEEE International Conference on Image Processing***,** pp. 965-968, October 2006.

VITA

Saurabh Agarwal was born on July 30, 1982 in Ajmer, India. In June 2003, he received his Bachelor's degree in Electronics and Communication Engineering from Maharishi Dayanand University — Rohtak, India. He joined the Master of Science program in Electrical Engineering at the University of Missouri—Rolla in spring 2005. While pursuing his graduate degree, he was supported by the Department of Electrical Engineering as a Graduate Research Assistant. He received his master's degree in Electrical Engineering from the University of Missouri—Rolla in August 2007. His technical interests are primarily in all aspects of real time and non-real time signal, image processing and telecommunication.